Application of EPR Spectroscopy to Study the Resting State Structure and the Mechanism of *Mycobacterium tuberculosis* Catalase-Peroxidase (KatG)

by

STEFANIA GIROTTO

A dissertation submitted to the Graduate Faculty in Chemistry in partial fulfillment of the requirements for the degree of Doctor of Philosophy, The City University of New York

2004

Reproduced with permission of the copyright owner. Further reproduction prohibited without permission.

UMI Number: 3115252

Copyright 2004 by
Girotto, Stefania

All rights reserved.

INFORMATION TO USERS

The quality of this reproduction is dependent upon the quality of the copy submitted. Broken or indistinct print, colored or poor quality illustrations and photographs, print bleed-through, substandard margins, and improper alignment can adversely affect reproduction.

In the unlikely event that the author did not send a complete manuscript and there are missing pages, these will be noted. Also, if unauthorized copyright material had to be removed, a note will indicate the deletion.

UMI®

UMI Microform 3115252
Copyright 2004 by ProQuest Information and Learning Company.
All rights reserved. This microform edition is protected against unauthorized copying under Title 17, United States Code.

ProQuest Information and Learning Company
300 North Zeeb Road
P.O. Box 1346
Ann Arbor, MI 48106-1346

Reproduced with permission of the copyright owner. Further reproduction prohibited without permission.

©2004

STEFANIA GIROTTO

All Rights Reserved

Reproduced with permission of the copyright owner. Further reproduction prohibited without permission.

This manuscript has been read and accepted for the Graduate Faculty in Chemistry in satisfaction of the dissertation requirement for the degree of Doctor of Philosophy.

01/20/04
Date

Chair of Examining Committee
Dr. Richard S. Magliozzo

1/26/04
Date

Executive Officer
Dr. Gerald Koeppl

Dr. Richard Pizer

Dr. Tatyana Polenova

Dr. Gary J. Gerfen

Supervisory Committee

THE CITY UNIVERSITY OF NEW YORK

Reproduced with permission of the copyright owner. Further reproduction prohibited without permission.

Abstract

Application of EPR Spectroscopy to Study the Resting State Structure and the Mechanism of *Mycobacterium tuberculosis* Catalase-Peroxidase (KatG)

by

Stefania Girotto

Adviser: Dr. Richard S. Magliozzo

Mycobacterium tuberculosis (*M. tuberculosis*) catalase-peroxidase (KatG) is a dimeric Class I heme peroxidase whose activity is implicated for the activation of the anti-tuberculosis antibiotic isoniazid (INH).

The catalytic function and the structure of this enzyme have been examined using rapid freeze-quench (RFQ) and low temperature X-band EPR spectroscopy.

The enzyme exhibits catalytic properties that differ from the Class I peroxidases. The reaction of ferric KatG with peroxyacetic acid was followed using RFQ-EPR (77 K). A doublet EPR signal appears within 6.4 ms after mixing and at time points through hundreds of milliseconds. Thereafter, a singlet signal develops and finally predominates after 1 s. Simulation of EPR spectra and isotope labeling experiments assigned both doublet and singlet EPR signals to tyrosyl radical(s). A two-state model was found to be adequate to describe the kinetics of evolution of the EPR signal from doublet to singlet observed in X-band data while High Field EPR results suggest that a distribution of orientations are present.

Single amino acid replacements in KatG have been investigated as a direct approach to identify the tyrosine residues at which the radical(s) is formed. RFQ-EPR

Reproduced with permission of the copyright owner. Further reproduction prohibited without permission.

spectroscopy confirms that tyrosine Y353, unique to *M. tuberculosis* KatG, is the amino acid at which a tyrosyl radical is formed upon turnover with peroxides. Moreover, residue Y229, which is involved in the formation of a newly defined Met-Tyr-Trp adduct in the active site of catalase-peroxidase, is shown to be important for preserving the catalase activity of KatG.

Low temperature EPR studies of ferric KatG, supported by optical and Raman data, suggest that different factors, such as water and other ligand binding, protonation state of the distal imidazole and incomplete adduct formation, are responsible for the heme iron structural heterogeneity observed in the WT enzyme. Coordination of the ferric iron and the geometry of the active site are influenced by small molecules such as INH, which binds at a special binding site removed from the heme. Moreover, alterations in the region of Ser315, whether induced by mutation or INH binding, affect the hydrogen bonding network on the distal side of the heme.

Reproduced with permission of the copyright owner. Further reproduction prohibited without permission.

To my family

Reproduced with permission of the copyright owner. Further reproduction prohibited without permission.

Acknowledgements

I want to express my deepest gratitude to my mentor, for his encouragement, help and guidance throughout the entire doctoral process. In particular, I am very grateful for his patience and understanding during the completion of this thesis.

I would also like to thank the other members of my doctoral committee, Dr. Gary J. Gerfen, Dr. Richard Pizer, and Dr. Tatyana Polenova for their valuable advice and critical review of this work.

I want to thank the two postdoctoral fellows I had the pleasure to work with, Dr. Salem Chouchane and Dr. Shengwei Yu; they have been my teachers, my supporters and, above all, my friends. I thank also my lab mate Xiangbo Zhao for his support and the interesting conversations about our research.

I am very grateful for all the people who welcomed me to the U.S. and helped me accomplish this goal.

Finally, I want to thank my family and friends for their love, support, and encouragement that I always felt even if an ocean stood between us.

Reproduced with permission of the copyright owner. Further reproduction prohibited without permission.

Table of Contents

Reproduced with permission of the copyright owner. Further reproduction prohibited without permission.

Reproduced with permission of the copyright owner. Further reproduction prohibited without permission.

Appendix A

Appendix B Fundamentals of EPR spectroscopy

Reproduced with permission of the copyright owner. Further reproduction prohibited without permission.

List of Figures

Reproduced with permission of the copyright owner. Further reproduction prohibited without permission.

Reproduced with permission of the copyright owner. Further reproduction prohibited without permission.

Reproduced with permission of the copyright owner. Further reproduction prohibited without permission.

List of Tables

Reproduced with permission of the copyright owner. Further reproduction prohibited without permission.

Chapter 1

This thesis is focused on the study of *Mycobacterium tuberculosis* (*M. tuberculosis*) catalase-peroxidase (KatG), a heme enzyme involved in the activation of the most common drug used against tuberculosis (TB) infection.

After antibiotics to treat tuberculosis became widely available in the 1950's, it was believed that tuberculosis would eventually be eliminated, but it continues to be a public health threat, to the extent that the World Health Organization (WHO) has declared tuberculosis a global public health emergency (1). Knowledge about pathogenesis and protection from tuberculosis is growing rapidly due to increased attention to this often fatal disease because of recent upswings in case numbers. Today, *M. tuberculosis*, the organism that causes tuberculosis, is responsible for more mortality in humans than any other pathogen.

The WHO estimated that *M. tuberculosis* is responsible for over 2 million deaths per year. The highest incidence of TB is recorded in developing countries (Africa, Asia, and Latin America) with poor economic and sanitary conditions (2). In the U.S., the number of TB cases dropped almost every year until 1985. Since 1985, the number of TB cases rose every year, reaching a peak in 1992. This outbreak is attributed to a high rate of immigration from countries with a high incidence of TB, to the development of new multi drug-resistant (MDR) strains and, in particular, to the emergence of HIV (Human Immunedeficiency Virus) infections. HIV patients are easily infected with TB and the rate of mortality is double compared with non-HIV patients (3).

The emergence of MDR and the widening association of mycobacterial infection and HIV have stimulated researchers to study the mechanisms of drug resistance and to

Reproduced with permission of the copyright owner. Further reproduction prohibited without permission.

design more effective anti-mycobacterial agents. Despite current efforts, a new drug highly effective against TB has not been developed since the early 1960's.

1.1 *M. tuberculosis* catalase-peroxidase and other KatG enzymes

Drug resistant *M. tuberculosis* strains typically have mutations in either the gene encoding an enzyme required for mycolic acid biosynthesis (a component of a Type II fatty acid synthase enzyme system) or the gene encoding a catalase-peroxidase enzyme. The catalase-peroxidase (KatG) from *M. tuberculosis* is a heme enzyme encoded by the *katG* gene that turned out to be very important for the mechanism of action of isoniazid (isonicotinic acid hydrazide, INH), one of the most widely used antitubercular drugs. It was shown in recent research that this enzyme is required for *M. tuberculosis* sensitivity to isoniazid (4-6) leading to a new interest in a relatively poorly characterized class of bacterial enzyme.

The catalase-peroxidases, a new class of bacterial heme enzymes, were first identified in 1979 (7). These enzymes have both catalase and peroxidase activities and play an important role in the response to oxidative stress arising from the continuous metabolic generation of reactive oxygen byproducts or environmental factors (8,9). The literature on the structure and function of heme proteins and enzymes is vast and will not be surveyed here except for those aspects that are specifically relevant to the studies in this thesis.

The first catalase-peroxidase to be identified, Hydroperoxidase I (HP I), was from *Escherichia coli* (*E. coli*). Hydroperoxidase I, a constitutive enzyme, is a tetramer with only two hemes per tetramer. In 1985, the gene for Hydroperoxidase I, called *katG*, was identified and sequenced, leading to recognition of the catalase-peroxidases as part of the

Reproduced with permission of the copyright owner. Further reproduction prohibited without permission.

Class I family of prokaryotic origin. They have little sequence homology with typical catalases, but high homology with yeast cytochrome *c* peroxidase (CCP) and ascorbate peroxidase (APX) (7), which are the classical examples of the Class I enzymes. Despite these sequence similarities, there are dramatic differences in catalytic activity and substrate specificity among Class I enzymes. For example, KatGs are the only peroxidases known so far that have both catalase activity comparable with "classical" catalases, as well as typical peroxidase activity with broad specificity (7).

The catalase-peroxidases range in subunit multiplicity from one to four identical subunits per multimer (7). Each subunit contains approximately 730 amino acids, which is twice the number typically found in other peroxidases. The doubling of molecular weight compared with other peroxidases is believed to be the result of gene duplication (10). In fact, each half of the KatG polypeptide has high homology with yeast CCP, yet there is only one heme binding site per polypeptide (7,11). Sequence comparisons among KatGs suggest that the 10 helical regions of the yeast enzyme are also present in each half of the bacterial enzymes, but are usually connected by longer surface loops. The residues contained in these loops may be responsible for the special catalytic functions of the catalase-peroxidases, an issue that is more specifically addressed in Chapter 3.

1.2 KatG and INH activation

Isoniazid (INH) (Figure 1.1) introduced for TB therapy in 1952 (12), is still the most widely used antitubercular drug. Despite its importance, the mode of action of isoniazid is only recently beginning to be understood. An apparent correlation between the loss of KatG activity and INH resistance first suggested the involvement of KatG in INH action (4-6). This was more recently confirmed by the analysis of isoniazid-resistant

Reproduced with permission of the copyright owner. Further reproduction prohibited without permission.

strains, which revealed that isoniazid is a *pro*-drug requiring *in vivo* activation by the mycobacterial KatG (4-6,13). It has already been proven that an enoyl acyl carrier protein reductase, InhA, involved in the production of mycolic acids found in the cell wall, is a likely target of the action of activated INH (14-17). Mycolic acids constitute over 60% of the *M. tuberculosis* cell wall. These are unique, very long fatty acids with 60 to 90 carbons that form a permeability barrier around the mycobacterium cell. Mycolic acids prevent attack by cationic proteins, lysozyme and oxygen radicals in the phagocytic granule (18) and thus contribute to the success of the infection of the host.

So far it is known that once INH is activated by KatG, it forms an adduct with NADH (nicotinamide adenine dinucleotide cofactor) that binds to InhA, inhibiting the synthesis of mycolic acid. This inhibition results in lethal consequences for the mycobacterial cell. Disruptions of the mode of action of the drug are being revealed in ongoing research into the properties of KatG mutant enzymes, and InhA mutants from antibiotic-resistant bacterial strains isolated from clinical settings throughout the world. The purpose of the research into the structure and function of KatG, which is the topic of this thesis, is ultimately designed to provide insights into mechanisms of antibiotic resistance at the molecular level.

1.3 Characteristics of *M. tuberculosis* KatG

M. tuberculosis KatG is a dimer consisting of 81 kDa subunits with one heme cofactor in each subunit's active site (11). The polypeptide consists of 740 amino acids in two domains: 1) the N-terminal domain (residues 55-423) carrying the active site and the heme-binding region of the enzyme; 2) and the C-terminal domain (residues 424-740) whose function remains to be elucidated (10)(Figure1.2).

Reproduced with permission of the copyright owner. Further reproduction prohibited without permission.

The ability of INH to function as a drug requires its activation by KatG and this depends on the catalytic activity residing in the heme group and the surrounding protein. For this reason, it is not surprising that those mutations (some of which have been found in clinical strains, others which have been prepared in the laboratory) in the *katG* gene leading to a single amino acid change in the catalytic domain of the KatG protein result in high resistance of *M. tuberculosis* to INH. Other mutations, outside of the catalytic domain, in particular in the C-terminal region, have negligible impact on the KatG function (10). One particular mutant, KatG[S315T], is among the most common drug resistant enzymes and the subject of some of the work in this thesis.

Although the X-ray structure of *M. tuberculosis* KatG is not available, the crystal structures of two other bacterial KatGs were recently published: the 2.0 Å resolution structure of KatG from *Haloarcula marismortui* (HMCP) (19) and the 1.7 Å resolution crystal structure of KatG from *Burkholderia pseudomallei* (BpKatG) (20). Unfortunately, much of the work in this thesis was performed before these structures were available. Even though these structures belong to KatGs from different organisms, they play a crucial role in the study of *M. tuberculosis* KatG since they allow the formulation of hypotheses based on the sequence homology existing among the family of KatGs. *M. tuberculosis* KatG has high homology with *both B. pseudomallei* and *H. marismortui* KatGs: they are respectively 64.6 % and 55 % (21,22) identical over the complete sequence of residues. More importantly, *M. tuberculosis* and *B. pseudomallei* KatGs are 75.7 % identical over 272 residues (residues 88 to 359) in the catalytic core of the enzyme (20).

Reproduced with permission of the copyright owner. Further reproduction prohibited without permission.

The heme domains of BpKatG and HMCP show high homology with plant peroxidases (Class III). A histidine imidazole is the fifth ligand to the heme iron, as in all the peroxidases (7). The active site triad arginine, tryptophan and histidine (Arg-Trp-His), located on the distal side of the heme, as shown in Figure 1.3 for HMCP, is also typical of all catalase-peroxidases and of Class I peroxidases, and plays a fundamental role in the peroxidase activity of these enzymes (19,20).

The crystal structures provided the discovery of a novel covalent adduct containing a tyrosine, a methionine and a tryptophan (Tyr-Met-Trp) residue in the vicinity of the active site in both BpKatG and HMCP (Figure 1.4). This novel modification is very interesting since its formation may be related to the unique functional properties of the enzymes. Clues about this are discussed in Chapter 3, where the properties of a mutant at the tyrosine residue are presented. The mechanism of adduct formation and its function are not understood at this time (19,20). In the following chapters, the importance of determining if this adduct is formed in the *M. tuberculosis* KatG enzyme and the mechanism of its formation will be specifically addressed.

Other information obtained from the crystal structure of KatG that is of great interest in terms of understanding INH resistance and enzyme mechanism, is the finding of a narrow access channel to the distal side of the heme. This channel is positioned similar to, but is longer than, the access route in peroxidases such as horseradish peroxidase (HRP). The channel in BpKatG has a funnel shape and is narrowest near residue serine Ser324, about 14 Å from the heme iron (20). Of critical importance to the understanding of INH resistance in the *M. tuberculosis* enzyme is the fact that Ser315 in *M. tuberculosis*

Reproduced with permission of the copyright owner. Further reproduction prohibited without permission.

KatG (the homologue of Ser 324 in BpKatG) is the site of a common mutation responsible for more than 50% of the clinically isolated INH-resistant strains of *M. tuberculosis*.

Further discussion regarding the significance of Ser315 is presented in Chapter 4.

1.4 KatG catalytic activity

KatG shows high homology not only to CCP and APX, but also to plant peroxidases such as HRP, especially in the distal and proximal heme regions. This homology raises the likelihood of a functional and not just structural similarity among these peroxidases. However, *M. tuberculosis* has high catalase activity (4500 units/mg) as well as significant peroxidase catalytic activity (0.95 units/mg) (11), which allows the enzyme to oxidize a variety of electron donors.

Our interest in the *M. tuberculosis* KatG enzyme is primarily focused on understanding its mechanism in INH activation. This mechanism is most likely related to the peroxidase cycle of KatG and, by analogy to classical peroxidases. Hydrogen peroxide or other peroxides are therefore considered to be required for initiating the peroxidative drug activation pathway beginning with the ferric form of the enzyme (resting enzyme).

The initiation of the catalytic cycle of KatG, whether considering the catalase or peroxidase activities, requires heterolysis of the oxygen-oxygen bond of hydrogen peroxide or other peroxides (Figure 1.5, reaction 1). This reaction, a two-electron oxidation, releases one water molecule (or an alcohol when alkyl peroxides are used) and results in the coordination of the second oxygen atom to the heme iron. The resulting intermediate, which is two electron equivalents more oxidized than the starting ferric form, is called Compound I (Cmpd I). Its structure in classical peroxidases has been shown to be an oxyferryl iron-protoporphyrin IX: π-cation radical (11). In the catalase cycle, a

Reproduced with permission of the copyright owner. Further reproduction prohibited without permission.

second hydrogen peroxide molecule reduces compound I back to the resting enzyme, completing the two-substrate catalytic cycle (Figure 1.5, reaction 2).

In the typical peroxidase cycle operating in the oxidation of organic molecules by HRP, for example, the resting enzyme reacts with one equivalent of H_2O_2 to give Cmpd I (Figure 1.5, reaction 1). Reduction of Cmpd I by a single electron from a substrate molecule yields a second stable intermediate, Compound II (Cmpd II), which contains an oxyferryl heme but no cation radical (Figure 1.5, reaction 3). Finally, Cmpd II can be reduced by a second mole of the substrate to the ferric state in another single-electron step (Figure 1.5, reaction 4) (23). This cycle produces two equivalents of substrate radicals and a variety of colored products that may be used to evaluate enzyme activity.

In contrast to these pathways, in yeast CCP, the second oxidizing equivalent removed by hydrogen peroxide is not stabilized in the π-cation radical of the heme group, but is transferred to a tryptophan residue lying near the heme group. This species was originally known as Compound ES (Cmpd ES), or more recently, CCP Cmpd I. This intermediate is responsible for the catalytic function of CCP in peroxidation of cytochrome c. Another oxidation state that may have catalytic relevance in certain peroxidase reactions is the oxyferrous form known as Compound III (Cmpd III) (24).

The detailed analysis of the peroxidase cycle of KatG has great importance since, as was previously mentioned, the mechanism of drug activation is directly related to the catalytic activity of this enzyme. The next section summarizes work that preceded this thesis research and is fundamental to developing hypotheses that will be presented, and to understanding certain results.

Reproduced with permission of the copyright owner. Further reproduction prohibited without permission.

Optical studies, including stopped-flow measurements based on characteristic changes in the absorption spectrum of the heme as a function of oxidation state changes, have provided details toward the characterization of the catalytic cycle in *M. tuberculosis* KatG. The optical spectrum of five-coordinate resting enzyme in *M. tuberculosis* KatG (in phosphate buffer) has a characteristic Soret peak (B band) at 405 nm ($\pi \rightarrow \pi^*$ transition from the a_{1u} ground state to the e_g excited state of the porphyrin) with a shoulder at 380 nm and a charge-transfer band (CT1) at 642 nm (transition from the highest energy filled orbitals of the porphyrin to the lowest energy partially filled orbitals of the iron) (11).

The optical spectrum of Cmpd I can be observed in stopped-flow experiments after the addition of a few equivalents of alkyl peroxides (*tert*-butyl hydroperoxide, 3-chloroperoxybenzoic acid (CPBA), peroxyacetic acid (PAA)) to resting KatG. The use of such peroxides has a long history in the study of peroxidases as they afford kinetics of the initial reactions usually in a time regime accessible for the commonly utilized stopped-flow techniques. The Cmpd I spectrum is characterized by a decrease of approximately 40% in Soret intensity compared with the resting enzyme, with a λ_{max} at 411 nm. In the visible region of the Cmpd I spectrum, maxima are observed at 550 nm and 590 nm (β and α bands respectively) with a shoulder at 655 nm (CT band) (11). These features, that characterize an oxyferryl iron-protoporphyrin IX: π-cation radical, are quite similar to those of the Cmpd I typical of peroxidases (7). The bimolecular rate constant for Cmpd I formation in *M. tuberculosis* KatG was determined to be 3.1×10^4 $M^{-1}s^{-1}$ for CPBA and 1.2×10^4 $M^{-1}s^{-1}$ for PAA. The rates of Cmpd I formation in KatG were found to depend on

Reproduced with permission of the copyright owner. Further reproduction prohibited without permission.

the nature of the peroxide used, its concentration, and the pH. Cmpd I decays to resting enzyme without any detectable formation of Cmpd II (11).

In most other peroxidases, the formation of Cmpd I can be observed after stoichiometric addition of H_2O_2 to resting enzyme. In the case of *M. tuberculosis* KatG this procedure doesn't allow the optical identification of Cmpd I; this is due to the high catalase activity of the enzyme and the very fast cycling of oxidized intermediates back to the ferric state of the resting enzyme. In contrast, the addition of large excess of H_2O_2 to the resting enzyme, leads to the formation of an unstable Cmpd III with typical features at 418 nm (Soret band), 545 nm (Q_{0v} (β), electronic transition from the a_{2u} state to the vibrationally excited levels of the e_g state of the porphyrin) and at 580 nm (Q_{00} (α) electronic transition from the a_{2u} state to the π^*, e_g state of the porphyrin). The unstable Cmpd III then quickly decays and returns back to the resting enzyme (11).

Optical spectroscopy enabled only a partial analysis of the intermediates formed in the catalytic cycle of KatG upon reaction with peroxides. This thesis describes the application of other techniques, including EPR spectroscopy and site directed mutagenesis that allowed a more complete characterization of *M. tuberculosis* KatG and the intermediates formed during its turnover with peroxides.

1.5 Isoniazid activation and drug resistance

The association between KatG enzyme activity and isoniazid efficacy is well established, though certain questions about the target(s) and chemical mechanism of isoniazid 'activation' remain under investigation. In the last decade, a major effort was made to understand and explain the mechanism of drug activation by *M. tuberculosis* KatG (4,5,25,26). For example, it has been shown that KatG can utilize peroxides to

Reproduced with permission of the copyright owner. Further reproduction prohibited without permission.

oxidize INH, presumably via a Cmpd I /II pathway. On the other hand, KatG also oxidizes INH in the absence of added peroxides suggesting that oxidation can proceed by an alternative mechanism or through an auto-catalytic process, but research has not yet shown what is really happening during such reactions. Alternative pathways to drug activation have been proposed, including an oxyferrous form of KatG reminiscent of the cytochrome P450 oxygenase intermediate (27) and pathways utilizing superoxide (25).

In an attempt to gain more insight into the mechanism of drug interaction with the enzyme, some experiments have been recently pursued in our laboratory. This work, published by Chouchane et al. (28), describes a series of stopped-flow double mixing experiments in which KatG was mixed with CPBA and, after a delay time of 4 s, INH was added to the mixture. The resulting spectra showed the formation of Cmpd I then, after the second mixing step, resting enzyme without any detection of Cmpd II intermediate. Since Cmpd I formed in the first mixing step decays much faster in the presence of INH than in the absence of this substrate, it was argued that Cmpd I was reduced by INH, providing evidence for their direct interaction (28). At this time, it is difficult to propose a complete mechanism for drug activation through the peroxidase cycle, but the fact that Cmpd I reacts with the drug strongly suggests the peroxidase cycle of KatG plays a role in drug activation. Furthermore, radical mechanisms for drug activation have already been proposed (29,30).

Besides the mechanistic aspects of drug activation, another important issue in this context is to understand the details of drug binding to the enzyme. Significant progress was recently made to determine the affinity of the enzyme for the drug. Optical difference spectroscopy of KatG titrated with INH is one of the techniques that has been used to

Reproduced with permission of the copyright owner. Further reproduction prohibited without permission.

evaluate dissociation constants. This approach relies on the fact that INH induces changes in the optical spectrum of the enzyme consistent with conversion of 6-coordinate heme to 5-coordinate heme. The sigmoidal binding curve indicated positive cooperative binding of INH to the enzyme with high affinity (K_d = 5.4 μM) (31). Cooperativity implies a structural difference between the active sites of either subunits within the KatG dimer.

The heme iron in peroxidases is usually a 5-c species, though this is a variable feature that is under investigation for KatG (Chapter 4). The phenomenon of a change in coordination number of heme iron in response to a change in solution conditions has been observed under a variety of conditions, including those to which the enzyme is exposed during isolation and purification. It will be shown in Chapter 4 that the heme coordination in KatG changes from almost completely 5-coordinate in the fresh partially purified enzyme, to completely 6-coordinate heme in the fully purified KatG. For this reason, optical difference spectroscopy is not a very reliable technique to study INH binding in samples that are predominantly 5-coordinate since no optical change can be observed though the drug still binds to the enzyme (32). Recently, the technique of Isothermal Titration Calorimetry (ITC) has been used to evaluate the thermodynamic parameters associated with the binding of INH to KatG. Recent work in our laboratory has provided evidence that a simple decrease in affinity of the enzyme for the drug is sufficient to explain the level of INH resistance in strains carrying KatG[S315T], though other studies have presented some conflicting views on this issue (31,33).

In the recent crystal structure of BpKatG, a site containing electron density for a small molecule was identified near the distal heme cavity. A molecule of INH was modeled into this density. This region, which is close to Ser324 (the equivalent of Ser315

Reproduced with permission of the copyright owner. Further reproduction prohibited without permission.

in *M. tuberculosis* KatG) is a very good candidate for an INH binding site. The crystal structure analysis suggests a mechanism for the oxidation of INH that attributes a double role to Serine 315: it interacts with the hydrazine portion of INH and provides a direct route for electron transfer from the INH molecule to the radical of either Cmpd I or Cmpd II of the heme (20). The greatly reduced affinity of KatG[S315T] for INH is then explained by the assumption that the methyl group of the threonine, which replaces the serine in the mutant, interferes with the specific interactions at this position in the INH-KatG complex.

Drug resistant mutants of *M. tuberculosis* KatG, other than KatG[S315T], involve the replacement of an amino acid that is located far from the INH binding region. Therefore, in these cases it has been proposed that the mechanism of INH resistance may be related to reduction of the peroxidatic activity of the enzyme, modification of catalytic residues, or alteration of the protein folding (20).

The crystal structure of KatG and the hypothetical INH binding site are important starting points in the challenge to clearly understand the mechanism of drug 'activation'. Nonetheless, questions still remain about the identity of an activated form(s) of isoniazid responsible for its effects, and about which oxidation states of catalase-peroxidase are catalytically competent to produce this activation.

The main part of this thesis addresses questions concerned with a more detailed understanding of the peroxidase mechanism of KatG and the identification of all the intermediates involved in its catalytic cycle (Chapter 2). The studies of single amino acid mutations in the KatG amino acid sequence, presented in Chapter 3, are of fundamental

Reproduced with permission of the copyright owner. Further reproduction prohibited without permission.

importance for the accomplishment of this task. A different topic is considered in Chapter 4, where a detailed analysis of coordination number and spin states in the KatG ferric enzyme under different conditions, including in the presence and absence of INH, led to new ideas about the relationship between structure and function in this enzyme. It will in fact be shown that there is communication between the drug binding site and the distal pocket specifically through displacement or re-positioning of a water molecule that may in turn interact with the iron either weakly or more strongly as a consequence of these peripheral structural changes.

Reproduced with permission of the copyright owner. Further reproduction prohibited without permission.

Chapter 2

In the last two decades, a growing importance has been attributed to amino acid based radicals as cofactors in the catalytic cycle of different enzymes.

In 1977, Sjöberg identified for the first time a one electron oxidized tyrosine residue as essential for the activity of ribonucleotide reductase (RNR) (34), an enzyme that catalyzes the conversion of nucleotides to deoxynucleotides in DNA biosynthesis. Since this initial discovery, stable and transient amino acid based radicals have been localized on glycines (35), cysteines (36), tyrosines (37), and tryptophans (38) as well as on a variety of modified tyrosine and tryptophan residues within proteins (39). An important issue for any protein radical is to determine its kinetic competence and therefore its function in the enzyme. Such catalytic function has been proven for tyrosyl radicals in RNR (40), PGHS (41,42), PSII (43) and for tryptophanyl radical in CCP (44), while for the tyrosyl radical found in mammalian catalase (45) and turnip peroxidase isoenzyme 7 (46) a catalytic function has not yet been defined. Frequently, the transient nature of these radicals makes this issue particularly difficult. Two methods have been used for either the identification of these radicals and/or the study of the kinetics of their formation: stopped-flow (SF) UV-vis spectroscopy and rapid freeze-quench (RFQ) electron paramagnetic resonance (EPR) spectroscopy. Usually stopped flow spectroscopy doesn't directly detect the radicals because of their low extinction coefficients, but it allows monitoring changes in the metal center responsible for generating the radicals.

Each of the amino acid-derived radicals are synthesized by a post-translational process involving metal cofactors (heme, non-heme Fe, Cu, Co, or Mn) located either adjacent to the amino acid being oxidized or on a second subunit or "activating enzyme"

Reproduced with permission of the copyright owner. Further reproduction prohibited without permission.

required for radical production (39). The time scale of these oxidation processes (milliseconds) is slow enough to be followed by SF UV-vis and RFQ-EPR spectroscopies. Therefore, these techniques provide mechanistic insight about radical formation pathways.

Recently, the functional importance of tyrosyl radicals has been well established in Class I ribonucleotide reductases (RNR), in prostaglandin H synthase (PGHS), and in photosystem II (PSII) (39). The mechanism for production of the radical requires a hypervalent metal center followed by electron transfer and successive proton transfer (47) or hydrogen atom abstraction from tyrosine (48). The tyrosyl radical then promotes the formation of a substrate radical, either by proton-coupled electron transfer or by hydrogen atom transfer from the substrate, and is reduced in the process. A recent review article by Stubbe and van der Donk provides overviews of radicals in enzyme catalysis, with the latter devoted solely to tyrosyl radicals (39).

In general, the catalytic function of peroxidases resides solely in the heme group, which can shuttle between three or four oxidation states to perform its functions. In a growing number of examples, the heme based radical of Cmpd I is transferred to an amino acid (Chapter 1) in order to provide a function with unique specificity; this specificity is not usually provided by plant peroxidases, which catalyze the oxidation of a broad range of organic and inorganic substrates.

2.1 Rapid freeze-quench EPR results

Early experiments showed that KatG behaves in many ways like the classical peroxidases. For example, optical SF experiments demonstrated that ferric *M. tuberculosis* KatG forms Cmpd I (oxyferryl iron porphyrin π-cation radical) in the reaction with alkyl hydroperoxides, which is the first and typical step in both the catalase and

Reproduced with permission of the copyright owner. Further reproduction prohibited without permission.

peroxidase cycles of this enzyme. Moreover, this intermediate can be reduced to resting enzyme by various substrates (11). Compound I in *M. tuberculosis* KatG decays relatively rapidly (seconds) in the absence of exogenous substrates (11) and this suggests that endogenous electron transfers produce amino acid based radicals during the process. Rapid freeze-quench EPR experiments were undertaken in an attempt to verify this hypothesis and further investigate the catalytic pathway of the enzyme.

In RFQ-EPR experiments (Appendix A), samples were prepared by mixing ferric KatG with peroxide and letting the mixture react for different periods of time. Each sample was then rapidly frozen in EPR tubes thereby quenching the reaction at a specific time point. EPR spectroscopy allows the study and characterization of the samples frozen as a function of time. Thus, valuable kinetic information can be obtained from a kinetic analysis of the acquired data.

Figure 2.1 shows the results for a typical RFQ-EPR experiment using 100 μM KatG mixed with peroxyacetic acid (300 μM) frozen after reaction from 50 ms to 10 s[1]. An initial doublet signal centered at g = 2.004 observed from 10 ms through ~500 ms is characterized by a principal hyperfine splitting of ~19 gauss and a linewidth of ~30 gauss. The earliest time experimentally accessible (6.4 ms) also shows a doublet EPR signal (data not shown). At longer incubation times, a singlet EPR signal centered at g = 2.004 appeared and it is characterized by a linewidth of ~27 gauss and weak hyperfine features appearing as small shoulders.

[1] An alkyl peroxide was chosen for all the experiments because hydrogen peroxide is rapidly decomposed by KatG, while PAA generates Cmpd I but does not usually act as a substrate for Cmpd I in a second turnover step. Thus, it is used as a means of starting the peroxidase cycle without catalase turnover.

Reproduced with permission of the copyright owner. Further reproduction prohibited without permission.

The same doublet and singlet signals were observed when *m*-chloroperoxybenzoic acid was used in place of peroxyacetic acid. This provides evidence that the radical formed is a protein based radical. Both peroxides were also shown in separate experiments to generate Cmpd I from the resting enzyme (11).

2.2 Simulation of EPR spectra

In an attempt to identify the radical species described above, both the doublet and singlet EPR spectra obtained from the RFQ-EPR samples were simulated. The simulations were performed using software provided by F. Neese (49,50). This program, starting from an initial assumption that the system is made up of an electron (S = ½) coupled to one or more I = ½ hydrogen nuclei allows the user to enter the g-tensor values and hydrogen nuclear hyperfine couplings (isotropic and or anisotropic) for simulation and comparison of simulation to the experimental data.

The spectra obtained from RFQ-EPR experiments of KatG showed a resemblance to EPR data published for the tyrosyl radical in prostaglandin H synthase I (PGHS-I) (51). This resemblance provided information about the initial choice of parameters to be used in the simulations. The EPR parameters initially chosen were then adjusted according to criteria better described below, until the simulated EPR spectrum fit the experimental one as judged by eye. This was preferred to an automated least-squares fitting routine also available in the software because fitting the simple spectra didn't require quantitative comparison of data to simulation.

It is already known from ENDOR spectroscopy and molecular orbital studies that tyrosyl radicals have invariant spin densities on the carbon atoms of the phenolic ring. The unpaired electron spin density follows an odd-alternate pattern with the highest density at

Reproduced with permission of the copyright owner. Further reproduction prohibited without permission.

carbons 1, 3, 5 and on the hydroxyl oxygen (Figure 2.2) (52,53). Despite the invariant spin density distribution, tyrosyl radicals exhibit a variety of EPR spectra (51). The different spectra arise from alterations of the proton hyperfine coupling for the β-hydrogen(s), reflecting different orientations of the phenolic ring with respect to the methylene group of the tyrosine side chain (Figure 2.3).

The spin system used for the simulation involves one unpaired electron and three hydrogen nuclei. The first hydrogen was considered to be one of the two β-methylene hydrogens: the high spin density on C1 can give rise to strong hyperfine coupling to one of the β-methylene hydrogens and thus to a doublet spectrum as observed. In the free amino acid, the single bond between the β-methylene carbon and carbon C1 in the ring has a very low barrier to rotation; for the ring on a tyrosine residue in proteins, this rotation may be hindered due to steric and other interactions. When the ring is fixed in position relative to the methylene group, the two β-methylene protons become non equivalent. If the dihedral angle, θ, formed between a Cβ–H bond and the direction perpendicular to the ring plane is small, only one β–hydrogen is in a position giving relatively strong hyperfine coupling through hyperconjugation. This interaction gives rise to a doublet EPR spectrum and a mainly isotropic coupling (Fermi interaction, Appendix B) (Figure2.3 (a)). If θ is close to 60 °, the hyperfine coupling at the two β–hydrogens will be equal. In this case, a singlet EPR signal is expected for the tyrosyl radical (Figure 2.3 (b)). The second and third protons considered in the simulation are the two equivalent hydrogens at the 3' and 5' positions of the phenolic ring. The anisotropic hyperfine couplings to H3' and H5' (Appendix B) are observed as poorly resolved shoulders in the doublet or singlet spectrum

Reproduced with permission of the copyright owner. Further reproduction prohibited without permission.

(Figure 2.1). The simulation of the doublet and the singlet RFQ-EPR spectra recorded at 250 ms and 10 s respectively (Figure 2.4) gave the parameters reported in Table 2.1.

At this point it seems appropriate to report some discrepancies that have been observed upon examination of a large collection of spectra for similar samples during the RFQ-EPR experiments. Small changes in the linewidths recorded for the doublet and singlet species were observed when the RFQ-EPR experiments were repeated (Chapter 3); this is probably due to small differences in the amount of PAA added to the enzyme, or in the small amount of H_2O_2 sometimes present in the PAA. As a consequence, differences in kinetics result in changes in the linewidths of the EPR features due to small changes in the abundance of doublet and singlet in the spectra (see the kinetic analysis below).

More detailed information on the structure of the tyrosyl radical can be obtained from the analysis of the hyperfine coupling parameters. The hyperfine coupling to the β-methylene hydrogens (bound to the carbon (Cβ) atom neighboring the carbon with the highest unpaired electron spin density (C1)) is strongly dependent on the ring plane orientation, as stated above. The McConnel equation describes the angular dependence of the isotropic hyperfine coupling, A_{iso}, at the methylene hydrogen(s) for a certain spin density on C1 of the tyrosyl ring. From this relation, the value of the dihedral angle, θ, can be determined using the isotropic β- methylene hydrogen nuclear hyperfine couplings obtained from the simulation:

$$A_{iso} = \rho_{C1} (B_0 + B_2 \cos^2\theta)$$

B_0 is close to zero; B_2 ~ 162 MHz for alkyl radicals (51,54). As the spin density distribution for tyrosyl radicals is almost invariant in both model and enzyme systems, the value of 0.39 can be used for ρ_{C1} (53). The A_{iso} values obtained from the simulations of

Reproduced with permission of the copyright owner. Further reproduction prohibited without permission.

the doublet and singlet EPR spectra are 48.3 MHz and 35.0 MHz respectively. Assuming that the percentages of singlet and doublet signals present in the RFQ-EPR spectra recorded at 250 ms and 10 s respectively are negligible, we obtain ~29.0° and ~ 41.9° for the dihedral angle, θ in the doublet and singlet respectively. These θ values may be dependent on steric constraints on the ring and therefore, may not represent lowest energy conformations (see below).

2.3 Isotope labeling experiments

The assignment of both doublet and singlet EPR signals to tyrosyl radicals was tentatively made based on the above analysis. The identification of the radical species couldn't be considered definitive since similar EPR spectra could represent a neutral tryptophanyl radical (55). This is due to the fact that the principal hyperfine splitting in the EPR spectra for both tyrosyl radical or tryptophanyl radical arises from the strong interaction of the unpaired electron on the phenol or indole rings with the β-methylene hydrogen(s) (55,56).

To confirm the assignment of the doublet and singlet EPR signals to tyrosyl radicals, isotope labeling experiments were undertaken. Isotope labeling (34) is a generally proven technique for definitive assignments of radicals in proteins and has been readily applied in systems where proteins are overexpressed in bacteria. The RFQ-EPR experiments described above were therefore repeated using deuterium labeled KatG to distinguish tryptophanyl from tyrosyl radical. The hyperfine coupling of the unpaired electron with a deuterium nucleus is reduced compared with the same interaction with a hydrogen nucleus due to different values of their magnetogyric ratios ($g_n(^1H)$ =

Reproduced with permission of the copyright owner. Further reproduction prohibited without permission.

5.5856948; $g_n(^2H) = 0.8574388$) (57). Deuterium substitution in the amino acid on which the radical is formed will result in a predictable change of the EPR features.

Deuterium labeled KatG was prepared according to the procedure reported in Appendix A, by enzyme overexpression in *E. coli* grown in minimal media containing either 2,4,5,6,7-[$^2H_5$]tryptophan or 3,3-[$^2H_2$]tyrosine. Growth in minimal media, which lacks all amino acid sources, in the presence of a labeled amino acid results in uptake from the medium and incorporation into proteins. This method, already used for the identification of the radical found in RNR (34), leads to the specific labeling of the enzyme with the desired isotopically-labeled amino acid.

The isotope labeling experiment required modification of the growth conditions routinely used for the unlabeled protein. The LB medium used to grow *E. coli* was substituted in these experiments with M9 (minimal) medium to prevent the incorporation into the enzyme of unlabeled amino acid present in the LB broth. Unfortunately, the *E. coli strain* UM262 used at that time, as described in Appendix A, showed an extremely low production of KatG in this medium even after prolonged growth periods. The medium was also supplemented, in addition to the labeled amino acid, with all the other unlabeled amino acids, but, unexpectedly, this completely inhibited overexpression of KatG. Therefore, the overexpression plasmid carrying the *katG* gene had to be transformed into *E. coli* BL21, which is known to grow in minimal medium (Appendix A).

The labeled enzyme was successfully prepared using *E. coli* BL21 grown in minimal medium (Appendix A). RFQ-EPR spectra, obtained as described above, were recorded. Figure 2.5 shows a comparison of the RFQ-EPR spectra obtained from the unlabeled enzyme, the [$^2H_5$]tryptophan-, and [^2H] tyrosine-labeled enzymes. No changes

Reproduced with permission of the copyright owner. Further reproduction prohibited without permission.

were observed for the initial doublet obtained from the [^{2}H]tryptophan-labeled enzyme compared with unlabeled KatG. However, for the [^{2}H] tyrosine-labeled enzyme, a singlet EPR signal (17 gauss linewidth) appeared at a time point at which the doublet appears in unlabeled enzyme. Furthermore, the linewidth of the singlet EPR signal found for labeled enzyme, exemplified by the sample freeze-quenched after 10 s-reaction, exhibited a significantly reduced linewidth (21 gauss *versus* 27 gauss) compared with the unlabeled protein under the same experimental conditions. These results provide conclusive evidence that the EPR signals observed at 250 ms and 10 s were both due to tyrosyl radicals.

At this point, a simulation of the [^{2}H]tyrosine-labeled enzyme spectra was undertaken to confirm that the changes in the EPR signals could be explained based on the expected reduction of hyperfine coupling interactions in the labeled radicals. For the singlet EPR spectrum (RFQ at 10 s) the expected reduction in linewidth was successfully simulated using the same parameters reported above for the fully protonated radical except for those assigned to the β-methylene hydrogen, which was substituted with deuterium (M_I = 1). The magnitude of the the hyperfine coupling values were reduced by the appropriate $g_n(^2H)/g_n(^1H)$ ratio (~0.1535). Simulation of the 250 ms spectrum using deuterium in place of the strongly coupled hydrogen gave a singlet that matching the data (Figure 2.6). Comparisons of the experimental and simulated spectra (250 ms) however, showed that some signal intensity that could correspond to the doublet observed in unlabeled KatG was still present in the RFQ-EPR spectrum of the [^{2}H] tyrosine-labeled enzyme. The intensity of this second signal was approximately 20% relative to the intensity of the original doublet of the unlabeled enzyme. The presence of this signal is not

Reproduced with permission of the copyright owner. Further reproduction prohibited without permission.

likely to be due to incomplete deuteration of the enzyme because the bacteria were never exposed to non-deuterated tyrosine. Whether tyrosine biosynthesis was completely eliminated under the minimal growth conditions, however, is not known. A second hypothesis is the simultaneous presence of a low abundance of a second radical along with the new tyrosyl radical singlet. This idea is discussed below in a section in which the presence of a tryptophanyl radical is presented based on High-Field (HF)-EPR results.

The simulations here suggest that the main changes in the doublet and singlet EPR spectra introduced by the labeling can be explained by the reduction of the principal hyperfine interaction due to the substitution of the β-hydrogen(s) with deuterium: isotope labeling experiments and EPR spectra simulation definitively confirms that the principal radical signal in the singlet and doublet EPR spectra is due to tyrosyl radical.

Although doublet and singlet EPR spectra obtained from the RFQ-EPR experiments may arise from tyrosyl radicals on two separate residues, a single tyrosyl radical could also give rise to both the singlet and the doublet EPR spectra. As reported for the tyrosyl radical in PGHS, the evolution of a tyrosyl radical doublet to singlet EPR signal could be interpreted as a re-orientation of the phenolic ring of the tyrosyl radical with respect of the β-methylene hydrogens (51).

An interesting computational study reported that the configuration giving rise to a singlet EPR signal represents a global minimum in the rotational degrees of freedom of the tyrosyl radical, while the doublet conformation is only a local minimum. Therefore, the finding that the radical exhibits a doublet signal initially, which would be the higher energy conformation, suggests that the phenolic ring of the tyrosine residue is subject to steric constraints by the protein. After the formation of the tyrosyl radical, the interactions with

Reproduced with permission of the copyright owner. Further reproduction prohibited without permission.

the rest of the protein change and the ring is free to rotate to assume a more stable conformation (51). Another study recently published presents a similar structural description of the conformational behavior of tyrosyl radical in a dipeptide model (58).

In the following chapter, it will be shown that the tyrosyl radical in *M. tuberculosis* KatG seems to be localized on Y353, which is a unique tyrosine not conserved in other KatG enzymes; this observation strongly suggests that this radical might be specifically involved in a function of the *M. tuberculosis* KatG enzyme that has yet to be identified. Interestingly, INH was found to quench the doublet EPR species in other RFQ-EPR experiments reported in Chouchane et al. (28).

2.4 High-Field EPR spectra

In order to gain insights into the local environment of the tyrosyl radical in KatG, HF-EPR spectra were collected. This technique resolves the anisotropic g-values of tyrosyl and other radicals that cannot be evaluated from the X-band spectra and therefore it provides information about the identity of the radical formed. In the case of tyroysl radical, the g-values also provide information about hydrogen bonding interactions between the phenolic oxygen and neighboring groups in the enzyme. For example, a comparison of the g-values of different tyrosyl radicals reported in the literature has shown that the values of g_{22} and g_{33} are invariant but g_{11} is variable and depends on the spin density at the oxygen substituent (in this case $|g_{11}| > |g_{22}| > |g_{33}|$) (59). Theoretical as well as experimental studies suggest that there is a proportionality between the spin density on the hydroxyl oxygen (ρ_O^{π}) and g_{11}- g_e (g_e, the free-electron g-value), and between ρ_O^{π} and g_{iso}. The presence of a hydrogen bond to the oxygen substituent reduces ρ_O^{π} and, consequently, the g-anisotropy (59). Therefore, the value of g_{11} is often used as a measure

Reproduced with permission of the copyright owner. Further reproduction prohibited without permission.

of hydrogen bonding to the tyrosyl radical. A g_{11} value of 2.00912 has been attributed to the absence of hydrogen bond to the tyrosine formed in *E. coli* ribonucleoside diphosphate reductase (RDPR); on the other hand, a g_{11} value of 2.00752 for the tyrosyl radical in photosystem II (PSII) has been attributed to the presence of a hydrogen bond at the oxygen of the tyrosine (59).

Figures 2.7 (a) and (b) show the HF-EPR spectra obtained from RFQ samples frozen after 700 ms and 10 s reaction time (mixing with peroxyacetic acid), respectively. The interpretation of the HF-EPR spectra was difficult since, according to subtractions and simulations, the spectra cannot be assigned to a single species. The intensity centered around g = 2.007 in Figure 2.7 spectrum (b) suggests a g_{11} value reminiscent of strongly hydrogen bonded tyrosyl radicals (59), even though it has also been suggested that a weakly hydrogen bonded tyrosyl radical coupled to an oxyferryl species (S = 1, Cmpd I) can give similar g_{11} values (60). Moreover, spectrum (b) in Figure 2.7 resembles a HF EPR spectrum published for tysosyl radical in PGHS (60). Both spectra are characterized by a g_{11}-edge that is continuously distributed unlike the narrow g_{11} feature observed for other tyrosyl radicals (60). In the case of PGHS, a similar broad g_{11} feature was suggested to be consistent with a collection of orientations of the phenol ring with respect to the protein backbone. Each rotamer in this collection would have a different g_{11} value that represents a variation in the strength of a hydrogen bond to the oxygen of the tyrosyl radical. The presence of the hydrogen bond limits the orientational freedom of the phenol ring around the C1-Cβ single bond. In the case of *M. tuberculosis* KatG, the resemblance with the PGHS spectra may suggest a similar behavior of the tyrosyl radical, but a confirmation awaits further HF-EPR experiments.

Reproduced with permission of the copyright owner. Further reproduction prohibited without permission.

Spectrum (b) reported in Figure 2.7 for the *M. tuberculosis* KatG enzyme also resembles the HF-EPR spectra found for *Synechocystis* KatG reacted with peroxide (61). That spectrum has been assigned to a combination of a tyrosyl radical signal (g values equal to 2.0064, 2.0040 and 2.0020) overlapped with a tryptophanyl radical. In the *Synechocystis* KatG spectrum, extra intensity at the g_{33} component that cannot be assigned to tyrosyl radical was assigned to the contribution from a tryptophanyl radical signal (61). A similar extra feature can be observed in the spectrum of the *M. tuberculosis* KatG ezyme (elipse in Figure 2.7 (b)). This observation suggests that the second radical present in the HF RFQ-EPR spectra of the *M. tuberculosis* KatG enzyme is most likely a neutral tryptophanyl radical.

The HF-EPR spectra of *M. tuberculosis* KatG spectrum freeze-quenched at 700 ms (Figure 2.7 (a)) shows a higher contribution of the tryptophanyl species in the g_{22}, g_{33} region compared with the spectrum quenched after longer time (spectrum (a)). Preliminary estimates based on the subtraction of the 10 s spectrum from the 700 ms spectrum show that the spectrum quenched at 700 ms has a 30% greater contribution of the tryptophanyl radical, compared with the sample quenched at 10 s. These results suggest that the tryptophanyl radical is decreasing in intensity while the tyrosyl radical is still increasing in intensity. While this may suggest a mechanistic connection between the two radicals, further experiments are required to investigate if such correlation exists.

When the HF-EPR data together with the results published for *Synechocystis* KatG raised the likelihood of a tryptophanyl radical formed in addition to the tryrosyl radical, a re-examination of the X-band data was undertaken. For example, the spectrum recorded at 250 ms for the [$^2H_2$] tyrosine-labeled enzyme (Figure 2.6) suggests that the residual

Reproduced with permission of the copyright owner. Further reproduction prohibited without permission.

doublet signal intensity most obvious on the high field side of the spectrum could arise from a tryptophanyl radical doublet signal. This kind of signal has been documented for tryptophanyl radical in tyrosine-tryptophan mutations of enzymes that form tyrosyl radicals (61-63).

Simulations reported by Lendzian et al. show that EPR spectra of [$^2H_5$] tryptophan radical have a significant reduction in the linewidth of the doublet signal compared with the non-deuterated radical (55). In the spectrum reported here, the low abundance of the presumed tryptophanyl radical (approximately 20%of total EPR signal intensity) could be responsible for the absence of any significant change observed in the EPR spectrum of the tryptophan-labeled enzyme compared with the unlabeled one.

2.5 Quantitative EPR and Kinetics

The EPR data considered until now have provided important information (for example, about hydrogen bonding and the phenol ring orientation) about the radical and its environment. The same RFQ-EPR samples can be analyzed using quantitative EPR to obtain the yield and the rate of formation of the radical(s).

The yield of the tyrosyl radical (concentration of radical expressed as spins/heme) formed during the reaction with peroxyacetic acid was obtained from the quantitative analysis of the RFQ-EPR spectra (Appendix A). Figure 2.8 shows the total EPR signal intensity (spins/heme) plotted as a function of time. The maximum yield was close to 0.2 spins/heme at 10 s; after 10 s the EPR signal intensity starts decaying. The low yield (less than 1 equivalent/heme) of tyrosyl radical observed may be justified assuming that radical quenching reactions compete with its rate of formation.

Reproduced with permission of the copyright owner. Further reproduction prohibited without permission.

Since we cannot yet confirm the model based on HF-EPR that there exists a collection of ring orientations at any particular time, we present another model considering the formation of the doublet and singlet species as two consecutive irreversible reactions. Moreover, it has already been shown that while the rate of Cmpd I formation depends on both the enzyme concentration and peroxide concentration, the rate of formation of the tyrosyl radical is independent of the peroxide concentration used to initiate its formation from resting KatG (11). The rate of tyrosyl radical formation should depend only on the concentration of the intermediate it is formed from, which is probably Cmpd I (see below). These considerations suggest that overall, the rate of radical production can be treated as two consecutive irreversible first order reactions.

A simple model for simultaneous and consecutive reactions was applied to determine the rates of formation of doublet and singlet based on the following simple scheme:

$$\text{Tyr} \xrightarrow{k_1} \text{Tyr}^{\cdot}\ (\text{doublet}) \xrightarrow{k_2} \text{Tyr}^{\cdot}\ (\text{singlet})$$

where $k_1$and k_2 are the two rate constants to be determined. Assuming that the two reactions are irreversible and first order, and the initial tyrosine concentration is the same as the maximum yield of radical (0.2 spins/heme), two rate equations describe the formation of the doublet and singlet species (64):

$$[\text{Tyr}^{\cdot}\ (\text{doublet})] = (0.2b/(a-b))(\exp[-bx]-\exp[-ax]) \qquad (2.1)$$

$$[\text{Tyr}^{\cdot}\ (\text{singlet})] = (0.2/(a-b))(a\ (1-\exp[-bx])- b(1-\exp[-ax])) \qquad (2.2)$$

Reproduced with permission of the copyright owner. Further reproduction prohibited without permission.

Figure 2.9 shows the simulated curves based on this model, together with the experimental data obtained for the yield of radical formation. The ratio of the two rate constants k_1/k_2 is 0.8 (k_1 and k_2 are 0.4 and 0.5 s^{-1} respectively).

The fitting of the model to the quantitative EPR results is supported by the fact that the percentage of singlet and doublet present at each time point based on the simulated curves agrees well with estimates of the relative abundance of singlet and doublet signal in the spectra recorded for the enzyme reaction quenched at the various time points. For example, the spectrum recorded for the sample freeze- quenched after 2 s incubation time can be simulated as the sum of 50% doublet and 50% singlet; this matches the results obtained from the two-state model reported in Figure 2.9.

The two-state model proposed here would also be adequate to describe the evolution from doublet to singlet also for a case in which two tyrosine residues, give rise to the observed EPR spectra.

More complicated models can also be considered because fast ring flip motions have been reported for tyrosine side chains in proteins based on NMR analyses (65,66). The possibility of detecting these motions with EPR spectroscopy depends on the rate of the fluctuations of the phenol ring compared with the EPR experimental time scale. Since these motions would not be expected to give a net change in orientation of the ring as a function of time, we exclude this kind of motion from our interpretation.

Another issue at this point was to check the kinetics of tyrosyl radical formation in relation to rates measured for other processes in the enzyme. For example, if the radical is formed from Cmpd I, we should observe the disappearance of the resting enzyme occurring faster than the appearance of tyrosyl radical. Therefore, the initial RFQ-EPR

Reproduced with permission of the copyright owner. Further reproduction prohibited without permission.

samples prepared from the unlabeled enzyme were analyzed in the g = 6 region where at 5.5 K it is possible to observe EPR signals due to ferric iron (Appendix B). In the peroxidase cycle of KatG, the resting enzyme is the only species containing ferric iron. Low temperature EPR spectra of the RFQ-EPR samples frozen after mixing the resting enzyme with PAA showed the decay of this species as a function of time. In Figure 2.10, the intensity of the EPR signal at g = 6 was plotted *versus* time (Appendix A). A decrease in the intensity of the ferric heme iron EPR signal is observed from the initial time points through 1s, after which it started to increase. The half time, $t_{1/2}$, for the decay of the ferric heme iron species is estimated to be less than 50 ms under these conditions.

The rate of ferric heme iron disappearance ($t_{1/2}$ < 50 ms) is similar to the rate of Cmpd I formation (Cmpd I evolves directly from ferric enzyme) estimated from optical stopped flow measurements under the same conditions ($t_{1/2}$ = 50 ms) (28) and is faster than the appearance of the tyrosyl radical ($t_{1/2}$ ~ 1.4 s). Cmpd I formation is considered a pseudo-first order reaction because the amount of PAA added was always in excess compared with the enzyme. Moreover, it is already known that the rate of Cmpd I formation is dependent on the peroxide concentration, while the rate of tyrosyl radical formation is not (28). All these observations strongly suggest that the tyrosyl radical formation takes place via an intermediate, most likely to be Cmpd I (Figure 2.11).

This conclusion provides the opportunity to address the issue of the low yield of tyrosyl radical. The tyrosyl radical is directly formed from Cmpd I, but Cmpd I can also react with any H_2O_2 present in the PAA. This competitive reaction rapidly consumes Cmpd I returning it to the resting enzyme before formation of a tyrosine radical.

Reproduced with permission of the copyright owner. Further reproduction prohibited without permission.

Unfortunately, more detailed kinetic correlations between the disappearance of the resting enzyme (ferric heme iron) and the appearance of the tyrosyl radical are impossible to obtain from the EPR data because the EPR signal of the intermediate, Cmpd I, has not yet been detected in *M. tuberculosis* KatG. The reasons for this are not clearly understood at present. Cmpd I was proven to be present in optical experiments at room temperature under conditions similar to those used for preparation of the RFQ-EPR samples. For other enzymes, including catalases and peroxidases, the Cmpd I EPR spectrum has been reported to be either an axial singlet with g-values $g_{\|} \sim 2$ and $g_{\perp} \sim 2.35$ (or $g_{\|} \sim 2$ and $g_{\perp} \sim 3.32$) (61,67) or an isotropic singlet signal at $g \sim 2$ (68).

Temperature- and power-dependence studies did not reveal the EPR signal of Cmpd I in the RFQ-EPR samples of *M. tuberculosis* KatG. The EPR spectra of Cmpd I depend on interactions due to a weak exchange coupling between the porphyrin π-cation radical ($S = ½$) and the oxyferryl iron ($S = 1$) (Appendix B). According to theory, the set of conditions with J/D very small and therefore $g_{\perp eff} \sim 0$ may justify the EPR silent Cmpd I in *M. tuberculosis* KatG (Appendix B). This would be the first example of an EPR silent Cmpd I in a heme enzyme.

2.6 Conclusions

In this chapter, it has been demonstrated that a tyrosyl radical is formed in the *M. tuberculosis* KatG enzyme when treated with peroxide. The radical is most likely formed from Cmpd I oxidation of a single tyrosine residue. Interestingly, double mixing RFQ-EPR experiments have shown that the tyrosyl radical, as well as Cmpd I in *M. tuberculosis* KatG react with INH (11,28). Therefore, it can be argued that the tyrosyl radical is kinetically competent in reactions with substrates, even though we cannot yet say whether

Reproduced with permission of the copyright owner. Further reproduction prohibited without permission.

it plays a fundamental role in drug activation or whether it is responsible for some metabolic reactions *in vivo*.

Figure 2.12 shows the intermediates potentially formed in the catalytic cycle of KatG. The tyrosyl radical is formed via an intermediate assumed to be Cmpd I. Cmpd II is the only intermediate that has not yet been spectroscopically identified in WT KatG, but its formation has been assumed from the analogy with all the other peroxidases.

The research work presented in this chapter has already been published in (28).

Reproduced with permission of the copyright owner. Further reproduction prohibited without permission.

Chapter 3

Chapter 2 described the identification and characterization of tyrosyl radical formation in *M. tuberculosis* KatG in which the hypervalent heme center (Compound I) is the oxidant responsible for its formation. The primary objective of the second part of this research work is the identification in *M. tuberculosis* KatG (Figure 1.2), of the specific tyrosine residue, among the twenty tyrosines present, on which the radical is localized. The first approach adopted to investigate this goal was site-directed mutagenesis. Site-directed mutagenesis can be a very useful technique in the absence of X-ray crystal structures, which was the circumstance with *M. tuberculosis* KatG when we started the investigations. This technique has been used to gain more insight into the mechanism of KatG enzymes from different organisms; in fact, it is a probe for the function of residues assumed to be important in the catalytic cycle and to assign roles in catalase and peroxidase cycles (61,69,70). Site-directed mutagenesis involves the modification of the genetic sequence encoding a protein that results in the substitution of one specific amino acid with another. The properties of the modified and native proteins are then compared to the native one to identify changes that can be related to the function of the mutated amino acid.

In particular, site-directed mutagenesis was used here to identify the tyrosine on which the radical is formed in the WT KatG enzyme by its replacement with a redox-inactive residue such as phenylalanine. Ideally, if the amino acid on which the radical is localized in the wild-type enzyme is mutated, it would eliminate radical formation. In other examples, since the highly reactive metal cofactor (in its hypervalent oxidation states) can be non-selective, the mutations don't necessarily eliminate radical formation.

Reproduced with permission of the copyright owner. Further reproduction prohibited without permission.

Instead, new radicals may be produced on other amino acid residues. Examples of these phenomena are found in ribonucleotide reductase (RNR), cytochrome c peroxidase (CCP) and prostaglandin synthase (PGHS) tyrosine mutants. In these cases, alterations of the kinetics and EPR parameters that characterize radical formation in WT enzyme were usually observed (39,71).

Here, several *M. tuberculosis* KatG mutants were studied. The choice of the sites of mutation had different purposes: some mutants were prepared to help identify the residue on which the tyrosyl radical previously described is localized; other mutants were prepared to aid in understanding the drug-resistance mechanism. These mutants include KatG[Y98F], KatG[Y113F], KatG[Y229F], KatG[Y304F], KatG[Y353F], KatG[Y426F], KatG[Y155S] and KatG[S315T].

3.1 Site directed mutagenesis

As stated in the introduction, to identify the tyrosine residue on which the radical is localized in *M. tuberculosis* KatG, mutations were generated that led to the change of a single tyrosine to phenylalanine. In an attempt to decrease the number of tyrosine-mutant proteins that would have to be screened, a detailed analysis of the position of tyrosine residues among highly conserved KatGs from different organisms and for homologous proteins such as CCP and APX was performed. The logic behind this approach is based on the assumption that the tyrosyl radical has a conserved function in the catalytic activity of the KatGs. According to this homology-based analysis, six *M. tuberculosis* KatG mutants were prepared (by Dr. Shengwei Yu, according to the procedure described in Appendix A): KatG[Y98F], KatG[Y113F], KatG[Y229F], KatG[Y304F], and KatG[Y426F]. When these mutation sites were chosen, there was no 3-dimensional X-ray

Reproduced with permission of the copyright owner. Further reproduction prohibited without permission.

crystal structure available. Residues 98 and 113 were considered to be close to the distal side of the heme pocket, while 304 and 426 were predicted to be in the proximal heme domain. Residue 229 was considered interesting because it is within a sequence of 40 amino acids (from residue 193 to 232) that is an insertion loop absent from other Class I peroxidases that could be responsible for some unusual function in KatGs. When the crystal structure of KatG from *Haloarcula marismortui* was published last year, tyrosine 229 turned out to be the closest tyrosine to the heme iron (10.4 Å), while tyrosines Y98 and Y113 are located approximately 20 Å away from the heme iron. Tyrosines 304 and 426 in *M. tuberculosis* KatG are conserved in *B. pseudomallei*, but not in *H. marismortui* KatG and are located on the distal side approximately 23 Å from the heme.

3.1.1 Characterization of radical formation in KatG[Y98F], KatG[Y113F], KatG[Y304F], KatG[Y426F]

Mutant enzymes KatG[Y98F], KatG[Y113F], KatG[Y304F], KatG[Y426F] were prepared and purified as described in Appendix A for WT KatG. EPR and optical data collected for these mutant enzymes in their resting states didn't reveal any major differences compared with the WT enzyme. Therefore, in order to obtain additional information on these mutants, the RFQ-EPR approach was applied since it could provide both EPR spectra of radicals and the kinetics of their formation.

RFQ-EPR samples were prepared as described in Appendix A for WT KatG, quenching the reaction of each enzyme after mixing with peroxyacetic acid. Figures 3.1 through 3.4 show the X-band EPR spectra recorded at 77 K for RFQ samples prepared for mutant enzymes KatG[Y98F], KatG[Y113F], KatG[Y304F], KatG[Y426F] after reaction with PAA for the time periods reported in the Figures.

Reproduced with permission of the copyright owner. Further reproduction prohibited without permission.

These EPR spectra show an evolution from doublet to singlet that matches the results observed for WT KatG (Chapter 2) in that doublet signals appear at 250 ms and singlet signals at 5 or 10 s. The spectra of the doublet and singlet signals in the mutants are very similar to those for WT KatG. On the basis of these analogies, the signal detected for the mutant enzymes was also assigned to tyrosyl radical(s). Moreover, the similarities in linewidths for these signals and the total radical signal intensity attained (corresponding to approximately 0.2 spins/heme) strongly suggest that the tyrosine on which the radical was formed was the same in these mutant enzymes as in WT KatG. These results led to the conclusion that tyrosines Y98, Y113, Y304 and Y426 are not the sites of radical formation in WT *M. tuberculosis* KatG enzyme nor are these sites required for tyrosyl radical formation. Moreover, optical and stopped flow spectrophotometric results, pursued to check for any changes in mechanism of heme-based reaction with peroxyacetic acid, don't show major differences compared with the native enzyme (data not shown).

3.1.2 Characterization of radical formation in the INH-resistant mutants KatG[Y155S] and KatG[S315T]

The question that led to the EPR study of KatG[Y155S] and KatG[S315T] was the possible loss of tyrosyl radical function as the origin of INH resistance due to these mutations. One of these mutants, KatG[Y155S], was chosen because it involves the substitution of a tyrosine residue. The second INH-resistant mutant considered was KatG[S315T], which is the most common mutation present in more than 50% of the clinically isolated resistant strains (33). The choice of this enzyme that doesn't carry a

Reproduced with permission of the copyright owner. Further reproduction prohibited without permission.

tyrosine mutation was made based on the idea that the resistance may still have been related to the lack of tyrosyl radical formation.

KatG[Y155S] is a conserved residue in catalase-peroxidases, which, according to the recent crystal structure published for KatG (20), is located approximately 29Å away from the heme on the distal side. Therefore, now it seems unlikely that the radical is formed so far from the metal center, but when the experiment was performed the choice for the mutation site was made only on the basis of the amino acid sequence of KatG. RFQ-EPR spectra obtained from the reaction of KatG[Y155S] with peroxyacetic acid (3-fold excess) are shown in Figure 3.5. No evident changes compared with WT KatG were observed either in the kinetics of evolution of the EPR signals, in the maximum yield of tyrosyl radical, or in the EPR parameters that characterize the doublet and singlet signals. Stopped-flow optical data for this mutant also showed behavior similar to WT enzyme (28). Therefore, since the data don't suggest kinetic and mechanistic differences in this mutant enzyme compared with WT KatG, it can be concluded that in KatG[Y155S] the tyrosyl radical is formed on the same residue as in the WT enzyme. Other studies of this mutant (personal communication, S. Yu) suggest that its affinity for INH is reduced, which could contribute to the drug resistant nature of this mutant.

RFQ-EPR spectra obtained from the reaction of KatG[S315T] with peroxyacetic acid (3-fold excess) (Figure 3.6) show no evident changes in the kinetics of formation or in the characteristics of the tyrosyl radical formed compared with WT. Therefore, we can conclude that in KatG[S315T], the tyrosyl radical is also formed on the same residue as in the WT enzyme. Later, it was shown that a greatly reduced affinity of the KatG[S315T] mutant enzyme for the drug is one of the major reasons for drug resistance (33).

Reproduced with permission of the copyright owner. Further reproduction prohibited without permission.

3.2 Characterization of radical formation in KatG[Y229F]

Mutant KatG[Y229F], prepared and purified as described in Appendix A, has been treated separately from the other mutant enzymes since it shows a peculiar behavior that suggests that tyrosine Y229 is a key residue involved in KatG function.

Figure 3.7 shows the EPR spectra recorded for RFQ-EPR samples in the reaction of KatG[Y229F] with a three-fold excess of peroxyacetic acid, at the given time points, as previously described for WT (Chapter 2). A doublet EPR signal appears only at the earliest time point, followed by a singlet EPR signal characterized by the same parameters as WT. Both signals were assigned to tyrosyl radical based on the similarity of these signals to those assigned in WT KatG. Surprisingly, the rate of evolution from the doublet to the singlet signal for mutant KatG[Y229F] was completely different compared with that observed for WT and the other mutant enzymes. Also, at 10 ms, the doublet EPR signal has a much higher intensity than the corresponding signal for WT and has the same linewidth as the doublet signal found in WT KatG freeze-quenched at 250 ms. By 50 ms, however, only the singlet appears, while in WT, the features of the doublet persist beyond 500 ms. The linewidth of the singlet EPR signal in KatG[Y229F] is progressively narrowed (from ~ 20 G to ~ 18 G) going from 50 ms to 5 s. The 18 G wide singlet is narrower than the singlet described in the RFQ experiment for WT KatG at the same time point. This suggests that at 5 s, the contribution of the doublet to the singlet signal is higher in WT than in the mutant. Therefore, in KatG[Y229F], radical formation is accelerated and the evolution from the doublet to the singlet is faster (see below)[2].

Figure 3.8 shows the radical concentration evaluated from the double integration of the RFQ-EPR spectra plotted *versus* time for KatG[Y229F] reacted with PAA. The

Reproduced with permission of the copyright owner. Further reproduction prohibited without permission.

radical concentration increases very rapidly in the first part of the curve reaching a maximum of 0.08 spins per heme at 100 ms. In WT KatG, the maximum radical yield (~ 0.2 spins/heme) occurs at 10 s. The lower yield of the radical formed in KatG[Y229F] compared with the radical in WT could be attributed to a rapid quenching of the radical by secondary electron transfer processes that are different from those in WT KatG. In fact, EPR signal intensity decayed more quickly than in WT.

While it would be useful to calculate a rate for radical formation, the rapid formation of the doublet EPR signal in mutant KatG[Y229F] makes the calculation of the initial rate unreliable because the RFQ instrument used (Appendix A) to prepare the samples doesn't access time points below 6.4 ms, and repeated trials at this short time resulted in the observation of EPR spectra characterized sometimes by doublet and other times by singlet signals. In any case, the rates for the tyrosyl radical doublet and singlet formation in the KatG[Y229F] mutant enzyme have been roughly estimated using the model presented in Chapter 2 for two, first-order irreversible consecutive reactions. The equations used are equations 2.1 and 2.2 with an initial tyrosine concentration normalized for the maximum radical produced in the KatG[Y229F] mutant enzyme (0.08 spins/heme). The rate constant for the formation of the doublet species (k_1) was four times higher than the rate constant for the formation of the singlet species (k_2) and a hundred times higher than the corresponding rate constant for the doublet formation in

[2] The RFQ-EPR samples of the mutant enzymes have been prepared using a three-fold excess of H_2O_2-free PAA which resulted in small changes in the linewidths of the EPR spectra compared with the samples described in Chapter 2 for which commercial PAA, which contained up to 5% H_2O_2, was used. The origin of this phenomenon is not understood, but note that the spectra reported here for the mutant enzymes have been compared with a set of RFQ-EPR spectra for the WT enzyme recorded for samples prepared under identical conditions.

Reproduced with permission of the copyright owner. Further reproduction prohibited without permission.

the WT enzyme. Therefore, assuming that the mutation of tyrosine 229 doesn't alter the site on which the tyrosyl radical is formed in both WT and this mutant, these results lead to the suggestion that an indirect involvement of tyrosine 229 in the radical formation possibly through hydrogen bonding or electron transfer effects occurs in the mutant, as discussed below. Alternatively, these results may be taken as an evidence for the formation of tyrosyl radical on a new residue in this mutant, and the conclusion would follow that the radical seen in WT occurs on Y229. Arguments against this conclusion are given below.

The formation of intermediates in the peroxidase cycle of KatG[Y229F] was investigated using stopped-flow optical experiments. The mutant enzyme was mixed with peroxide and the course of the reaction was monitored following the evolution of the optical spectrum. Values for (k_{obs}) were determined as a function of peroxide concentration by fitting the change in absorbance at a particular wavelength (Soret peak or a maximum in the visible region) to a hyperbolic exponential function. Second order rate constants were determined from the slope of the plot of the observed rates (k_{obs}) calculated for different peroxide concentrations, a standard procedure used in the analysis of peroxidase kinetic measurements (11).

Figure 3.9 shows the evolution of the reaction of KatG[Y229F] (0.1 mM) with peroxyacetic acid (0.3 mM) obtained from stopped-flow optical data. While the initial spectrum has the typical features of the resting enzyme, the intermediate spectrum shows a decrease in intensity of the Soret peak typical of Cmpd I (Chapter 1). The final spectrum shows a red shift of the Soret peak (416 nm), the appearance of features at 530 and 560

Reproduced with permission of the copyright owner. Further reproduction prohibited without permission.

nm, and the disappearance of the CT1 band at 640 nm characteristic of the resting enzyme. The final spectrum strongly resembles the optical spectrum of horseradish peroxidase Cmpd II (Chapter 1). The values of k_{obs} for Cmpd I and Cmpd II formation were calculated from the changes in intensity with time of the features at 409 nm and 416 nm respectively. For Cmpd I formation, k_{obs} was linearly dependent on peroxide concentration, consistent with formation of this intermediate directly from the initial turnover with peroxide. The second order rate constant for this reaction was calculated to be 4×10^6 $M^{-1}s^{-1}$. This rate is 330-fold higher than the value reported by Chouchane et al. (11) for WT KatG (1.21×10^4 $M^{-1}s^{-1}$). For Cmpd II formation, k_{obs} was equal to (13.5 ± 0.5) s^{-1}. Cmpd II features persisted for at least six minutes before the spectrum of the resting (ferric) state began to reappear.

Related results were recently published in a study of mutant KatG[Y249F] of *Synechocystis* KatG (Y249 corresponds to tyrosine 229 in *M. tuberculosis* KatG) showing spontaneous formation of Cmpd II (k_{obs} = (0.6 ± 0.1) s^{-1}) was much slower than for *M. tuberculosis* KatG[Y229F] (72). These variations may reflect differences between number and locations of the tyrosines residues in the two mutant enzymes.

It is noteworthy to recall that WT KatG does not exhibit the optical spectrum of Cmpd II under the conditions described above. Therefore, mutant KatG[Y229F] allowed for the first time the identification of the features that characterize this intermediate in *M. tuberculosis* KatG.

The data analyzed up to this point suggest that the mutation of tyrosine 229 not only induces an alteration of the kinetics of tyrosyl radical formation, but also of the kinetics of the overall peroxidase cycle including a more rapid formation of Cmpd I and a

Reproduced with permission of the copyright owner. Further reproduction prohibited without permission.

slower decay of Cmpd II. Since both EPR and optical data were collected for this mutant, it was interesting at this point to probe the mechanism of radical formation based on kinetics. Figure 3.10 shows the yield of tyrosyl radical (previously reported in Figure 3.8), along with a plot of the change in intensity at 560 nm, which is a feature of the Cmpd II spectrum, obtained from stopped- flow experiments (0-0.5 s). The similarity in the time courses in these two plots ($t_{1/2} \cong 50$ ms for both), suggests that radical and Cmpd II formation are kinetically coupled. Kinetic data presented in Chapter 2 suggested that in WT KatG, the tyrosyl radical was formed in a reaction involving an intermediate most likely to be Cmpd I; but in WT KatG no Cmpd II could be observed. Therefore, no correlation between the reduction of Cmpd I and Cmpd II formation could be drawn. For mutant KatG[Y229F], the demonstration of equivalent rates for Cmpd II and tyrosyl radical formation strongly suggest that endogenous electron transfer from tyrosine to Cmpd I leads to the formation of tyrosyl radical and Cmpd II (Figure 3.11; compare also with Figure 2.11). Whether this applies also to WT KatG remains without direct evidence. (Indirect evidence for the presence of Cmpd II in WT enzyme comes from the observation that Cmpd III is produced when resting enzyme is treated with a large excess of hydrogen peroxide in analogy with a pathway known to occur in HRP (73)).

The information available until this point, namely that the kinetics of the peroxidase cycle, including tyrosyl radical formation, are altered compared with the WT enzyme led to two hypotheses: tyrosine 229 could be the residue on which a radical forms in WT KatG; or Y229 is tightly associated with another tyrosine on which the radical forms, for example through electron transfer or hydrogen bonding. If the first hypothesis is correct, the replacement of Y229 with a phenylalanine would either eliminate radical

Reproduced with permission of the copyright owner. Further reproduction prohibited without permission.

formation or lead to its formation on another tyrosine residue that may or may not present a different EPR spectrum. The second hypothesis might be consistent with a hydrogen bond between Y229 and the key tyrosine, which in the mutant is absent, releasing the steric constraint that holds the phenolic ring in a fixed orientation. This would result in faster conversion from the doublet to the singlet signal.

The crystal structures of KatG from *H. marismortui* and *B. pseudomallei* published last year provided us with the structure of the region surrounding tyrosine 229. The structure showed that tyrosine 229 is covalently attached to a methionine and a tryptophan side chain in an unusual adduct on the distal side of the heme. The adduct, illustrated in Figure 1.4, shows that the tyrosine (218 in *H. marismortui* corresponds to tyrosine 229 in *M. tuberculosis* KatG) is covalently bound to a methionine and a tryptophan through the phenol ring carbons, 3' and 5'. This indicates that protons H3' and H5' are missing and could not contribute to the secondary hyperfine coupling observed in the EPR spectrum of such a modified residue if it were converted to a tyrosyl radical (Chapter 2). In order to help understand whether the tyrosyl radical observed in the WT enzyme could have been generated on the Y229 tyrosine, EPR simulations were produced to illustrate the spectrum that would be observed for a tyrosyl radical missing the 3' and 5' hydrogens (Figure 3.12). The comparison of this simulation with the doublet EPR signal obtained for WT KatG (not shown) eliminated the possibility that a modified Y229 residue could be the residue on which the tyrosyl radical forms during the turnover of WT KatG with peroxide. The second hypothesis about the possible existence of a hydrogen bond between tyrosine 229 and the key tyrosine forming a radical in WT KatG, may also be invalidated because there is no nearby tyrosine in the crystal structure. The

Reproduced with permission of the copyright owner. Further reproduction prohibited without permission.

data available suggest therefore that the only possibility for tyrosine Y229 to be the main residue on which the radical is formed in the WT enzyme is that its side chain is not incorporated into the adduct in the *M. tuberculosis* KatG enzyme used in the RFQ-EPR experiments. This last idea is contradicted by optical stopped-flow results demonstrating a change in mechanism in KatG[Y229F] very similar to that reported for the homologous mutant KatG[Y249F] in *Synechocystis* KatG (72), an enzyme proven to contain the adduct. It is also possible that only a certain percentage of the protein as isolated contains the adduct. This idea is supported by a recent mass spectroscopy study on *B. pseudomallei* KatG that confirmed that the adduct is not formed in all the subunits of the enzyme (74). Support for these hypotheses awaits the *M. tuberculosis* KatG crystal structure and more detailed studies on the adduct.

The changes in the mechanism of the mutated enzyme compared with WT are difficult to explain, but they suggest that residue Y229 (and the adduct) serves to prevent the formation of Cmpd II, which is inactive for catalase activity but active in the peroxidase function of the enzyme. This is based on experimental results reported in (75). The mutation of tyrosine 229 facilitates formation and stabilization of Cmpd II and thereby induces an increase of the peroxidase activity and a loss of catalase activity. Similar modification of the catalatic activity of the enzyme was observed for mutation of the tryptophan residue involved in the formation of the covalent adduct (70). Therefore, the ultimate function of the adduct is suggested to be the provision for the catalase activity of the enzyme (75).

3.3 Characterization of radical formation in KatG[Y353F]

Reproduced with permission of the copyright owner. Further reproduction prohibited without permission.

The mutation of the seven amino acids described above didn't lead us to the identification of the tyrosine residue on which the radical is formed in the WT *M. tuberculosis* KatG enzyme. Therefore, in a further attempt to reach our goal, labeling with nitric oxide, followed by mass spectroscopy analysis was undertaken. Y353, which was converted to nitrotyrosine in these experiments, was concluded to be the site of radical formation (76). Surprisingly, tyrosine 353 is not conserved in other KatGs where it is substituted by a tryptophan and, less frequently, by a phenylalanine. In *H. marismortui* and *B. pseudomallei*, Tyr 353 of the *M. tuberculosis* enzyme is found as a tryptophan residue whose side chain is located approximately 15 Å from the heme iron. In an attempt to better understand the issues related to tyrosyl radical formation, stopped-flow and RFQ-EPR experiments on the KatG[Y353F] mutant enzyme prepared using site directed mutagenesis (Appendix A) were undertaken.

Figure 3.13 shows the RFQ-EPR spectra obtained after reaction of the mutant enzyme with PAA under the same conditions and according to the same procedure described in Appendix A for the WT KatG enzyme. A radical is formed and the evolution from a doublet to a singlet signal as well as the other EPR parameters closely resemble the data already reported for the WT enzyme. Therefore, this radical was also assigned to a tyrosyl radical. However, the evolution from the doublet to the singlet signal was slower than in the WT enzyme. In fact, the spectrum recorded for the mutant 10 s after mixing with PAA shows a contribution of the doublet to the overall spectrum that is approximately 25-30% higher than what was observed in the WT enzyme at the same time point. This is taken as clear evidence that the rate of the conversion from doublet to singlet is slower in KatG[Y353F] than in the WT enzyme.

Reproduced with permission of the copyright owner. Further reproduction prohibited without permission.

Another difference observed for mutant KatG[Y353F] compared with the WT enzyme was the very low yield of radical (0.05 spins/heme). The maximum yield of radical in mutant KatG[Y353F] was found at 100 ms (Figure 3.14). This value is 27% of the maximum radical yield reported for WT occurring at 10 s (see Chapter 2). The data available on this mutant therefore, suggests that even though a pathway for tyrosyl radical formation still exists in the KatG[Y353F] mutant, the oxidation of a different tyrosine residue occurs with a significantly lower efficiency and its decay is also accelerated. These results strongly suggest that the principal radical site in the WT enzyme has been altered by the mutation of Y353 to phenylalanine.

Peroxyl radical formation

In Chapter 2, the appearance of a small signal at g ~ 2.03 in certain RFQ-EPR samples, tentatively assigned to a peroxyl radical, was mentioned. RFQ-EPR spectra of mutant KatG[Y353F] show a significant contribution from the same signal, with g values $g_z = 2.03$, $g_y = 2.006$, $g_x \sim 2.00$. For the purpose of quantifying the yield of this radical, its signal was resolved from spectra that also contained a contribution of tyrosyl radical, by subtraction of the tyrosyl radical signal from data in which both signals were found. Its intensity is at a maximum at 10 ms (0.034 spins/heme) and then rapidly decays; at 250 ms it is less than 0.005 spins/heme and at 10 s the signal at g = 2.03 cannot be detected. The peroxyl radical observed could be an amino acid based peroxyl radical or a peroxide based peroxyl radical. A suggestion that this radical is formed in a side reaction comes from a RFQ-EPR experiment performed on the WT KatG enzyme. A sample of WT KatG enzyme was mixed with peroxyacetic acid in ratio 1:10 incubated for one hour at 4 °C. The enzyme was then exchanged into phosphate buffer and was then used in rapid freeze-

Reproduced with permission of the copyright owner. Further reproduction prohibited without permission.

quench protocols with peroxyacetic acid according to the procedure previously described for WT KatG. The EPR spectra recorded for two samples, 250 ms and 5 s after mixing, are reported in Figure 3.15. They both show only the formation of a peroxyl radical (g_z = 2.03, g_y = 2.006, g_x ~ 2.00) similar to the one observed in the RFQ-EPR spectra for the KatG[Y353F] mutant. These results may suggest that the treatment of the enzyme with a high concentration of peroxyacetic acid disrupts the enzyme at tyrosine Y353. Dimerization by covalent bond formation between two tyrosines has been reported for example in Lactoperoxidase (77). These observations suggest that the peroxyl radical observed in the RFQ-EPR spectra of the KatG[Y353F] mutant enzyme is the result of a side reaction occurring when the key tyrosine is unavailable. The previous suggestion would lead to the conclusion that the tyrosyl radical formed in the mutant is not located on the same tyrosine residue as in the WT enzyme.

It is possible to conclude that the significant increase of peroxyl radical yield in the RFQ-EPR spectra of the KatG[Y353F] mutant compared with WT enzyme confirms that the mutation of the tyrosine Tyr353 disrupts the native mechanism for tyrosyl radical formation.

3.4 Conclusions

The results described in Chapter 2 provided the details of tyrosyl radical formation in WT KatG, which enabled interpretation of data in which radical formation was examined in mutant enzymes (this Chapter). The combined results presented in this chapter point toward tyrosine Y353 as the principal site of radical formation in the *M. tuberculosis* KatG enzyme. However, the possibility that a tyrosyl radical could be formed on tyrosine Y229 has not been ruled out. Moreover, since the possibility still

Reproduced with permission of the copyright owner. Further reproduction prohibited without permission.

exists that the doublet and the singlet signals observed upon radical formation can be assigned to two different tyrosines both Tyr 353 and Tyr229 may be involved in the process of radical formation in the *M. tuberculosis* KatG enzyme. Crystal structure data on the *M. tuberculosis* KatG enzyme and eventually more details on the mechanism of adduct formation will be helpful in the future to answer these open questions about the enzyme.

The research work presented in this chapter has already been published in (33,75,76).

Reproduced with permission of the copyright owner. Further reproduction prohibited without permission.

Chapter 4

In this chapter, a detailed characterization of ferric KatG is presented based on the application of EPR and optical techniques. The structural insights are developed from an analysis of the data for *M. tuberculosis* KatG under different conditions including those used for purification, storage, and as a function of pH and ligand binding. The aims include learning about 1) origins of heme structural heterogeneity that involves interchangeable species that can be altered by different effects such as pH; 2) effects on heme structure of weakly coordinating sixth ligands and small molecule binding; and, 3) an intermediate spin state (S = 3/2) that can be related to special heme structures.

The studies combined observations gathered using EPR spectroscopy, optical spectroscopy, and resonance Raman spectroscopy. Resonance Raman data on *M. tuberculosis* KatG samples prepared in our laboratory were collected in collaboration with Dr. J. P. M. Shelvis at NYU. Besides the general characterization of this enzyme under different conditions, this analysis provided some knowledge about the geometry of the KatG active site in the absence of a crystal structure. The major conclusions in this chapter are related to the finding that the structural parameter that ultimately defines much of the spectroscopy of KatG involves the distal imidazole and the sixth ligand water molecule. An emerging part of this story is an attempt to correlate observations from the different spectroscopies, as certain techniques provide information that others may not.

The active sites of catalase-peroxidases in their resting state are ferric heme complexes, in which iron can be penta or hexacoordinate and in various spin states due to the multiplicities of the d^5 systems. The classical example of a peroxidase in its "native" state (in the absence of exogenous ligands) is the 5-c HS heme of HRP. This species and

Reproduced with permission of the copyright owner. Further reproduction prohibited without permission.

all the other heme peroxidases contain a histidyl imidazole as the fifth ligand to heme iron (7). Water coordination to heme iron at the sixth position of the heme iron complexes is also known to occur in most heme proteins and enzymes in native and other forms. The most common six-coordinate form for these proteins is the HS ferric aquo complex in which a water molecule is bound to the iron in the sixth position as typified by the ferric globins, and lignin peroxidase (78,79). Low spin species include those 6-c complexes bearing strong field exogenous or endogenous ligands such as hydroxide, cyanide, or imidazole (80). The intermediate spin state (S = 3/2) is uncommon in heme proteins (never found as the pure state), but evidence for it may be found in cases where spin admixture with S = 5/2 occurs to give a unique quantum mechanical admixture of spin states (QS) (see Appendix B). Some controversy about this spin state exists and will be discussed in this chapter.

The predominant spin state observed for a specific enzyme is a sensitive function of the structure of the heme complex usually governed by the distal side structure. It has been shown that the ground spin state depends strongly upon the sixth axial ligand type and also on the geometry of the equatorial ligand field provided by the pyrrole nitrogens of the porphyrin macrocycle. The equatorial geometry varies because the porphyrin macrocycle can distort into different shapes including saddled, ruffled or domed (7). At this point, while the literature on model systems and heme proteins and enzymes is very extensive, the establishment of a well-defined correspondence between geometry, nature of axial ligand, and spin state is still being developed. Computational studies on model compounds have been made in an attempt to establish this correlation firmly, but a definitive and reliable correspondence between spin states and heme geometry (more

Reproduced with permission of the copyright owner. Further reproduction prohibited without permission.

specificially distortions away from planarity) has not been defined yet (81). Examples are accumulating in the literature, however, and we take advantage of much of the work on other systems for interpretations about KatG.

The ultimate goal of the experiments described in this chapter was to establish a relationship between heme structural features defined through spectroscopic approaches, and other factors such as solution conditions, and, most interestingly, the binding of isoniazid to KatG. This analysis led to an idea that has not been investigated in detail for catalase-peroxidases: the geometry and coordination of the active site of the enzyme depends not only on a change in the axial ligands of the heme iron, but also on binding of a small molecule in a special binding site removed from the heme. Relatively few other examples have been reported about small ligands that influence heme coordination and conformation in peroxidases yet don't bind directly to the heme iron, though examples exist for HRP and $P450_{cam}$ (82,83).

4.1 EPR analysis of KatG examined during purification and storage

Spectroscopic data (EPR, Raman and optical) published elsewhere reported that purified overexpressed *M. tuberculosis* KatG enzyme consisted of a mixture of five-coordinate (5-c) and six-coordinate (6-c) high spin (HS) heme iron, with a large component of low spin (LS) heme (84). Our preliminary work instead shows that the enzyme is mainly in 5 –c HS forms (32). Since unavoidable and easy spin and coordination number changes however had been observed in our laboratory during the purification and storage of KatG even for relatively short periods of time, a detailed EPR study of *M. tuberculosis* KatG was undertaken simultaneously with an optical analysis and a Raman study to better characterize the phenomenon. Figure 4.1 presents low

Reproduced with permission of the copyright owner. Further reproduction prohibited without permission.

temperature EPR spectra of *M. tuberculosis* KatG in phosphate buffer at different stages of purification and after different periods of storage. The complexity observed did not allow a straightforward assignment because there appeared to be a combination of rhombic and axial signals contributing features around g = 6. In order to simplify the assignment, temperature- and power-dependence of the EPR signals, together with an analysis using difference spectroscopy (not shown), allowed the assignment of g_{max} and g_{mid} components of particular signals in a systematic manner. The resulting g-values for four EPR signals are given in Table 4.1. Note that the g = 2 region was not analyzed in great detail after the realization that a Cu(II) signal often contaminated this region of EPR spectra.

The next level of analysis involved possible assignment of spin states and heme iron coordination number to the various signals. For this aspect, we relied on conventions developed in the literature that axially symmetric EPR signals are associated with hexacoordinate HS ferric heme complexes (as found in globins and lignin peroxidase) while penta-coordinate high spin (or possibly QS) ferric hemes exhibit rhombically distorted EPR signals. Small rhombic distortions have also occasionally been assigned to 6-c species (85,86).

Signal r_1 (g_1 = 6.3, g_2 = 5.14 and g_3 ~ 2) in the *M. tuberculosis* KatG spectra reported in Figure 4.1, is considered to be an example of a signal that arises from a 5-c HS heme. A second signal, r_2 ($g_\perp$ ~ 5.8, $g_{||}$ ~ 2), is considered more typical of 6-c HS heme species. A third species r_3 (g_1 = 6.6, g_2 = 5.0 and g_3 ~ 2) was assigned to another 5-c HS form. Signal r_4 with a small rhombic splitting (g_1 = 6.04, g_2 = 5.6 and g_3 ~ 2) could be assigned to an atypical 6-c species (see below)[3].

Reproduced with permission of the copyright owner. Further reproduction prohibited without permission.

The appearance of this spectrum of resting KatG does not completely agree with data presented by Wengenack et al. (31) for another overexpressed KatG preparation. In that study, signal r_1 was not found (but was seen in EPR spectra of the mutant enzyme, KatG[S315T]). The absence of the r_1 signal, according to the analysis reported in this chapter, is related to different conditions used for preparation and storage of the enzyme. In fact, it has been observed that in the stored protein (protein that has been stored for more than one week at 4 ° C after purification) the relative intensity of signal r_1 is very low, while it is the predominant EPR species in the fresh enzyme. Since these differences between fresh and stored enzyme had never been reported for catalase-peroxidases, comparisons between different samples and the results from different laboratories became problematic. Based on these observations, it was decided to pursue a more focused analysis of the influence of storage, pH, anionic ligand binding, and small molecule binding. Some agreement between EPR and Raman observations in preliminary studies suggested that we might be able to make good progress toward understanding the heterogeneity and structural issues for KatG.

A set of EPR spectra recorded for WT KatG under different conditions is shown in Figure 4.1. Spectrum (a) was recorded for the fresh, partially-purified enzyme (immediately after the first chromatographic column, Appendix A) and it contains almost exclusively signal r_1 with some features due to a low intensity of signal r_4. Therefore, it can be argued that the native structure of KatG could be exclusively 5 coordinate, as

[3] The spin state and coordination number assignments are not definitive, but they did provide a framework that allowed for comparison and some interpretation because it was possible to follow changes in spectroscopic signatures in three techniques and then assign trends for changes from 5-c to 6-c.

Reproduced with permission of the copyright owner. Further reproduction prohibited without permission.

would be typical of most other peroxidases based on similar EPR signals in well characterized examples (7,32).

Spectrum 4.1 (b) was recorded for the fresh, fully purified enzyme (after the third chromatographic column, Appendix A) and it shows an increase in the contribution from signals r_2 and r_4, consistent with formation of 6-c heme. The 6-coordinate species represented by signal r_4 is tentatively assumed to contain a water molecule bound to high spin heme iron, which is the most common form for hexacoordinate heme proteins and usually gives axial or slightly distorted features in EPR spectra in the g = 6 region.

Spectra (c) and (d) in Figure 4.1 were recorded after storing the enzyme at 4 ° C in phosphate buffer for 3 and 10 weeks, respectively. The progressive decrease in intensity of the r_1 signal is observed in these two spectra together with the predominant r_2 and r_4 signals confirming the idea that the 6-c species accumulates due to an undefined structural change. The difference between signals r_1 and r_3, both assigned to pentacoordinate forms of the enzyme, is associated with structural differences that are not yet assigned or understood. The enzyme is a dimer of identical polypeptide subunits and this kind of mixture could be a reflection of slightly different heme structures in each subunit of a dimer.

Two other techniques have been used to address coordination number and spin states in samples prepared as described above for the EPR analysis. The optical spectrum of *M. tuberculosis* KatG has two features that are sensitive to heme iron coordination number: the Soret band and the CT1 band (see Chapter 1). The Soret band shifts from 404 nm to 408 nm during the steps of purification and storage, and the CT1 band blue-shifts from 640 nm to 630 nm under the same conditions. These shifts are consistent with

Reproduced with permission of the copyright owner. Further reproduction prohibited without permission.

conversion of the heme iron from penta to hexacoordinate, a trend similar to that concluded from the EPR results. While optical spectra of KatG seemed to represent homogeneous population of heme species, the resonance Raman results say otherwise.

Resonance Raman spectroscopy has also been widely used to identify coordination numbers and spin states in a variety of heme proteins and enzymes, based on a collection of assignments of porphyrin macrocycle vibrational modes, and axial ligand vibrational modes. The most relevant Raman band for the purposes of the present analysis is the ν_3 band, which is sensitive to spin state and coordination number. KatG (both the fresh and older enzyme) shows three ν_3 components; 1487, 1495, and 1503 cm^{-1}, rather than a single species. The band at 1495 cm^{-1} is typical of a 5-c HS ferric heme; the band at 1487 cm^{-1} is attributed to a 6-c ferric heme not exactly typical of 6-c HS forms, and the vibration at 1503 cm^{-1} that could be interpreted as a 6-c LS heme species or as a 5-c quantum mechanically mixed spin (QS) species, was, after detailed analysis, attributed to a 5-c QS heme species (see below and) (87). Estimates of the relative abundance of three species based on the Raman spectra of KatG presented above suggest that the 5-c HS species is constant, while the 6-c species is greater in the stored enzyme compared with the fresh enzyme. Here again, the data points out an evolution from 5-c heme iron to 6-c heme iron during handling/storage of KatG.

In the recent past, the presence of the QS spin state has being recognized in different enzymes and in many Class III peroxidases (88), but the identification of a QS state in *M. tuberculosis* KatG (suggested by the ν_3 band at 1503 cm^{-1}) represents the first case of a quantum mechanically admixed spin state in a Class I peroxidase. Raman

Reproduced with permission of the copyright owner. Further reproduction prohibited without permission.

spectroscopy has developed as a tool that can diagnose this spin state based on the frequency of a ν_3 band, intermediate between its position for HS and LS forms. Other techniques, such as magnetic susceptibility, Mössbauer and NMR spectroscopy, have also been applied but there is still some controversy about QS heme spin states. For heme enzymes, there is an abundance of spectroscopy but not a large body of work in which several techniques have been used on identical samples to provide proof. Here, some history and current perspective on this issue is presented.

The first identification of an unusual magnetic state in a ferric heme system was made in 1974 by Maltempo in the bacterial heme protein ferricytochrome *c'* (89). He claimed that the unusual magnetic properties of this protein (based on EPR and magnetic susceptibility data) could be attributed to a ground-state heme-iron electronic configuration giving a unique quantum mechanical admixture of an intermediate (S=3/2) spin state and a high spin (S=5/2) state. He showed that this QS state is different from a thermal mixture of the two spin states and is instead a single species with magnetic properties distinct from either pure spin state, in which the 3/2 and 5/2 states are close in energy. The mechanism considered responsible for the mixing of these spin states is the spin-orbit coupling interaction, which competes with the crystal field splitting energy. A more detailed theoretical description of the origin of the QS spin state can be found in Appendix B.

From the experimental point of view, Maltempo gave some guidelines for the identification of the QS spin state in pentacoordinate heme of HRP based on resonance Raman, EPR and Mössbauer spectroscopy. More recently, criteria for the identification of the QS state have been modified based mostly on empirical findings; moreover, the QS

Reproduced with permission of the copyright owner. Further reproduction prohibited without permission.

spin state has recently been assigned to a hexacoordinate heme peroxidase also (86). The current criteria for assignment of the QS state in a 5-c heme complex include: i) electronic absorption spectra similar to those of a 5-c HS heme but with shorter wavelength $\pi \rightarrow \pi^*$ (Soret peak) transitions; ii) a CT1 charge-transfer band between 630-635 nm (which is blue shifted compared to 5-c HS forms); iii) high frequency of the resonance Raman core size marker bands (ν_3 included); and iv) EPR spectra (axial or rhombic) with g_{ave} values in the range $4 < g_{ave} < 6$. The 6-c QS state is instead characterized by: i) an electronic absorption spectrum similar to that of a 6-c HS heme. It differs from the 5-c QS in that the Soret band red-shifts by about 4 nm and sharpens with a ~ 35% increase of the extinction coefficient; ii) high frequency of the resonance Raman core size marker bands, which are closer to a 5-c HS model compound than a 6-c HS heme; iii) EPR spectra with g_{ave} values in the range $4 < g_{ave} < 6$ (86). These criteria have to be simultaneously met by a single sample for a resonable assignment of the QS spin state. Right after the first report about QS heme (89), arguments began on the possible structural origin or cause for this unusual spin state. The issue of saddling and other heme deformations has been raised as an important feature though a weak axial ligand field was originally suggested (see Appendix B).

EPR and resonance Raman spectroscopic analysis reported prior to the digression regarding the QS spin state, led us to conclude that the heme in *M. tuberculosis*. KatG exhibits an unavoidable heterogeneity in coordination and spin state under most conditions, and heme coordination shifts from 5 to 6 during purification and storage even for short periods of time. The above analysis suggests that the origin of the heterogeneity

Reproduced with permission of the copyright owner. Further reproduction prohibited without permission.

in KatG could be ascribed to partial conversion to 6-c heme due to water coordination that will be shown below depends on pH and other factors. Examination of the two recently reported X-ray structures reveals a network of hydrogen bonded water molecules within and extending beyond the distal side of the heme iron to the periphery of the heme including a water molecule directly above the heme iron at a distance of 2.54 Å (Figure 4.2). The results presented here suggest that the position of a potential sixth ligand water molecule and other waters in the active site give rise to a heterogeneous structure in this enzyme. Issues such as the possible coordination of weakly binding anionic ligands contributing to the heterogeneity are considered further below.

The evolution of a 6-c species seen during the time required for purification and then during storage may be related to alterations in the structure of the active site or in regions remote from the heme that affect the structure of the heme pocket. One important issue that may explain this suggestion is the covalent amino acid adduct found in the distal pocket of the two KatG enzymes for which crystal structures are available (Figure 1.4). It seems likely that water coordination is dependent on the presence of this adduct especially since the indole nitrogen of the tryptophan residue of the adduct is hydrogen bonded to a water molecule in turn bonded to the water directly above the heme iron (Figure 4.2). Furthermore, the position of the tryptophan could be different when it is incorporated into the adduct compared to when it is free. Finally, if only a certain fraction of the KatG enzyme population contains adduct, then only a fraction of enzyme has the appropriate network of water molecules to give a 6-c complex. In fact, recent results reported for adduct formation in *B. pseudomallei* KatG show that the adduct is not present in the entire population of enzyme molecules (74). This would explain the structural origin for

Reproduced with permission of the copyright owner. Further reproduction prohibited without permission.

an evolving species we observed during purification and storage. If it is assumed that the presence of the adduct also influences other side chains in the distal pocket (for example the pK_a, of the distal imidazole, which is also involved in the hydrogen bonding of water molecules above the heme iron), then there may be a connection between the presence of the adduct and the ligand binding properties (90).

4.2 pH dependence of ferric KatG EPR spectra

The three panels in Figure 4.3 show the EPR spectra of KatG during different stages of purification or storage: fresh, partially purified (Panel A), fresh, fully purified (Panel B) and fully purified and stored for 3 weeks (Panel C). Each panel shows spectra recorded for samples prepared in buffers at three different pH values: pH = 5 (citrate buffer), pH = 7 (phosphate buffer), and pH = 10 (carbonate buffer). (It was assumed that the anions of these buffers do not coordinate to heme iron). Here is a clear example of the complicated pattern of overlapped EPR signals and their changes under different conditions that is very difficult to interpret. At pH 10, the simultaneous presence of all the components is evident and a significant increase of the shoulder at g = 5.7 (g_2 of the r_4 signal) relative to the other components is clearly observed. Ignoring for a moment all the other features, this increase confirms a possible increase in the population of the QS spin state especially since a net increase of the 1503 cm^{-1} band and a corresponding decrease of the 6-c HS species was observed in Raman spectra at pH 10. Interestingly, a complete transition from a heterogeneity of spin states to a pure QS heme has been reported in the case of barley peroxidase at high pH (88).

It is also interesting to observe that a decrease of the pH from 7 to 5 induces an increase of the 6-c HS species (r_2 signal) and the disappearance of the r_3 signal (5-c) in

Reproduced with permission of the copyright owner. Further reproduction prohibited without permission.

KatG. The lower pH apparently favors the binding of a water molecule to the heme iron. This conclusion is considered reasonable because citrate is unlikely to coordinate to heme iron, and therefore, anion binding cannot be the origin of the change in the spectrum. Since lowering the pH caused the conversion to nearly a unique structural species, it might be concluded that at least part of the heterogeneity is due to a structural change that has a pK_a in the range of 5-7. This most likely involves the protonation state of the distal imidazole. It is possible that when the distal imidazole carries a positive charge, it adjusts its conformation by forming a new interaction with another residue nearby, and allows a water molecule to bind tighter to the heme iron (Figure 4.4).

Resonance Raman and optical data collected from similar *M. tuberculosis* KatG samples confirm the observation that the 6-c form is favored at low pH (not shown).

4.3 Anionic ligand binding to ferric KatG

Fluoride has been traditionally used in heme protein spectroscopy because it binds tightly to iron and produces a 6-c HS form (32,87,91). The binding of chloride was also investigated because NaCl is used in a relatively high concentration (0.3 M) to elute KatG from ion exchange media during the purification process; moreover, chloride binding to heme iron in CCP has been reported (91).

Figure 4.5 (b) shows the EPR spectrum obtained after the addition of a large excess of NaF to the fresh partially purified KatG enzyme: an intense 6-c HS signal (r_2) assigned to the KatG-fluoride complex is observed (with a shoulder at $g = 6.3$ that can be attributed to a small portion of the 5-c HS heme (signal r_1) remaining without fluoride bound). An incomplete conversion of the fresh enzyme to the 6-c HS fluoride complex was also found in Raman and optical spectra for the fresh partially purified enzyme under

Reproduced with permission of the copyright owner. Further reproduction prohibited without permission.

similar conditions (32,87). This may be interpreted to reflect the same heterogeneity reported above due to incomplete formation of the adduct and therefore, a mixed population of distal imidazole/imidazolium species.

Chloride binding to KatG was initially studied adding an excess of NaCl to the fresh partially purified KatG enzyme to deliberately produce a chloride complex. Despite a large amount of investigation and data analysis, the results of studies in which high concentration of chloride was used left some questions unanswered. The results did provide evidence for a unique 6-c QS heme species.

The spectrum recorded for the sample of KatG treated with NaCl (Figure 4.5 (c)) shows the presence of a low intensity signal, r_1, due to a 5-c form and the 6-c axial signal, r_2, together with a shoulder at g = 5.7 (r_4). (The fresh enzyme before chloride addition (Figure 4.5 (a)), had a high intensity r_1 signal with $g_1 = 6.3$ and a smaller contribution from the r_4 signal). These observations are consistent with some conversion of 5-c HS species to a 6-c form (HS or QS heme). These results may be contrasted with those for fluoride in which nearly complete conversion to 6-c HS form occurred.

Optical spectra of the fresh partially purified enzyme before and after the addition of chloride ion show changes typical of production of 6-c species, but the blue-shift of the CT1 band and the red-shift of the Soret peak (one nanometer) is minimal, compared with the 20 nm shift observed for the CT1 band in the case of fluoride addition (data not shown).

These results may be consistent with a slow binding of chloride to the heme iron under these conditions with the partially purified enzyme. This can be understood based on the knowledge that fluoride binding occurs with a molecule of HF, rather than F^-

Reproduced with permission of the copyright owner. Further reproduction prohibited without permission.

(92,93). Since Cl^- is not protonated at pH 7, there is poor conversion to the 6-c form. Alternatively, a high concentration of NaCl may induce conformational changes of the polypeptide that are transmitted to the heme pocket and what we observe is just the result of a rearrangement of the water molecules that perturbs the appearance of the EPR (and the optical) spectra. In fact, Raman spectra of samples under similar conditions didn't show a net increase of the band associated with a typical 6-c HS heme; on the contrary, a broad ν_3 band centered at 1495 cm^{-1} and an increase of the intensity of the ν_3 band at 1487 cm^{-1} was observed, consistent with some changes in spin state and coordination number but only incomplete conversion of the starting enzyme to a new form.

If both fluoride and chloride in fact are bound to heme iron, one significant difference between the two may be related to the greater tendency for fluoride to form hydrogen bonds compared to chloride. The optical spectra of fluoride-bound heme complexes in peroxidases show trends in the frequency of the CT1 band that correlate with the behavior of the distal hydrogen bonding ligands such as tryptophan indole and histidyl imidazole nitrogens. These interactions contribute to the stability of the 6-c complexes and the strength and number of hydrogen bonds to the bound ligand influences the energy of the optical transitions including the CT1 bands through electronic induction effects (94).

In a second analysis, an excess of NaCl was added to samples of enzyme that had been stored in phosphate buffer for some time. As described above, the heme iron in the enzyme under these conditions is almost completely hexacoordinate. Figure 4.6 (panel A) shows the EPR spectrum of a sample of KatG (at pH 7) that had been stored for one week in buffer alone (a), compared to the same enzyme immediately after the addition of excess

Reproduced with permission of the copyright owner. Further reproduction prohibited without permission.

NaCl (b), and twenty four hours after the addition of excess NaCl (c). Here, a nearly axial signal ($g_{\perp}$ = 5.8; $g_{\parallel}$ ~ 2) (r_2) typical of a 6-c HS heme species is found, similar to that observed for the fluoride addition to the fresh enzyme. These results suggest that the initially present 6-c form of the aged enzyme allows the replacement of the water molecule that constitutes the sixth ligand to the heme iron with a chloride ion. This may be evidence that fluoride is able to bind to 5-c heme iron but chloride binding is complete only through a ligand displacement reaction. This difference between the two binding mechanisms may be attributed either to the difference in size of the two ligands or to the charge of the binding species (HF or Cl^-).

In a third analysis the effect of NaCl addition to the enzyme was monitored at low pH. The same EPR samples described above were prepared in citrate buffer at pH 5 (Figure 4.6, panel B). A nearly axial signal (r_2) with a small component of the r_1 signal is found for the pure KatG enzyme stored for one week and exchanged into pH 5 buffer (spectrum (a)); the addition of NaCl to the enzyme at pH 5 shows a conversion of the 6-c HS species (r_2) to the atypical 6-c signal (r_4) that is complete in spectrum (c) recorded twenty four hours after the addition of NaCl. This EPR spectrum strongly resembles the EPR spectra reported elsewhere for 6-c QS heme forms of peroxidase (86).

If this is, in fact, an example of QS heme, the optical spectrum should be different from typical 6-c HS. Spectrum (a) in Figure 4.7 characterized by a Soret peak at 407 nm and a CT1 band at 628 nm confirms that the stored enzyme at pH 5 before the addition of NaCl contains 6-c HS heme; after the addition of excess NaCl (spectrum (b)) there is a red-shift of both Soret (411 nm) and CT1 bands (634 nm) accompanied by a sharpening of the Soret peak. The guidelines previously reported for the optical identification of a QS

Reproduced with permission of the copyright owner. Further reproduction prohibited without permission.

spin state suggest the assignment of the spectrum obtained after the chloride addition at pH 5 to a 6-c QS spin state. Therefore, the results suggests that only under these specific conditions, a 6-c QS heme species can be isolated and identified for the first time in the *M. tuberculosis* KatG.

Assuming that the above sample represents QS heme, the relative contribution of the 3/2 and 5/2 states to the QS admixture can be approximately determined, according to Maltempo's calculation, from the g_{ave} value of the EPR signal r_4. This analysis for the r_4 signal predicts that the intermediate spin (S = 3/2) contributes approximately 10% to the QS spin state (Appendix B) (89). Therefore, the quantum mechanical admixture in KatG is almost completely HS.

The presence of a 6-c QS species is consistent with assignment of the atypical ν_3 band at 1487 cm^{-1} observed in many Raman spectra (included the fresh and aged enzyme) to a 6-c QS species rather than 6-c HS. Also, the presence of 6-c QS heme is consistent with the presence of 5-c QS heme (as evidenced by Raman) according to Indiani et al. (86), who suggested that the heme deformation responsible for the 5-c QS state are maintained when heme is converted to the 6-c QS form.

The initial reason that led us to a detailed analysis of the low temperature EPR spectra of the KatG enzyme in the presence of chloride was the possibility that in KatG there is a contribution from a chloride complex even though we routinely exchanged the enzyme after each chromatographic step in potassium phosphate. Despite that fact that this study gave us valuable information about the enzyme it didn't allow us to definitively answer this question with reasonable confidence. In fact, the purification of the enzyme (fresh partially purified compared to fresh fully purified Figure 4.1 spectra (a) and (b)

Reproduced with permission of the copyright owner. Further reproduction prohibited without permission.

respectively) is accompanied by the appearance of 6-coordinate species whose formation, as it was discussed above, can be induced by either storage or chloride binding.

4.4 Antibiotic (INH) binding to ferric KatG

An important goal of these spectroscopic studies is to understand changes in coordination and spin states such that changes in heme structure induced by drug binding to KatG can be interpreted. An analysis was undertaken for KatG samples in the presence of the drug. It was already thought based on optical spectroscopy that the coordination at the KatG heme shifts toward 5-c in the presence of INH (31,32).

Figure 4.8 shows the EPR spectra of KatG (sample frozen after the enzyme was stored for three weeks at 4 ° C) (a) and the same enzyme after the addition of INH (b). An increase of the r_4 (6-c QS) signal is observed, while the r_2 6-c HS signal is probably lower in intensity. Similar results were obtained after addition of benzohydroxamic acid (BHA, this molecule is structurally similar to INH and has a similar binding affinity for KatG) to the enzyme (Figure 4.9 (a) and (b)).

Optical and Raman data show that upon INH binding, conversion from 6-c to 5-c HS and 5-c QS heme occurs. The apparent discrepancy with the EPR data, which show the conversion of the enzyme to a species assigned above to a 6-c QS heme may find justification in frequently observed freezing artifacts in heme proteins (91). Moreover, interchange between 6-c QS heme and 5-c QS heme is reasonable, since, as stated above, the heme distortion thought to be required for stabilization of the mixed spin state is not removed upon conversion to a 6-c form, at least in Class III peroxidases (86). Therefore, the change in coordination is probably induced by small displacements of the sixth ligand to the heme iron (water molecule) that take place upon freezing.

Reproduced with permission of the copyright owner. Further reproduction prohibited without permission.

The data obtained from the spectroscopic analysis of *M. tuberculosis* KatG were then analyzed in light of the recently published crystal structures of KatG from *H. marismortui* and *B. pseudomallei*. The crystal structure of KatG from *B. pseudomallei* KatG reports the presence of a potential INH binding site located close to the heme propionate groups (Figure 4.10). It is possible to suggest that at room temperature, INH binding induces a specific distortion of the heme macrocycle that stabilizes the QS spin state and forces the Fe to release the sixth ligand (water molecule). Previous optical studies have already shown that INH addition induces changes in the distal heme pocket including loss of coordinated water (31). A detailed Raman analysis reported elsewhere suggests that the conformational form associated with the QS spin state probably depends on a network of water molecules and certain amino acids located in the distal heme pocket that are involved in a complex network of hydrogen bonds that includes the heme propionate group(s) (Figure 4.2) (87). Moreover, Ser315 (Ser 324 in *B. pseudomallei*), according to the region illustrated in Figure 4.10, is hydrogen bonded to a heme propionate group and to INH. Therefore, this residue may be directly responsible for communicating between the drug binding site and the heme. More information relevant to this issue was provided by results for KatG[S315T].

The analysis of the available data shows that the binding of INH to the *M. tuberculosis* KatG enzyme induces a conversion from the 6-c HS species to the 5-c QS heme spin state which, upon freezing, becomes 6-c QS.

4.5 KatG[S315T] mutant

In the previous section, EPR together with resonance Raman and optical results for the wild type KatG enzyme provided information about heme coordination numbers

Reproduced with permission of the copyright owner. Further reproduction prohibited without permission.

and spin states. An EPR analysis was also undertaken for the most common KatG drug resistant mutant enzyme, KatG[S315T]. Interesting differences were immediately observed.

Figure 4.11 shows the low temperature EPR spectrum of a sample of KatG[S315T] enzyme recorded on a sample frozen after three weeks' storage (spectrum 4.11 (a)). The EPR spectrum shown here closely resembles the spectrum of fresh fully purified WT KatG presented in the previous section (spectrum 4.1 (b)) where signals r_1, r_2 and r_4 are simultaneously present. Therefore, this mutant enzyme, despite the storage period, still contains 5-c HS heme species in high abundance. Raman data collected for the fresh and stored KatG[S315T] mutant confirmed that the mutant enzyme is significantly more stable to conversion to the 6-c form than the WT enzyme.

According to the recently published crystal structures the hydroxyl group of residue S315 (Ser 324 in *B. pseudomallei*) is hydrogen bonded to a heme propionate group and it is part of that network of water molecules in the distal side of the heme mentioned above. Raman spectra of WT KatG and the KatG[S315T] mutant suggest that the substitution of Ser315 with a bulkier threonine probably disrupts the network of hydrogen bonding at the distal side of the heme and destabilizes the water ligand to the heme iron, favoring the 5-coordinate form (87).

These observations show that alterations in the region of Ser315, whether induced by mutation or drug binding, induce changes in heme conformation.

4.6 Low spin heme in ferric KatG

The two major conclusions from the following paragraph demonstrate that: 1) little to no LS heme species are present in the KatG enzyme under a variety of conditions; and,

Reproduced with permission of the copyright owner. Further reproduction prohibited without permission.

2) the pK_a of water coordinated to the sixth position of the heme iron is very high (higher than 10) probably because it is not tightly bound to the iron.

The analysis demonstrating the very low abundance of low spin forms in *M. tuberculosis* KatG enzyme turned out to be decisive in the identification of the QS heme spin state suggested above. In fact, based on the very low abundance of LS heme detected by EPR and optical spectroscopy, the Raman vibration at 1503 cm^{-1}, whose assignment was initially uncertain, was assigned to 5-c QS heme with greater confidence.

In CCP, which we have used as an example of a Class I peroxidase with high homology to KatG, the pentacoordinate high spin heme characteristic of the freshly prepared enzyme is easily converted to a hexacoordinate LS form upon freezing and other manipulations (91). In the *M. tuberculosis* KatG enzyme, a power and temperature dependence of EPR signals of the samples described in the previous sections of this chapter was conducted to maximize the intensity of low spin forms possibly present to check for similar behavior (LS signals saturate much easier than HS). Since no strong field external ligand was added during the preparation of the EPR samples (typical examples of these include azide, cyanide, mercaptide), the two most likely low spin forms that we expected to find were a bisimidazole or a hydroxide form. Bisimidazole species can be found in peroxidases since a distal histidine imidazole is available for heme iron binding at the sixth position. Small conformational changes from the native structures of these proteins can induce coordination of this ligand, forming a stable 6-c LS complex with characteristic rhombic EPR spectra (95). The formation of the LS hydroxide species usually occurs upon titration of 6-c aquo forms of the enzymes to high pH, above the pK_a

Reproduced with permission of the copyright owner. Further reproduction prohibited without permission.

of the axially bound water molecule in the sixth position. The pK_a for this water molecule is usually around 8 in globins, and is closer to 10 in peroxidases.

EPR analysis showed that not more than 10% of the total heme in the samples of purified KatG is present as a LS form. This LS species was found after storage for ten weeks at pH 7 of a sample of pure KatG. Quantification was based on the intensity of a feature at g = 2.2 considered to represent the g_{mid} for a low spin heme species. A second sample that showed the presence of LS heme is a sample of fresh, fully purified KatG exchanged into pH 10 buffer. This sample was prepared to investigate the pK_a of water coordinated in 6-c forms already present in the sample. A signal having g-values equal to $g_x = 2.64$; $g_y = 2.20$; $g_z = 1.85$ was evident under these conditions. This LS heme species was identified according to the Peisach and Blumberg classification (80) as the hydroxide species. The abundance of the low spin form in this sample was estimated to be approximately 10% using myoglobin β-mercaptoethanol as standard (96). LS species were not detected in other samples of KatG. This result confirms some earlier observations that there was no change in the optical or Raman spectrum of KatG at pH 10 compared to pH 7. Titration to even higher pH denatures some enzyme so we could not evaluate the pK_a of axially bound water. The high pK_a could be consistent with a weakly bound water molecule.

For the purpose of additional confirmation related to LS species, a bisimidazole 6-c LS complex of KatG was deliberately prepared by adding an excess of solid imidazole to a sample of KatG. The EPR spectra showed three low spin complexes. One was the hydroxide form. Neither of the other two (g_{max} = 3.2 and 2.9) were found in EPR spectra of the enzyme without addition of imidazole. The g values for bisimidazole forms of ferric

Reproduced with permission of the copyright owner. Further reproduction prohibited without permission.

heme complexes are known to depend on the relative orientation of the imidazole planes above and below the porphyrin plane (97). The formation of multiple bisimidazole forms in an enzyme such as KatG, which is a dimer of identical subunits, suggests that there is some inherent heterogeneity in the enzyme that we suggest is related to the presence of the distal side amino acid adduct in less than 100% of the protein (74). Additional heterogeneity in these species could be a result of pH dependent conformational states.

Rusnak et al.,previously reported EPR spectra of *M. tuberculosis* KatG that showed signals of significant intensity attributed to a low spin (LS) heme component (84). They estimated this population (assigned to bis-imidazole species) to be around 30-50% of the heme iron depending on whether the enzyme was the wild type or the mutant KatG[S315T]. The discrepancy with the results presented in this thesis may be ascribed to different techniques of enzyme purification that altered the native state of the enzyme.

4.7 Conclusions

In this chapter, evidence has been presented that *M. tuberculosis* KatG is characterized by heterogeneity of coordination number and spin states. There are many potential sources of heterogeneity including incomplete adduct formation, mixed protonation state of the distal imidazole, anion ligand binding and water binding. It has also been shown that a 6-c QS heme spin state is always present in *M. tuberculosis* KatG. It appears as the majority species upon addition of chloride ion at low pH. A 5-c QS heme species detected in *M. tuberculosis* KatG at room temperature is instead probably converted to the 6-c QS form upon freezing. INH binding affects the conformation of the heme through a network of hydrogen bonded water molecules and amino acids located at

Reproduced with permission of the copyright owner. Further reproduction prohibited without permission.

the distal side of the heme. The region around Ser 315 also affects the heme structure on the distal side through hydrogen bonding effects.

The research work presented in this chapter has already been published in (32,87).

Reproduced with permission of the copyright owner. Further reproduction prohibited without permission.

Chapter 5

5.1 Concluding remarks

The ultimate goal of the scientific community involved in the study of tuberculosis is to discover new, more effective drugs that can defeat the disease. The call for new antibiotics is required by the recent development of INH and more critically multi-drug resistant strains (MDR). The mechanism of INH action is still under investigation, but an important milestone has been the discovery that this antibiotic requires *in vivo* activation by catalase peroxidase, KatG. Unfortunately, little was known about this enzyme before its role in the mechanism of isoniazid activation was discovered. Therefore, the most critical goal is now to gain more insight into KatG structure and function as a first step to reach a complete understanding of its interaction with isoniazid and the mechanisms of drug resistance.

The research work in this thesis used EPR spectroscopy as the main tool because it provides insights into both the structure and function of KatG. In particular, specific attention was paid to the catalytic activity of KatG (Chapters 2 and 3), and to the changes in structure induced by different factors such as drug binding (Chapter 4).

One of the most important accomplishments of this work is the discovery of a tyrosyl radical formed in *M. tuberculosis* KatG when it is reacted with alkyl peroxides (Chapter 2). Evidence for formation of this radical on tyrosine Tyr353, which is not conserved among other KatG enzymes was also found (Chapter 3). The study of the kinetics of tyrosyl radical formation showed that a relationship exists between this species and the intermediates previously identified in the catalytic cycle of KatG: the tyrosyl radical is probably formed from Compound I (Chapter 2). In mutant KatG[Y229F], it has

Reproduced with permission of the copyright owner. Further reproduction prohibited without permission.

been specifically shown that electron transfer from tyrosine to Cmpd I leads to the simultaneous formation of tyrosyl radical and Cmpd II (Chapter 3).

The potential importance of the studies addressing tyrosyl radical formation in KatG is that this radical, in addition to a potential catalytic function in metabolic reactions *in vivo*, may also play a specific role in the mechanism of drug activation. Radical mechanisms have been proposed for formation of the INH-NADH adduct required in the mechanism of drug action. The tyrosyl radical may be necessary, together with Cmpd I, for production of this adduct since both can perform single electron oxidations or hydrogen atom abstractions to initiate adduct formation. Some suggestions presented in this thesis may argue in favor of a catalytic function for the radical such as: 1) the radical is formed on a tyrosine (Y353) unique to the *M. tuberculosis* enzyme; 2) the tyrosyl radical reacts with INH (28); and 3) non specific pathways for radical formation occur if the key tyrosine is taken away either by mutation or by self-inactivation (Chapter 3).

To extend the understanding of the tyrosyl radical function, different mutant enzymes should probably be studied; for instance, a mutant replacing the key tyrosine 353, with a tryptophan, the amino acid most frequently found in the corresponding position of homologous KatGs, would give a better understanding of the specificity of radical production at this site in *M. tuberculosis* KatG. Moreover, mutation of Trp107 and Met255 (or both in a double mutant) which, with Tyr 229, are likely to form an adduct on the distal heme side, may shed more light on confirming the role of the adduct in preserving the catalase activity of KatG.

Expanding the EPR studies demonstrating evolution of the tyrosyl radical from doublet to singlet species that includes a theoretical model describing the dependence of

Reproduced with permission of the copyright owner. Further reproduction prohibited without permission.

the g_{11} values on the rotational angle θ, will help in identifying which of the hypotheses presented in Chapter 2 better explains the radical behavior. Another interesting topic that may be further analyzed is the change in structure of the WT enzyme pre-treated with a large excess of PAA; this should be performed through physical characterization of the product of this reaction to check for oligomerization of the polypeptide through tyrosine cross links formed from tyrosyl radical recombination. The results would provide confirmation about the site of radical formation.

The major achievement in the second part of this work (Chapter 4) is the definition of heterogeneity of KatG heme iron spin states and coordination numbers that is determined by multiple factors such as water and other ligand binding, protonation state of the distal imidazole, and probably incomplete adduct formation. Furthermore, it has been shown that in KatG, the coordination of the ferric iron and the geometry of the active site are influenced by small molecules such as isoniazid that do not directly bind to the heme iron, but at a special binding site removed from the heme.

Some discrepancies attributed to temperature differences and freezing artifacts were observed in the distribution of the spin state populations recorded for similar samples by optical, Raman (room temperature) and EPR (77 K) spectroscopy. Spectra collected for the same samples using low temperature optical and Raman apparatus will be necessary to support these hypotheses. Moreover, it would be useful to study spin state and coordination number changes in mutant enzymes KatG[W107F], KatG[Met255F] and KatG[H108F] under different conditions of pH, ligand binding, etc. The comparison of these studies with the one presented here for the WT enzyme will provide important information about the effect that the adduct has on the observed heterogeneity.

Reproduced with permission of the copyright owner. Further reproduction prohibited without permission.

Another important accomplishment of this work is the correlation established in *M. tuberculosis* KatG between heme iron spin state, and INH binding. An increase in intensity of EPR and Raman features associated with an unusual spin state (QS) probably induced by a specific heme distortion has been observed upon INH addition to the enzyme. Therefore, our analysis strongly suggests that INH, which binds at the heme periphery, induces a rearrangement of the heme pocket on the distal side with a resulting change in spin state.

Even though the correlation between INH binding at a specific site in the protein and the QS heme spin state has been established, it is extremely difficult to explain why the binding induces a heme structure associated with the QS spin state. This difficulty is partially due to the fact that the origin of the QS spin state is still unresolved and structural information is lacking for the *M. tuberculosis* KatG heme group.

A better understanding of the correlation between QS spin state and INH binding will hopefully find a clear answer when the crystal structures of the *M. tuberculosis* KatG enzyme in the presence and absence of INH is solved. Moreover, the crystal structure of the INH resistant mutant enzymes will provide explanations for the origin of drug resistance and may lead to the development of new anti-tuberculosis antibiotics.

Reproduced with permission of the copyright owner. Further reproduction prohibited without permission.

Appendix A

Materials and Methods

Materials-Escherichia coli UM262 (contains pKAT II, overexpression system containing the *M. tuberculosis* katG gene) was a gift from Stewart Cole (Institut Pasteur, Paris, France). L-3,3-[$^2H_2$]tyrosine and L-2,4,5,6,7-[$^2H_5$]tryptophan were from Cambridge Isotope Laboratories, Inc. (Cambridge, MA); LB (Luria-Bertani) Broth, Miller medium was purchased from Fisher Biotech. All other reagents were from Sigma-Aldrich. Isoniazid was recrystallized from methanol.

M. tuberculosis KatG preparation—*M. tuberculosis* KatG was prepared from *E. coli* strain UM262 (*katG* minus) carrying an overexpression plasmid (pKAT II) containing the *M. tuberculosis katG* gene. Bacteria were grown in LB growth medium (25 g/L of purified H_2O) plus ampicillin (100 μg/ml) at 37 °C in 0.5 or 1 L flasks with constant shaking. Protein expression was induced by the addition of 3-β-indoleacrylic acid (40 mg/L) when the optical density (600 nm) of cultures reached ~0.9-1. δ-aminolevulinic acid-HCl (16.8 mg/L) a heme biosynthesis precursor, was added to cultures to maximize the yield of holoenzyme because protein synthesis outruns heme synthesis without this precursor. Cells were harvested 6-18 hours post induction.

The enzyme was purified at 4 °C by FPLC according to a published procedure with minor modification (98) using 20 mM potassium phosphate buffer, pH 7.2. Purity was based on the optical purity ratio (A_{405}/A_{280}), which was approximately 0.54 for all the enzyme used in these studies. Spectrophotometric measurements were made using a

Reproduced with permission of the copyright owner. Further reproduction prohibited without permission.

Model NT14 UV-Vis spectrophotometer (Aviv Associates, Lakewood, NJ) interfaced to a personal computer.

Deuterium labeled KatG preparation— E. coli strain UM262 could not be grown in minimal medium because of amino acid auxotrophy. Therefore, *E. coli* BL21 was selected as a host for the pKAT II vector in order to produce labeled enzyme by labeled amino acid supplementation. BL21 was transformed by electroporation. While strain UM262 does not express *E .coli* KatG (HP I), strain BL21 expresses catalase-peroxidase; therefore, the level of *E. coli* KatG was checked by SDS-PAGE electrophoresis of crude extracts from *E .coli* BL21 strain grown for 6 hours in M9 medium. No KatG was detected. Therefore, it was assumed that contamination of the preparation of overexpressed deuterium-labeled *M. tuberculosis* KatG with *E. coli* HP I was negligible.

Labeled KatG was prepared using the same overexpression plasmid used for unlabeled KatG (pKatII), but in *E. coli* strain BL21 (see below). Bacteria were grown in M9 (minimal) medium supplemented with $MgSO_4 \cdot 7H_2O$ (0.5 g/L), $CaCl_2 \cdot 2H_2O$ (11mg/L), $ZnCl_2$ (0.5 mg/L), $MnSO_4 \cdot H_2O$ (0.1 mg/L), $FeCl_2 \cdot 4H_2O$ (10 mg/L), glucose (3.60 g/L), ampicillin (100 mg/ml) prepared under sterile conditions. Either sterile L-2,4,5,6,7-[$^2H_5$]tryptophan (39 mg/L) or L-3,3-[$^2H_2$]tyrosine (47.6 mg/L) were added to the medium to produce labeled KatG.

Protein expression was induced by the addition of 3-β-indoleacrylic acid (40 mg/L) when the optical density ($A_{600\ nm}$) of cultures reached ~0.9-1. δ-aminolevulinic acid-HCl (16.8 mg/L) was added to culture to maximize the yield of holoenzyme as described for unlabeled KatG. The cells were harvested 16 hours after induction and the protein was

Reproduced with permission of the copyright owner. Further reproduction prohibited without permission.

purified by FPLC according to published procedures (98). The optical purity ratio of the labeled enzymes was approximately 0.53.

Catalase activity—One unit of catalase activity is defined as the amount of enzyme catalyzing the decomposition of 1 μmol of H_2O_2/min at 25 °C. The catalase activity was assayed in phosphate buffer, pH 7.5, using approximately 25 mM H_2O_2 (ε_{240nm} = 43.6 M^{-1} cm^{-1}) by following the decrease in absorbance at 240 nm typically from 0.8 to 0.65 (99).

Peroxidase activity—One unit of peroxidase activity is defined as the amount of enzyme that catalyzes the oxidation of 1 μmol of *o*-dianisidine/min. Peroxidase activity was measured spectrophotometrically in 50 mM sodium acetate buffer, pH 5.5, using *tert*-butyl hydroperoxide (23 mM) and *o*-dianisidine (0.1 mM), following color development at 460 nm (ε_{460nm} nm = 11.3 mM^{-1} cm^{-1} for the oxidation product) (98).

Protein concentration—The concentration of KatG was determined using the Bio-Rad protein assay reagent (Bradford method) or using the heme extinction coefficient, $\varepsilon_{407\,nm}$ = 100 mM^{-1} cm^{-1}.

Electrophoresis—Gel electrophoresis was carried out under denaturing (SDS-PAGE) and nondenaturing (Native-PAGE) conditions using a Pharmacia Biotech PhastGel system.

Optical Stopped-Flow Spectrophotometry—Kinetic measurements were performed using a HiTech Scientific Model SF-61DX2 stopped-flow apparatus equipped with a rapid-scanning diode-array spectrophotometer. Kinet-Asyst software was used for data acquisition and analysis.

Reproduced with permission of the copyright owner. Further reproduction prohibited without permission.

RFQ-EPR Spectroscopy—Rapid freeze-quench EPR samples were prepared using an Update Instrument, Inc. Model 1000 chemical-freeze-quench apparatus (Figure A.1). KatG (typically 100 uM) and peroxyacetic acid (3-fold excess over heme concentration) in 20 mM potassium phosphate buffer, pH = 7.2, were mixed and reacted for the indicated time periods followed by freeze-quenching of reaction mixtures in isopentane at -130 °C. Frozen sample powders were packed into precision-bore quartz EPR tubes immersed in the isopentane bath and were then transferred to liquid nitrogen and finally were examined using a Varian E-12 or a Bruker E500 EPR spectrometer operating at X-band. A finger Dewar inserted into the EPR cavity was used for recording spectra at liquid nitrogen (77 K) temperature, while a liquid helium cryostat and Heli-Tran liquid helium transfer system (Advanced Research System, Inc., Allentown, PA) or an Oxford liquid helium transfer system and cryostat were used for EPR at temperatures between 5 and 30 K. EPR data acquisition and manipulation was made using WinEPR software (11) or WinEPR software (Bruker).

Quantitative EPR—The EPR spectrum of 0.5 mM Cu(II)EDTA in 50% ethylene glycol was used as a spin standard. Quantification was accomplished by double integration of EPR signal intensities. The signal-to-noise ratio in EPR spectra was improved by signal averaging when necessary. The estimation of spin concentration in freeze-quench samples included application of a packing factor of 0.5 to account for dilution by isopentane. Intensity estimation for the EPR signal of resting (Fe(III)) enzyme (Chapter 2) was performed by measurement of the peak height taken at g = 6 relative to a maximum (100%) signal height for the known concentration of resting enzyme before reaction with peroxide, again taking into account a packing factor of 0.5.

Reproduced with permission of the copyright owner. Further reproduction prohibited without permission.

Site-Directed Mutagenesis of the M. tuberculosis katG gene—All KatG mutant enzymes used in the present research were prepared by Dr. Shengwei Yu. Mutagenesis was performed using the Transformer site-directed mutagenesis kit from Clontech (Palo Alto, CA) according to published procedures (33,75,100). Correct nucleotide replacement was confirmed by sequencing of double-stranded plasmid DNA by the Sanger method (101) (Gene Link, Inc.; Hawthorne, NY).

Reproduced with permission of the copyright owner. Further reproduction prohibited without permission.

Appendix B

This Appendix presents an overview of EPR spectroscopy applied to biological systems and specifically addresses issues relevant to the work in this thesis.

B.1 Resonance phenomenon

Electron paramagnetic resonance spectroscopy (EPR) is a technique that provides structural information about atoms and molecules containing unpaired electrons, and is sensitive to the magnetic moment μ produced by the unpaired electron(s) and the local magnetic field produced by neighboring atoms. The paramagnetic systems described in this thesis were either organic radicals or ferric iron. Quantitative EPR, which was used in the study of radical formation here, provides the measurement of the concentration of unpaired spins present in the sample, by comparison to a primary spin standard.

EPR basically is sensitive to the magnetic moment μ of the unpaired electron and its interaction with local electric and magnetic fields produced within and nearby the parent atom. The magnetic moment μ is indirectly measured through the dimensionless parameter, g.

In the absence of a magnetic field, the two spin orientations of an unpaired electron are energetically degenerate. In the presence of an external magnetic field, the component of **s** in the direction of the magnetic field is quantized and can have two values, $m_s = \pm 1/2$. The magnetic energy is proportional to the magnetic moment, which is proportional to the spin angular momentum:

$E_m = -\mu_z (m_s) B_0 = g \mu_B B_0 m_s$ μ_B, Bohr magneton = $e \hbar / 2 m_e$

The energy levels are therefore separated by:

$\Delta E = g \mu_B B_0 = \gamma \hbar B_0$ $\Delta m_s = \pm 1$

Reproduced with permission of the copyright owner. Further reproduction prohibited without permission.

where γ, called the magnetogyric ratio, is defined as $\gamma = gq/2m_e$; g is the Zeeman factor. Transition between the Zeeman-split levels may be induced by photons of appropriate energy (Figure B.1):

$\Delta E = h\nu = g\,\mu_B\,B_0$

These two expressions define the resonance condition for the observation of an EPR signal, which is usually obtained experimentally in an instrument operating at a constant frequency and variable magnetic field.

B.2 g-factor anisotropy

The g value for a free electron is 2.002329 (57). For electrons bound in atoms or molecules, the resonance condition changes due to effects of the environment. The predominant effect that determines the value of g in atoms and molecules is the spin-orbit coupling. The g-factor is orientation dependent in a system with symmetry lower than spherical, which is an anisotropic system; g depends on the angle between the external magnetic field **B** and the local symmetry axis system of the paramagnetic center. Taking into account the dependence of g on angles that define the orientation of **B** relative to the principal axis system of the g-tensor (θ and φ), the Zeeman energy can be written using a spin Hamiltonian:

$H_{Ze} = \mu_B\,\mathbf{B}\cdot\mathbf{g}\cdot\mathbf{S}$

where **g** is now defined as a tensor and it reflects the symmetry of the paramagnetic center under study; six independent parameters are needed to determine the magnitude and orientation of the g-tensor axes within a molecular axis system. The deviation of its principal values from the g of the free electron is due to the admixture of orbital angular

Reproduced with permission of the copyright owner. Further reproduction prohibited without permission.

momentum with electron spin angular momentum. Therefore, shifts in the g values can be attributed to the differences in size and shape of the local electric, and sometimes magnetic, fields that are present at the unpaired electron. These electric and magnetic fields are created by ligand atoms, parent or satellite nuclei as well as satellite unpaired electrons.

In liquid samples, the anisotropy is time-averaged because of the rapid tumbling of the molecules and therefore the resulting spectrum is isotropic with narrow linewidths possible. In solids, the anisotropy is space-averaged, giving a powder pattern spectrum, which extends over the field range determined by the minimum and maximum values of the g-tensor components. Frozen solutions also give powder pattern spectra.

B.3 Spin-Hamiltonian

For electrons bound in atomic or molecular orbitals, the electrostatic and magnetic interactions between the electron and its environment can be found in hyperfine coupling interactions that alter the energy levels of the unpaired electron system. The strength of these interactions may often be obtained directly from spectral data.

All the interactions that may split or shift the electron spin energy levels and thus affect the EPR spectrum can be written into a spin Hamiltonian for the system of interest. The full Hamiltonian operator that describes the energy of a radical or atom with unpaired electrons and includes nuclei with non-zero spins can be written as:

$$H = H_N + H_{el} + H_{CF} + H_{LS} + H_{SS} + H_{Ze} + H_{hfi} + H_{Zn} + H_{II} + H_Q$$

where the first two terms describe the kinetic and potential energy of the nuclei and electrons. H_{CF} describes the crystal field splitting, H_{LS} the possible spin-orbit coupling contributions. H_{SS} is the term for electron spin-spin interaction. H_{Ze} and H_{Zn} stand for

Reproduced with permission of the copyright owner. Further reproduction prohibited without permission.

electronic and nuclear Zeeman splittings in an external magnetic field. H_{hfi} describes the electron-nuclear hyperfine interaction, which can be isotropic or anisotropic, and the last two terms which describe nuclear spin-spin and nuclear quadrupole interactions are usually not very relevant in CW-EPR spectroscopy. The most important terms of the spin Hamiltonian for practical EPR spectroscopy are those that reflect the interactions of the unpaired electrons and nearby nuclei with an applied magnetic field and with each other. Therefore, the effective spin Hamiltonian contains only a few selected interactions, chosen beforehand and depending on the problem under consideration. For example, for an organic radical such as the tyrosyl radical reported in Chapters 2 and 3, the spin Hamiltonian will contain the terms for electronic Zeeman interaction and the electron-nuclear hyperfine coupling interaction.

The following paragraphs will give only a brief overview of the terms for most important types of interactions; more detailed descriptions will be given only for those topics considered of particular interest for the understanding of the present thesis.

B.3.1 Zeeman interactions

The interaction of an electron or a nucleus with an external static magnetic field taken along some direction **z** is described by:

$H_e = + g\beta_e B S_z$

$H_n = - g_n\beta_n B \hat{I}_z$

B.3.2 Hyperfine interactions

This is defined as the interaction of an unpaired electron with neighboring magnetic nuclear dipole moments. The hyperfine interaction may be either isotropic (orientation independent) or anisotropic (dependent on the orientation of the external field

Reproduced with permission of the copyright owner. Further reproduction prohibited without permission.

with respect to a molecular axis). An anisotropic hyperfine interaction can be accompanied by a significant isotropic component, and they are both measurable (57).

B.3.2.1 Isotropic Hyperfine interaction

The spin Hamiltonian operator for one electron interacting with nuclei, including also the electron and nuclear Zeeman interactions, is:

$H = g\beta_e B S_z - \sum_i g_{ni}\beta_n B \hat{I}_{iz} + \sum_I A_{0i} S z \hat{I}_{iz}$

A_{0i} is the isotropic hyperfine coupling constant and it measures the magnetic interaction energy between the electron and each nucleus.

The effect of the nuclear Zeeman energy (second term) is not normally seen in EPR because the contributions from this term cancel in the upper and lower electron spin manifolds. The most general matrix form for the isotropic electron-nuclear coupling interaction is:

$H_{iso} = A_0 \mathbf{S}^T \cdot \hat{\mathbf{I}}$

The isotropic component of the electron-nuclear hyperfine interaction is observed even in powder pattern EPR spectra and is also called the Fermi contact interaction. It arises from the delocalization of electron spin density onto an s-orbital of a nearby atom having non-zero nuclear magnetic moment. In an organic π-radical, for example, an unpaired electron in a p-π orbital may experience a hyperfine interaction with σ-bonded hydrogen atoms through a σ-π-spin polarization mechanism. An example of this kind of isotropic interaction can be observed in a tyrosyl radical where the unpaired electron delocalized in the phenol ring shows hyperfine coupling interaction with hydrogens at the 3' and 5' positions of the ring. The same kind of Fermi contact interaction is also observed between

Reproduced with permission of the copyright owner. Further reproduction prohibited without permission.

an unpaired d-electron and the magnetic nucleus of a transition metal such as Cu(II) and Co(II) ions, for which M_I is 3/2 and 7/2 respectively.

B.3.2.2 Anisotropic Hyperfine interaction

The spin Hamiltonian containing the electron Zeeman term, and also the isotropic and anisotropic electron nuclear hyperfine interactions is given by:

$$H = g\beta_e \mathbf{B}^T \cdot \mathbf{S} + \mathbf{S}^T \cdot \mathbf{A} \cdot \hat{\mathbf{I}} - g_n \beta_n \mathbf{B}^T \hat{\mathbf{I}}$$

The anisotropic hyperfine interaction is the classical magnetic dipolar interaction between an electron and a nuclear dipole. It is observed only in solids (powders, frozen solutions) as molecular tumbling in solution would make this interaction unobservable. The weak couplings due to this term are usually not resolvable in CW-EPR spectra of organic radicals but can be evaluated in double resonance techniques such as ENDOR.

B.3.3 Spin-spin- and electron-exchange interactions

Electron systems with multiple unpaired spins give rise to another terms, which for two interacting electrons can be written as:

$$H = g\beta_e \mathbf{B}^T \cdot \mathbf{S} + \mathbf{S}^T \cdot \mathbf{D} \cdot \mathbf{S} - \tfrac{1}{2} J_{n0}[\mathbf{S}^2 - 3/2\mathbf{1}_3]$$

The first term is the electron Zeeman interaction. The second term is the spin-spin interaction, or the anisotropic magnetic dipole-dipole interaction between the two unpaired electrons. The last term is the isotropic component of the exchange interaction derived from the electric interaction of the two unpaired electrons (J_0 is defined as the isotropic electron-exchange coupling constant); this last interaction splits apart in energy the singlet and triplet states that constitute the four spin state system for two interacting electrons. The electron-electron interactions in the S = 5/2 system of high-spin Fe(III)

Reproduced with permission of the copyright owner. Further reproduction prohibited without permission.

give rise to the unique EPR spectra of heme proteins and enzymes considered in this thesis.

B.4 EPR of Metalloproteins

The g-factor can have as many as three values, each one corresponding to a resonance position at which the external magnetic field H lies parallel to one of the three principal directions of the g tensor. These special directions often coincide with the structural (and for metal ions, the crystal field) axes of the molecule. The projections of g along these three directions are usually labeled g_x, g_y, and g_z when the g-tensor assignment in the molecular axis system has been made. Otherwise the three g values are non-specifically defined as g_1, g_2 and g_3.

Three different cases can be observed and they are illustrated in Figure B.2 (102):

1. The isotropic case: all the three g values are equal in magnitude; therefore only a single EPR absorption curve is observed (Figure B.2 (a)).
2. The axial case in which one g-value ($g_{\parallel}$) is different from the others ($g_{\perp}$). $g_{\parallel}$ can be either larger or smaller than $g_{\perp}$ (Figure B.2 (b), (c)).
3. The rhombic case in which all three g values are different (Figure B.2 (d)).

These three cases correspond to four different sets of conditions:

a. $S = ½$, $\Delta g < 0.4$ (for example Cu(II), Ni(III), low-spin Co(II), Mo(V))

b. $S = ½$, $\Delta g > 0.4$ (low-spin ferric hemes)

c. $S > 1/2$ (for example Mn(II), high-spin Fe(III) and Co(II))

d. Coupled-spin systems having an $S = ½$ ground state (iron-sulphur clusters).

Reproduced with permission of the copyright owner. Further reproduction prohibited without permission.

In this brief overview only the third case with the specific example of ferric Fe (III) will be considered in more detail because it is of great importance for the understanding of the EPR spectra of high spin heme enzymes presented in this thesis.

B.5 EPR spectroscopy of Fe (III)

Fe(III) has 5 electrons in the d orbitals and two cases exist: high- or low-spin state, with the total spin S equal to ½ and 5/2 respectively (special circumstances can give the intermediate case, S = 3/2). For the high spin case, the interaction between the unpaired electrons and the crystal field induces differences in the energy of the spin substates (M_s = ±1/2, ±3/2, ±5/2, each a pair of Kramer's doublets) even in the absence of an external magnetic field. This is called zero-field splitting, ZFS. The difference in the energies of the spin substates is present only if the symmetry of the ligand field is lower than the ideal octahedral geometry. The characteristics of EPR spectra for S = 5/2 systems are very sensitive to deviations from such cubic symmetry. For axial distortions, the magnitude of the splitting between the three Kramer's doublets is determined by the parameter D, defined as the zero-field splitting parameter.

a. If D = 0, the levels converge and one single EPR signal is observed at g = 2. The selection rule is ΔMs = ± 1 and all the levels are equally separated (Figure B.3 (a)).
b. With values of D smaller than the microwave quantum ($h\nu$), a small zero-field splitting in the energy levels occurs (Figure B.3 (b)).
c. For 2D > $h\nu$ the separation of the energy levels is large. For commonly available magnetic fields used in EPR spectroscopy, the selection rule ΔMs = ± 1 is satisfied only for transitions within the Ms = ±1/2 levels. If the

Reproduced with permission of the copyright owner. Further reproduction prohibited without permission.

external field (H) is parallel to D a single resonance is observed at g = 2. When the external field is perpendicular to D a unique situation arises. Since the unpaired electrons gain an energetic advantage in the interaction with the ligand field, they tend to stay aligned with the symmetry axis of the ligand field and not with the external magnetic field; therefore, when the external field is perpendicular to one of the symmetry axes (for the axial case), it 'sees' a spin component that is larger compared to the one when it was parallel to D. In most high-spin Fe (III) heme systems, this "effective" g-value is around 6 (Figure B.3 (c)).

For symmetries lower than axial, a second parameter, E, is introduced to describe the rhombic distortion. The $g_{\perp}$ is split into g_x and g_y and the ratio E/D determines the three different g-values (102). This situation is often found for distorted heme complexes (Chapter 4).

In the presence of strong axial ligand fields, the high-spin form of Fe(III) is converted to the low-spin form, with S = ½. The axial ($g_{\perp}$ and $g_{\parallel}$) and rhombic ($g_x \neq g_y \neq g_z$) cases have g-values that range from close to 4.0 to less than 2.0. Examples of these systems are also reported on in Chapter 4.

An important characteristic of Fe (III) in biological systems is that EPR signals are subject to broadening because the spin-lattice relaxation times are very short (103). These absorptions cannot be observed at room temperature. Even though the EPR signals are detectable at liquid nitrogen temperature, only liquid-helium temperature allows for observation of sharp and well resolved lines in EPR spectra for most cases.

B.6 Spin coupling interaction in Compound I

Reproduced with permission of the copyright owner. Further reproduction prohibited without permission.

The EPR theory presented above can be used to interpret the spectrum of the peroxidase cycle intermediate Compound I described in Chapter I as an oxoferryl iron protoporphyrin (IX) π-cation radical. In this complex, which is two electrons higher in oxidation state than its ferric precursor, the heme iron electronic configuration is $3d^4$ low-spin (S =1). The heme group is missing one electron in the highest occupied molecular orbital of the porphyrin, which has been oxidized to a π-cation radical. Schultz et al. described this model consisting of an S = 1 oxoferryl moiety and a S' = ½ porphyrin π-cation radical with an exchange interaction $\boldsymbol{H}_{ex} = \mathbf{S}\cdot\mathbf{J}\cdot\mathbf{S'}$ where **J** is a tensor, but usually it is sufficient to consider only the isotropic exchange $H_{ex} = J\,\mathbf{S}\cdot\mathbf{S'}$ where J is a scalar.

The system can be described by the Hamiltonian:

$H = H_0 + H_{ex} + H_z$

H_0 is the zero field splitting, H_{ex} is the exchange interaction and H_z is the Zeeman interaction. The solutions of the Hamiltonian give the relations between D, E, and g. Each set of D, E, and g values allows determination of the eigenfunctions and eigenvalues of H. The six eigenfunctions of the Hamiltonian give six energy levels for the oxoferryl porphyrin π-cation radical and they form three Kramer's doublets. For axial symmetry and isotropic J, the eigenfunctions depend only on the ratio J/D once the g value is specified. The lowest doublet is well separated in energy from the others and it is the one that gives rise to the EPR signal (S_{eff} = ½) observed for Cmpd I in many proteins.

Quantum mechanical calculations allow defining an effective g-tensor, $\mathbf{g}_{eff}$ for the lowest Kramer's doublet. For isotropic J, and E = 0, it is possible to determine $(g_{\parallel eff})^2$ and $(g_{\perp eff})^2$ as a function of J/D. The g-value along the heme normal (z axis) is almost constant for all

Reproduced with permission of the copyright owner. Further reproduction prohibited without permission.

J/D values, $(g_{\parallel eff})^2 \approx 2$, while the $(g_{\perp eff})^2$ which characterizes the magnetic moment in the heme plane, varies with J/D from 4 to zero for $J > 0$ and from 4 to 19 for $J < 0$ (104). Therefore, the spin coupling in a particular Compound I intermediate can be characterized by the sign and magnitude of the exchange parameter, J, and of the zero-field splitting parameter, D, measured based on temperature dependence of the EPR linewidths. Many systems have been studied and they present a variety of exchange coupling values from ferromagnetic ($J < 0$ and $g_{\perp eff}$ monotonically increases with J/D) to antiferromagnetic ($J > 0$ and $g_{\perp eff}$ passes through zero at $J/D \cong 0.4$). For example, Compound I in lignin (LiP) peroxidase I, catalase I and Ascorbate peroxidase I shows ferromagnetic exchange with $J < 0$ and J/D 0.29, 0.40 and 0.28 respectively (67), while chloroperoxidase I exhibits antiferromagnetic exchange with $J > 0$ and $J/D = 1.02$ (104). HRP exhibits weak exchange and it has been considered to represent both ferro- and antiferromagnetic coupling (68).

These examples illustrate that different EPR spectra can be observed for Cmpd I: axial EPR spectra are detected with $g_{\parallel eff} \approx 2$ and varying $g_{\perp eff}$ as a function of J/D, a singlet EPR signal $g \cong 2$ can be observed in the particular case in which $J > 0$ and $J/D \cong 0.4$ and theoretically EPR silent species should arise if the J/D ratio is particularly small.

The sign and magnitude of the exchange interaction depends on structural features of the heme complex under study (104). For instance, it has been suggested that the variation from ferromagnetic to antiferromagnetic coupling is directly related to an increasing departure from the four-fold symmetry typical of iron porphyrins. Such changes in geometry can be attributed to π-bonding between the Fe and the proximal endogenous ligand (a histidyl imidazole in peroxidases). Therefore, not only the type of

Reproduced with permission of the copyright owner. Further reproduction prohibited without permission.

proximal axial ligand, but also its π-bonding characteristics determine the exchange coupling constant, J (79).

B.7 Quantum mechanically mixed spin (QS) state

In 1974 Martin M. Maltempo reported for the first time the identification of an unusual magnetic state for the bacterial heme protein ferricytochrome c' (89). He claimed that the unusual magnetic properties of this protein could be attributed to a ground-state heme-iron electronic configuration that is a unique quantum mechanical admixture of an intermediate (S=3/2) spin state and a high spin (S=5/2) state. It has been proven that this QS state is different from a thermal mixture of spin states and is instead a single magnetic species with magnetic properties distinct from either pure spin state. The effect responsible for the mixing of spin states is the spin-orbit coupling interaction. Maltempo was able to show through calculation that the admixing of a spin quartet ($^4A_2$, S = 3/2) and a spin sextet ($^6A_1$, S = 5/2) in a $3d^5$ heme-iron electronic configuration via spin-orbit coupling for the formation of the QS state was possible only if the crystal field parameter Δ (energy separation between the unperturbed $^4A_2$ and $^6A_1$ states in the absence of spin-orbit interaction) was at least of the same order of magnitude as the spin-orbit coupling parameter, λ. The relative contribution of the 3/2 and 5/2 states to the QS admixture can be determined as a function of the ratio Δ/λ (89). Theoretical calculation of the EPR g values for the QS state led to the conclusion that the observed g-values can vary from a minimum of 4 for large positive values of Δ/λ (the unperturbed state $^4A_2$ lying below the $^6A_1$ state) to a maximum value of 6 for large negative values of Δ/λ (the unperturbed state $^6A_1$ lying below the $^4A_2$ state) (89). Figure B.4 shows the ordering of the d orbitals for high (a) and low (b) spin heme and the iron-ligand configurations reported by Maltempo

Reproduced with permission of the copyright owner. Further reproduction prohibited without permission.

(89) together with his model proposed for quantum admixed spin state (c). According to this model, a QS spin state can be stabilized in a heme-iron conformation in which the iron is at a position intermediate between its out-of-plane position considered to be found in 5-c HS heme and the in-plane position typical of 6-c LS species. In this first description, the strength of the axial ligand bonds to the heme iron was supposed to be similar to the one reported for HS configuration. Different admixtures of intermediate spin (S = 3/2) and high spin (S = 5/2) states within the QS state reflect the different distances of the iron from the plane of the heme in this model. From the experimental point of view, Maltempo stated that the QS heme state is characterized by a single set of resonance Raman marker bands intermediate in position between the bands assigned to high spin and low spin heme iron; a single EPR spectral species with a $g_{\perp}$ between 4 and 6; paramagnetic susceptibility values intermediate between those for low and high spin; and a Mössbauer spectrum in small applied fields consisting of a four-line hyperfine pattern (89). Certain of these criteria have been found in heme peroxidase spectra including some data presented in Chapter 4 for the *M. tuberculosis* KatG enzyme.

After the initial publications of Maltempo, the QS state has been identified and investigated in many heme proteins and different theoretical models have been presented to fully explain this unusual spin state (105-108). It has been also suggested that identification of the QS spin state using EPR spectroscopy can be made if the average of the g_1 and g_2 values (g_{avg}) for a rhombic EPR signal is between 4 and 6, similar to the definition that the $g_{\perp}$ falls in this range as originally defined (109). A correlation between heme structure and spectroscopic parameters for an iron porphyrin complex, including

Reproduced with permission of the copyright owner. Further reproduction prohibited without permission.

Raman and EPR results, has provided some documentation for the model (88,91,107,110).

The quantum mechanically mixed spin state is very rare. The spin admixture has been observed mainly in the heme protein cytochrome c'. In one recent example, the magnetic susceptibility was evaluated for a ferricytochrome historically considered to exemplify QS heme (the relative EPR signal has g_{avg} between 4 and 6, that led to assignment of a 40% contribution of the 3/2 spin state to the QS spin state). In this case, the susceptibility was most consistent with high spin iron (111). Another example had been previously reported for a ferricytochrome of another organism for which the EPR results predicted a high contribution of the s = 3/2 state to the QS spin state whereas a pure high-spin state was found using NMR spectroscopy (112). These discrepancies are still difficult to explain, and controversial results cast some doubt on the existence of the QS spin state. Nevertheless, certain heme proteins do exhibit unusual ν_3 band frequencies as well as unusual EPR spectra assigned in current literature as additional examples of QS heme.

In peroxidases the existence of the QS spin state has been reported for horseradish peroxidase (113), barley peroxidase (90) and soybean peroxidase (114). These enzymes belong to Class III peroxidases. EPR and resonance Raman studies on barley peroxidase at different pH values, at room temperature and 20 K have shown that in this protein there is the coexistence of 6- and 5-c HS heme with QS spin state and most importantly the QS heme form seems to predominate at high pH and low temperature (90). This provided some guidelines we refer to in Chapter 4 for KatG.

Reproduced with permission of the copyright owner. Further reproduction prohibited without permission.

The possible structural origins for the QS spin state include: a weak axial ligand field (which more recently has been ruled out as the most important feature); and heme distortions, including saddling and ruffling. Computational studies have been presented to show the relationship between spin state and the out-of-plane displacement of the iron in Fe-porphyrins (108); other studies have investigated the possible influence of heme deformations such as saddling and ruffling, on iron spin state (90), but none of these studies has been conclusive.

The QS heme has been historically associated with 5-c hemes. Only three years ago Indiani et al. (86) assigned QS heme to a 6-c Class III peroxidases containing the small molecule benzhydroxamic acid bound near the heme. The 5- and 6-c QS assignments were characterized by slightly different resonance Raman frequencies and electronic absorption wavelengths (86) and unique EPR signals.

Reproduced with permission of the copyright owner. Further reproduction prohibited without permission.

Figures and Tables

Reproduced with permission of the copyright owner. Further reproduction prohibited without permission.

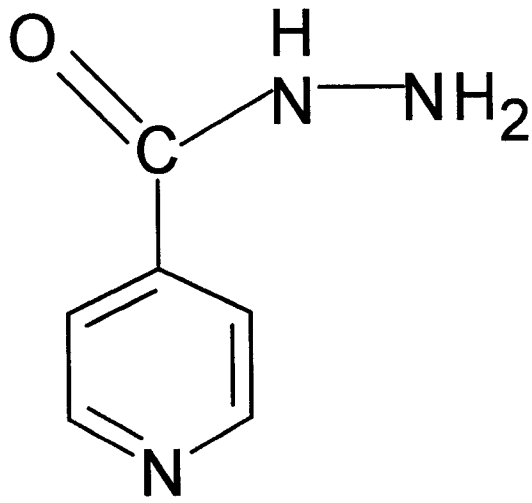

Figure 1.1 Isonicotinic acid hydrazide; Isoniazid; INH.

Reproduced with permission of the copyright owner. Further reproduction prohibited without permission.

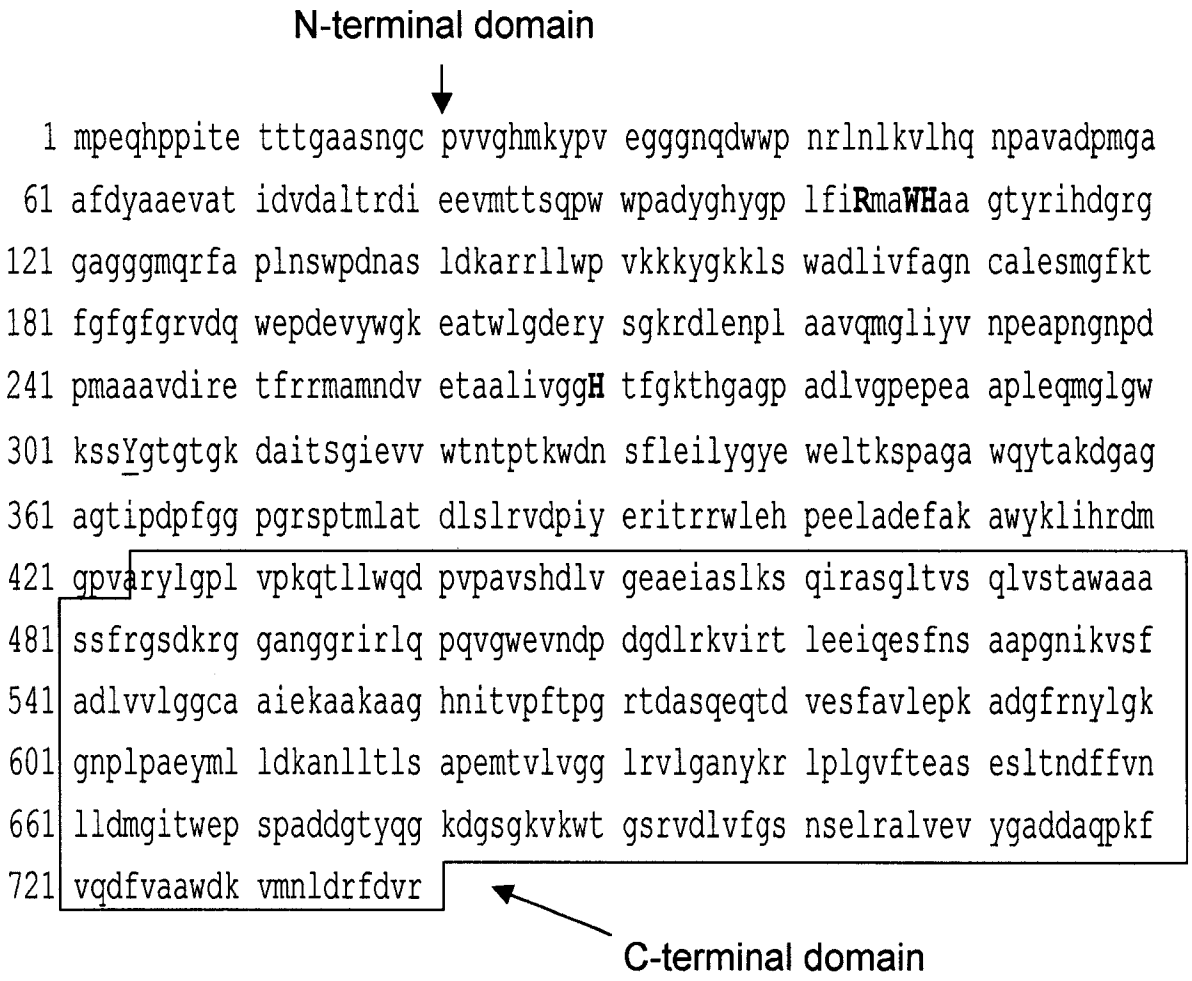

Figure 1.2 Amino acid sequence of *M. tuberculosis* catalase-peroxidase (115). Figure 1.3 shows details of the active site.

Reproduced with permission of the copyright owner. Further reproduction prohibited without permission.

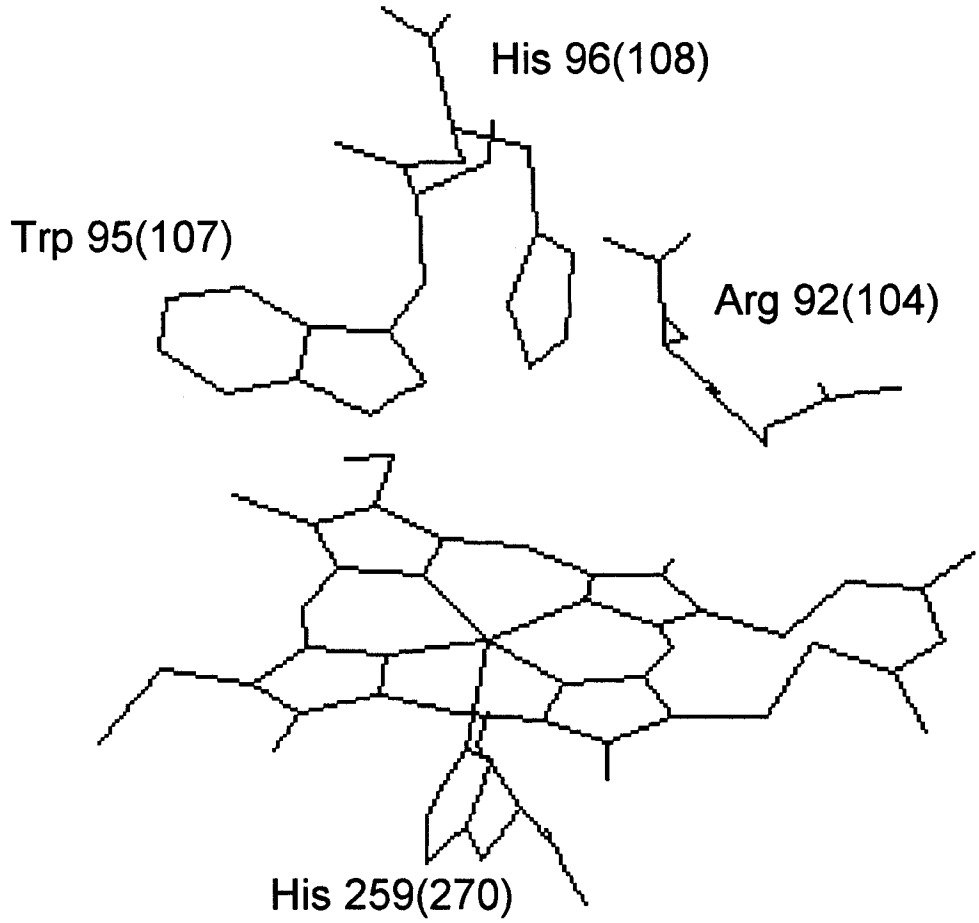

Figure1.3 Active site of catalase-peroxidase from *H. marismortui.*

The active site triad arginine, tryptophan and histidine (Arg92-Trp95-His96), located on the distal side of the heme is shown together with the proximal histidine (His259) (19). The numbers in brackets are for *M. tuberculosis* KatG.

Reproduced with permission of the copyright owner. Further reproduction prohibited without permission.

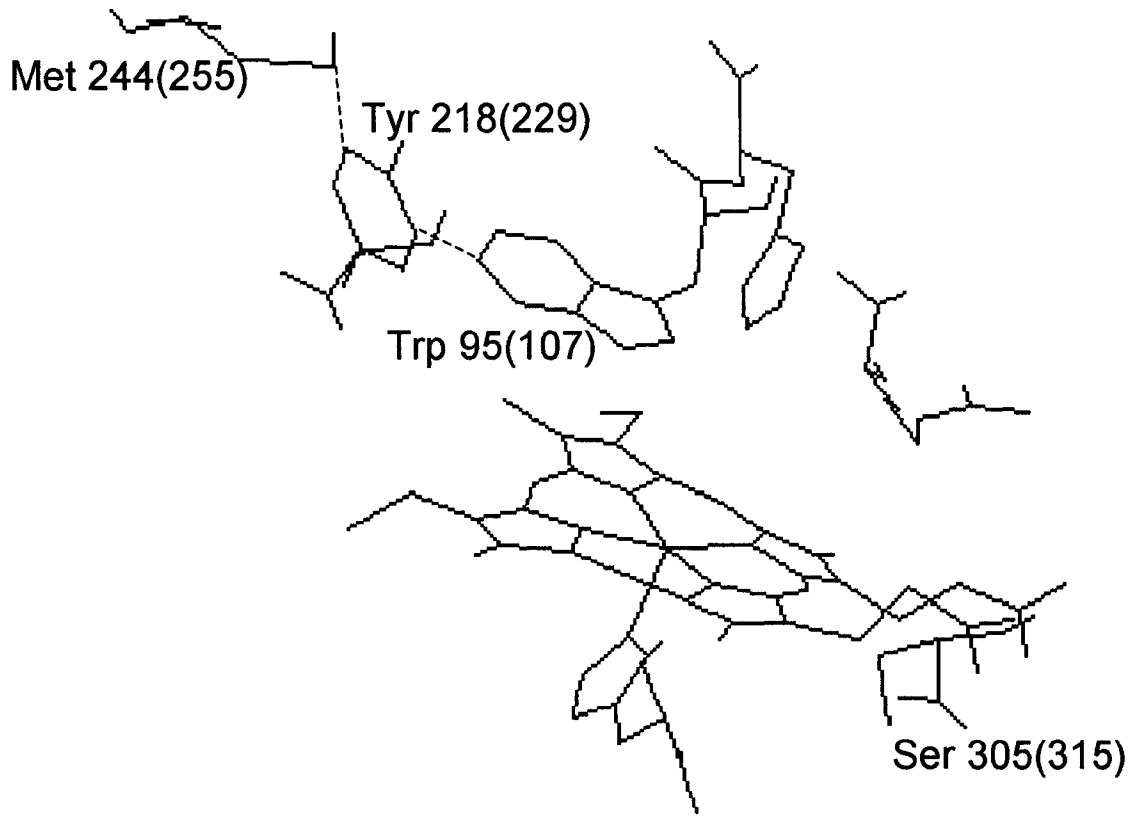

Figure 1.4 Structure of the Trp95-Tyr218-Met244 adduct found in *H. marismortui* KatG. Covalent bonds occur between $C^{\eta 2}$ of Trp95 and $C^{\varepsilon 2}$ of Tyr218, and between $C^{\varepsilon 2}$ and S^{δ} of Met244 (19). The same adduct is found in *B.pseudomallei* KatG (20). The numbers in brackets are for the *M. tuberculosis* KatG.

Reproduced with permission of the copyright owner. Further reproduction prohibited without permission.

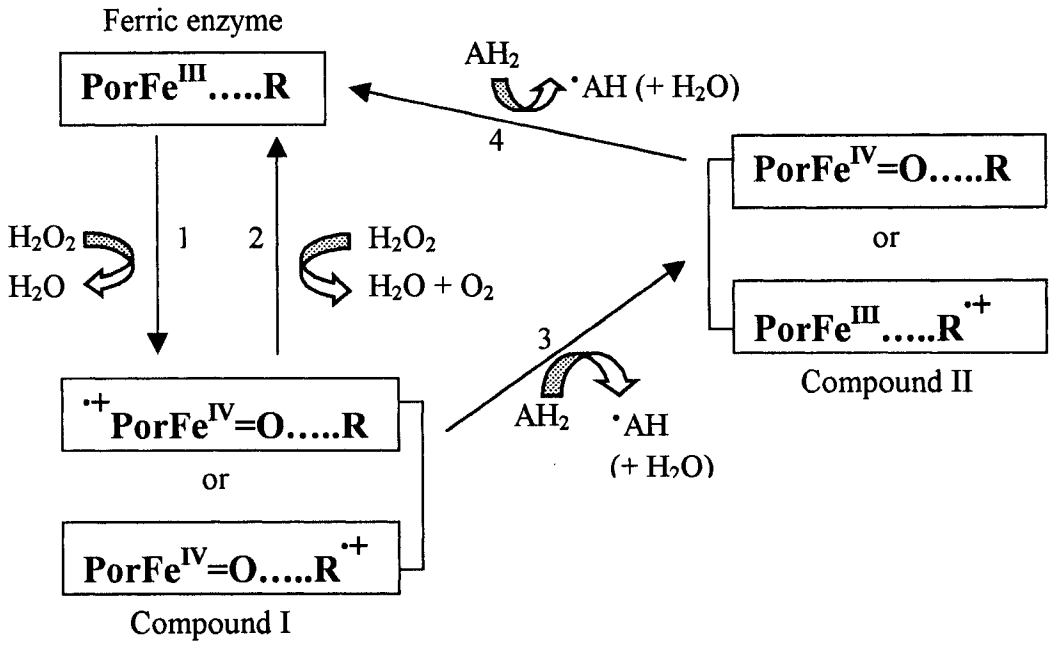

Figure 1.5 Catalase-peroxidase reaction scheme (taken from (23)).

Reproduced with permission of the copyright owner. Further reproduction prohibited without permission.

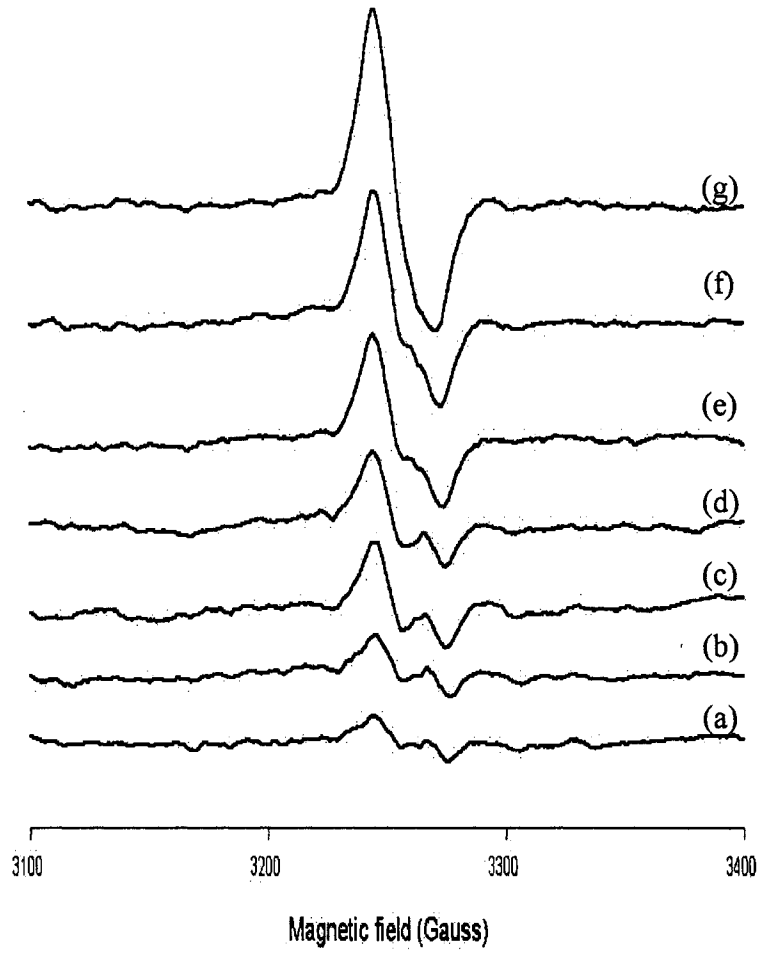

Figure 2.1 Evolution of radical EPR spectra as a function of time. Rapid freeze-quench samples were prepared from KatG (50 μM final) reacted at 25 ° C with PAA (150 μM final) in 20 mM potassium phosphate buffer (pH =7.2). Reaction mixtures were freeze-quenched after 50 ms (a), 100 ms (b), 250 ms (c), 500 ms (d), 2 s (e), 5 s (f), and 10 s (g). The EPR spectra were recorded at 77 K (microwave frequency 9.13 GHz, modulation amplitude 4 G, microwave power 5 mW).

Reproduced with permission of the copyright owner. Further reproduction prohibited without permission.

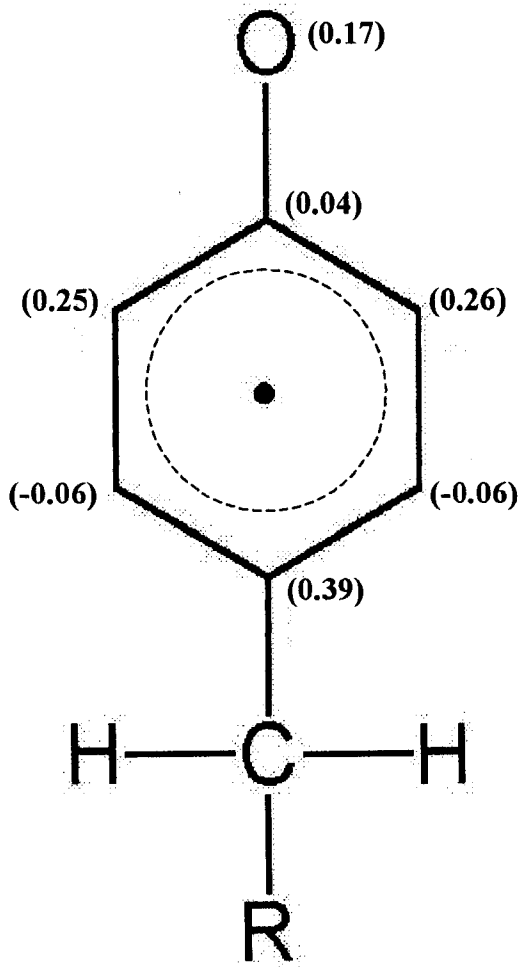

Figure 2.2 Electron spin density distribution in tyrosyl radical based on experimental data and calculations (53).

Reproduced with permission of the copyright owner. Further reproduction prohibited without permission.

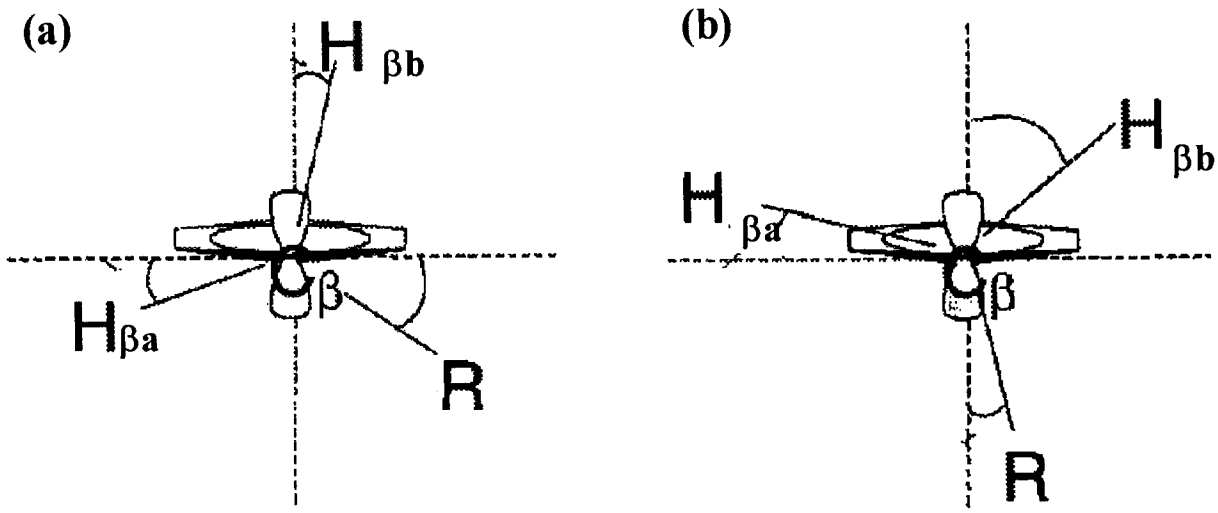

Figure 2.3 Conformations of the β-methylene group of a tyrosyl radical. (a) gives a doublet and (b) a singlet EPR signal (51).

Reproduced with permission of the copyright owner. Further reproduction prohibited without permission.

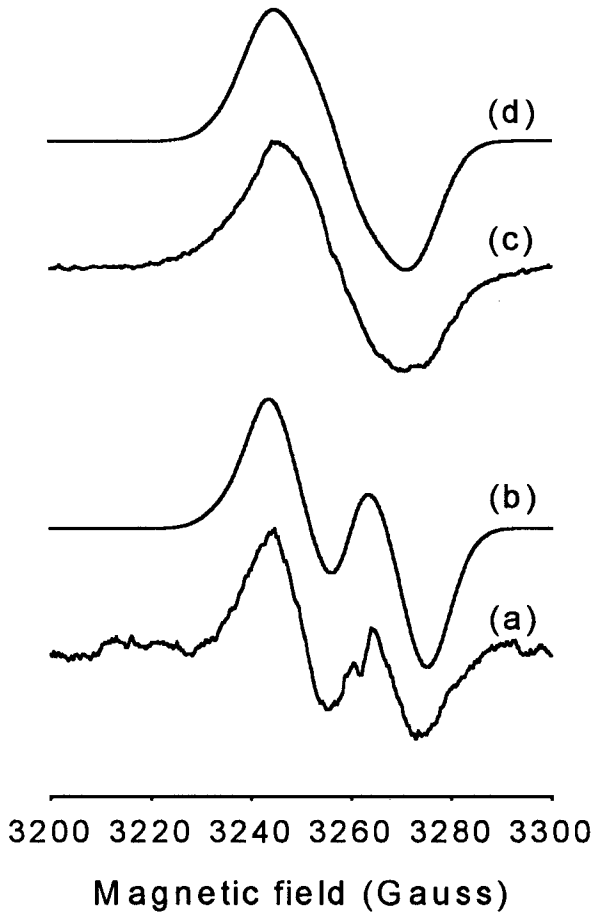

Figure 2.4 Simulation of tyrosyl radical doublet and singlet, X-band EPR spectra. Spectra (a) and (c) are the experimental spectra taken from figure 2.1 (c) and (g) (250 ms and 10 s, respectively); spectra (b) and (d) are the simulations based on the parameters given in Table 2.1.

Reproduced with permission of the copyright owner. Further reproduction prohibited without permission.

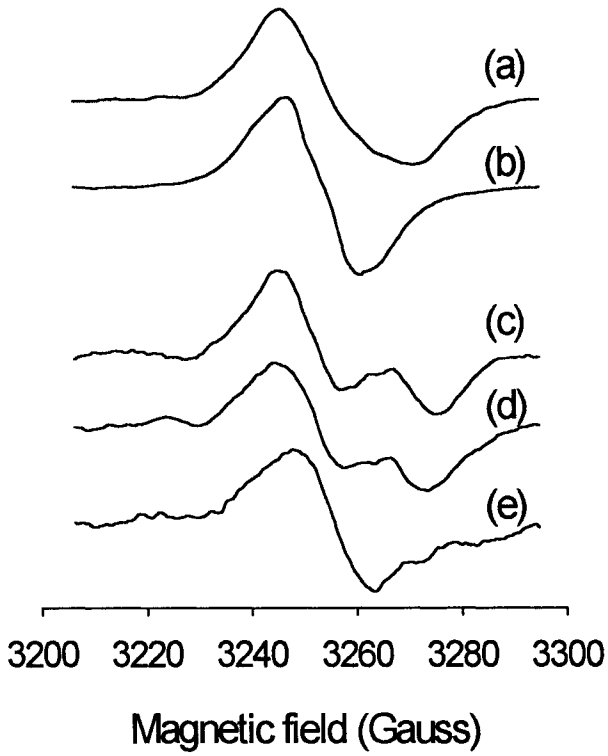

Figure 2.5 EPR spectra of radical species formed in deuterium-labeled KatG. Labeled or unlabeled KatG (50 μM final) was reacted at 25 ° C with PAA (150 μM final) in 20 mM potassium phosphate buffer (pH = 7.2). (a) unlabeled KatG, 10 s reaction; (b) L-3,3-[$^2H_2$]tyrosine-labeled KatG, 10 s reaction; (c) unlabeled KatG, 250 ms reaction; (d) L-2,4,5,6,7-[$^2H_5$]tryptophan-labeled KatG, 200 ms reaction; (e) L-3,3-[$^2H_2$]tyrosine-labeled KatG, 250 ms reaction. EPR spectra were recorded under the same conditions as described in figure 2.1.

Reproduced with permission of the copyright owner. Further reproduction prohibited without permission.

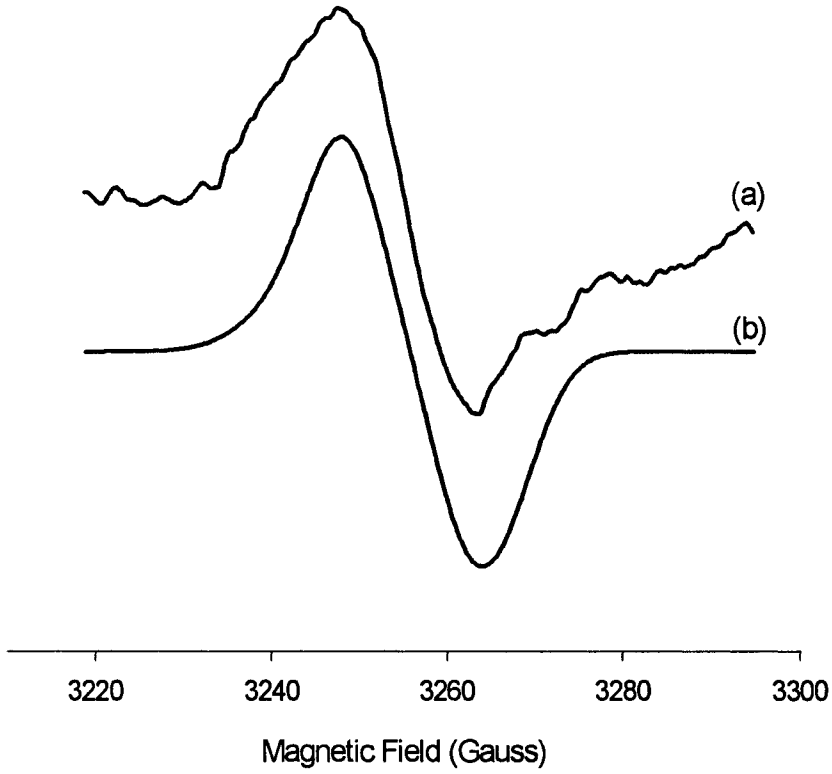

Figure 2.6 Simulation of the EPR spectrum for a tyrosyl radical in L-3,3-[$^2H_2$]tyrosine-labeled KatG. Spectrum (a) is the same as spectrum 2.5 (e) for the L-3,3-[$^2H_2$]tyrosine-labeled KatG reacted with PAA as described in figure 2.5, 250 ms reaction, (b) is the simulation.

Reproduced with permission of the copyright owner. Further reproduction prohibited without permission.

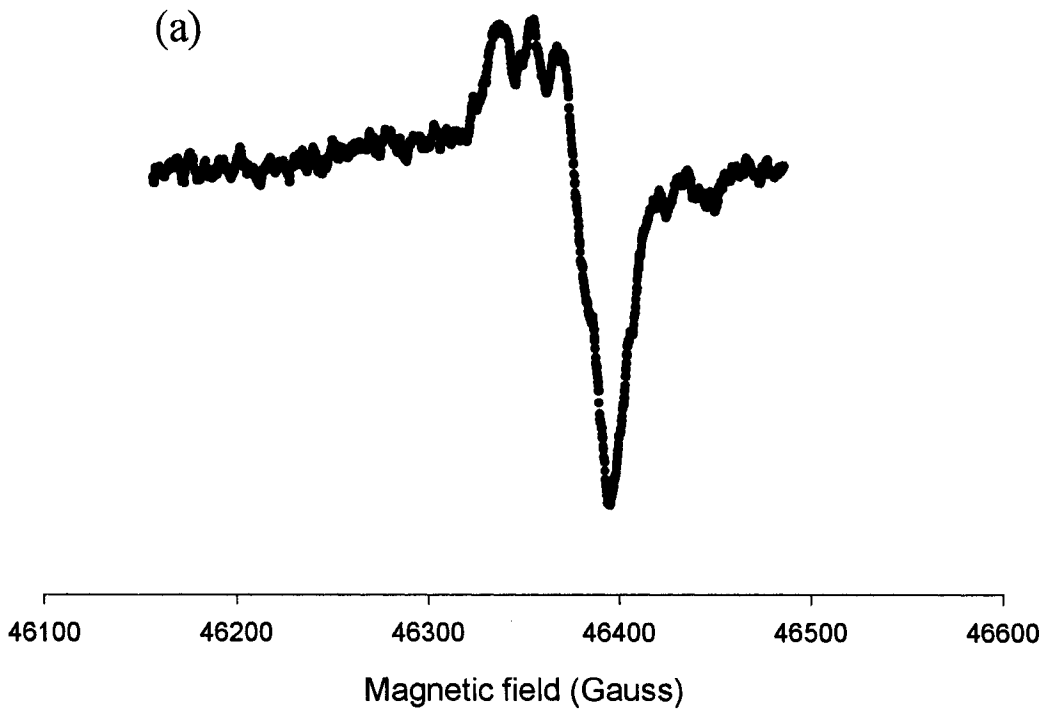

Figure 2.7 RFQ-High-Field (130 GHz) EPR spectra of the protein-based radicals in *M. tuberculosis* catalase-peroxidase. KatG (150 μM final) was reacted at 25 ° C with PAA (450 μM final) in 20 mM potassium phosphate buffer (pH =7.2). Reaction mixtures were freeze-quenched after 700 ms (a) and (10 s).

Reproduced with permission of the copyright owner. Further reproduction prohibited without permission.

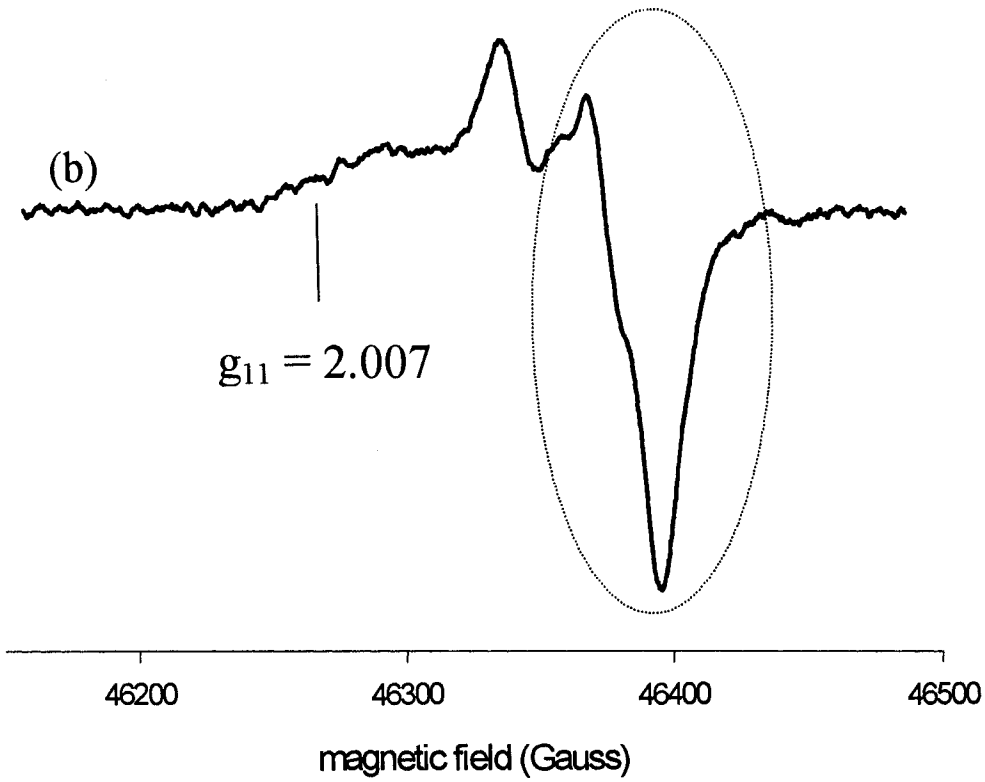

KatG (150 μM final) was reacted at 25 ° C with PAA (450 μM final) in 20 mM potassium phosphate buffer (pH =7.2). Reaction mixtures were freeze-quenched after 700 ms (a) and (10 s).

Reproduced with permission of the copyright owner. Further reproduction prohibited without permission.

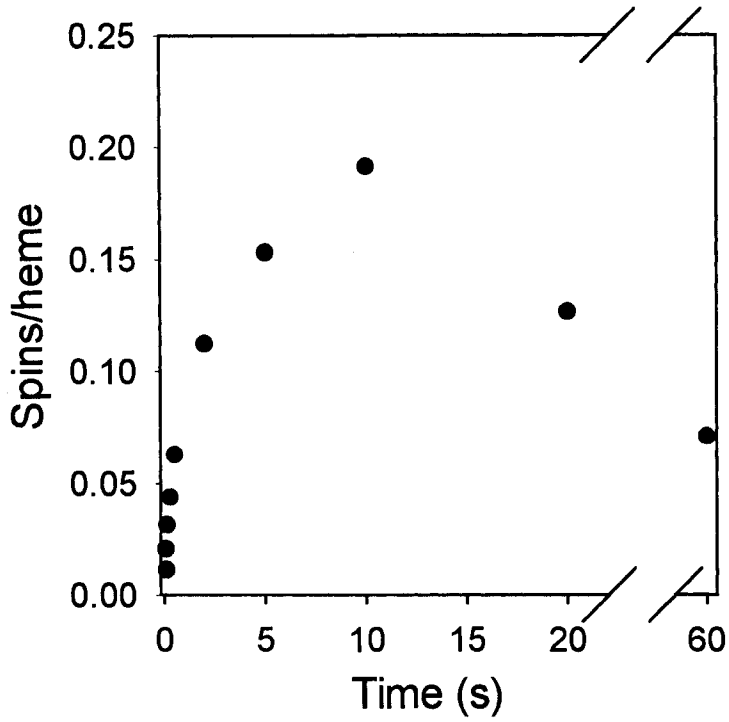

Figure 2.8 Yield (spins/heme) of tyrosyl radical as a function of time. Concentration of tyrosyl radical was evaluated by double integration of EPR signal intensity (in triplicate RFQ-EPR experiments) using KatG (50μM final) reacted with PAA (150 μM final) for the time periods given by the data points.

Reproduced with permission of the copyright owner. Further reproduction prohibited without permission.

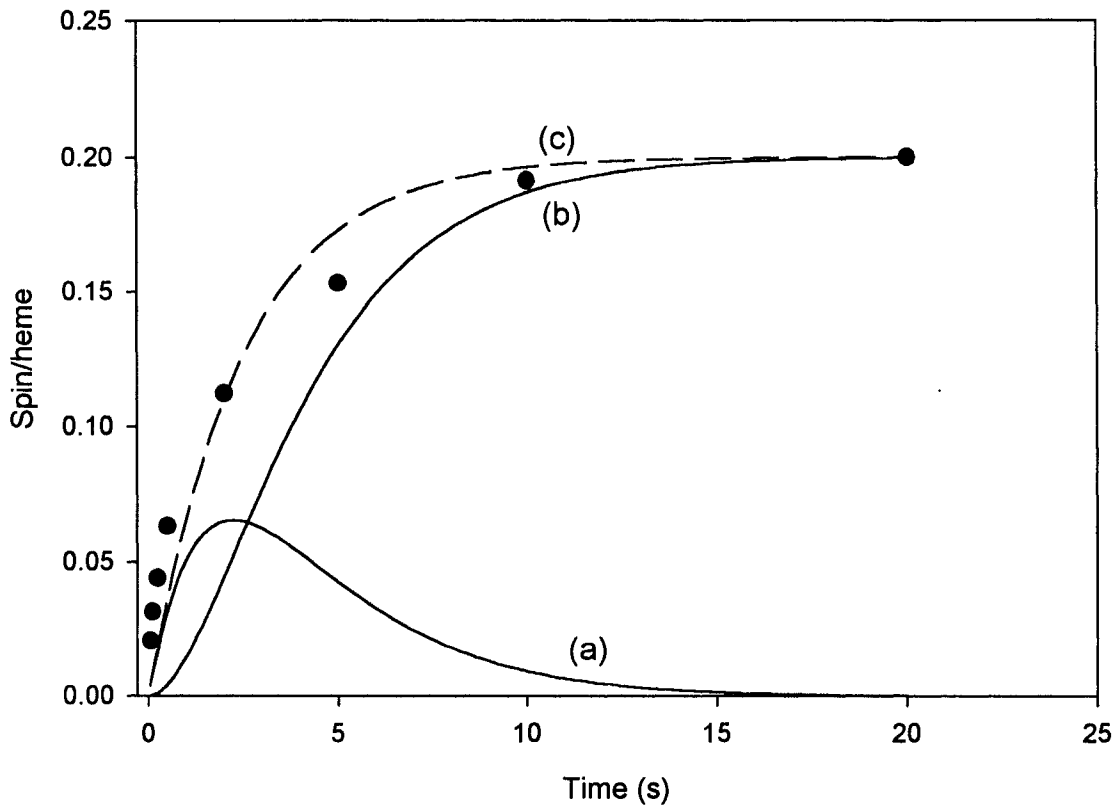

Figure 2.9 Simulation of the rate of formation of tyrosyl radical(s) according to a kinetic model for two consecutive irreversible reactions. Curve (a), formation of product I (tyrosyl radical doublet species); curve (b), formation of product II (tyrosyl radical singlet species); curve (c), sum of curves (a) and (b); (closed circles), tyrosyl radical yield from Figure 2.8.

Reproduced with permission of the copyright owner. Further reproduction prohibited without permission.

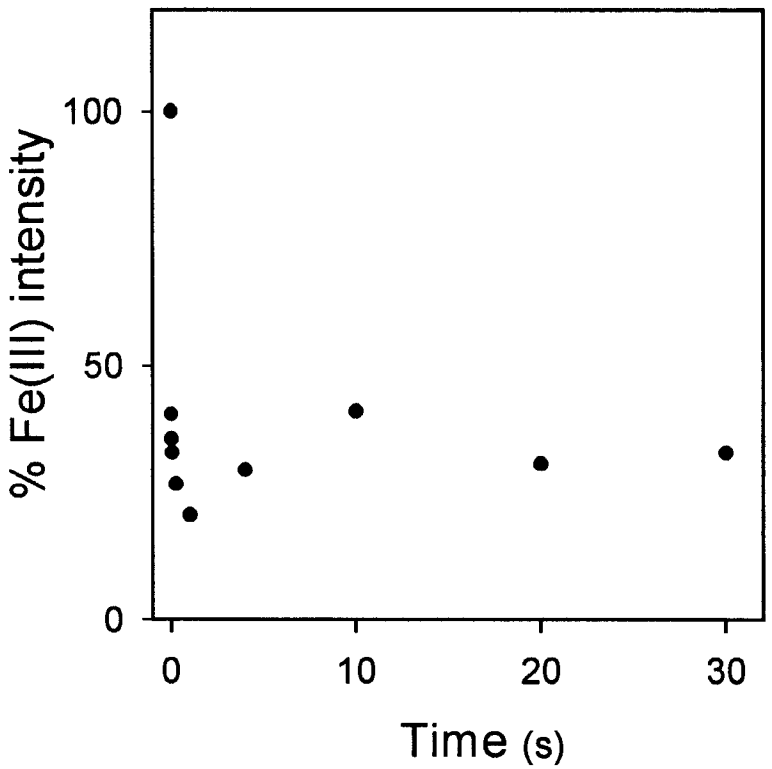

Figure 2.10 Intensity of ferric heme iron EPR signal as a function of time after reaction with peroxyacetic acid. Relative intensity due to the residual ferric iron evaluated as the signal height at g = 6.0 in spectra recorded at 5.5 K for the same or similar samples used for observation of the radical formation kinetics.

Reproduced with permission of the copyright owner. Further reproduction prohibited without permission.

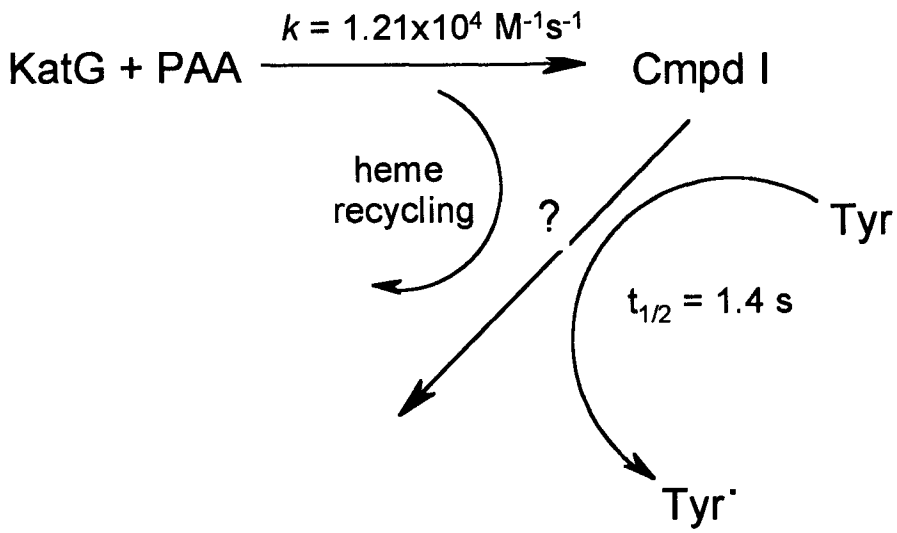

-d[KatG]/dt = k [KatG] [PAA] = k' [KatG] — pseudo first order reaction ($t_{1/2}$ = 50 ms) (observed by EPR spectroscopy)

d[Cmpd I]/dt = k [KatG] [PAA] = k' [KatG] — pseudo first order reaction ($t_{1/2}$ < 50 ms) (observed by SF spectroscopy)

d[Tyr ·]/dt = k''[Cmpd I] — proposed first order reaction ($t_{1/2} \cong$ 1.4 s) (observed by EPR spectroscopy)

Figure 2.11 Kinetic scheme for tyrosyl radical formation in WT KatG.

Reproduced with permission of the copyright owner. Further reproduction prohibited without permission.

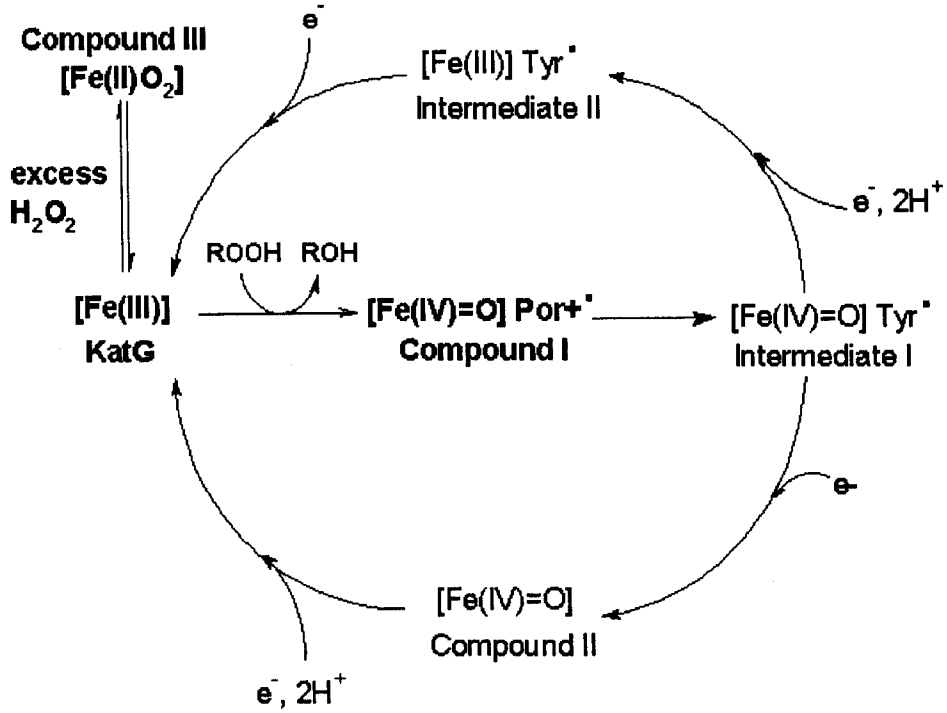

Figure 2.12 Scheme for KatG catalytic cycle. The species shown in bold text are those identified here or in previous work on WT KatG (11,28). Tyr·, tyrosyl radical; Por+·, porphyrin π-cation radical; ROOH, *m*-chloroperoxybenzoic acid, peroxyacetic acid, or *t*-butylhydroperoxide.

Reproduced with permission of the copyright owner. Further reproduction prohibited without permission.

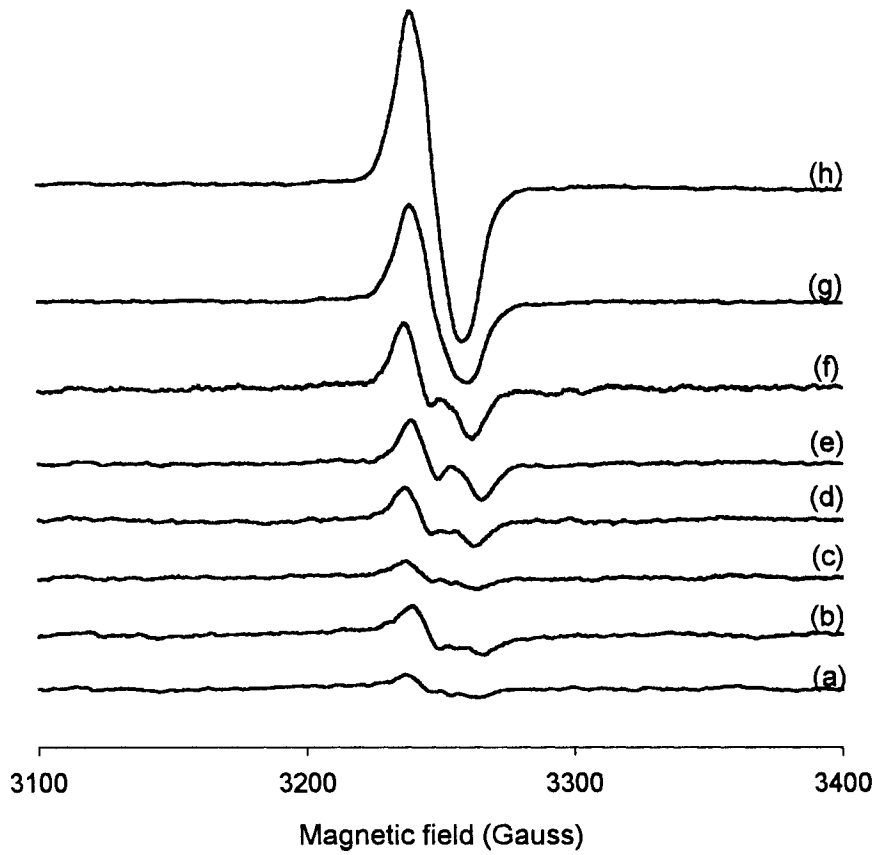

Figure 3.1 Evolution of tyrosyl radical EPR spectra in KatG[Y98F] during the reaction of resting enzyme with peroxyacetic acid. KatG[Y98F] (50 μM final) was reacted at 25 ° C with PAA (150 μM final). Reaction mixtures were freeze-quenched after (a) 6.4 ms; (b) 10 ms; (c) 50 ms; (d) 100 ms; (e) 250 ms; (f) 500 ms; (g) 5 s; (h) 10 s. Experimental conditions: temperature, 77 K; microwave frequency, 9.120 GHz; modulation amplitude, 4 G; microwave power, 5 mW.

Reproduced with permission of the copyright owner. Further reproduction prohibited without permission.

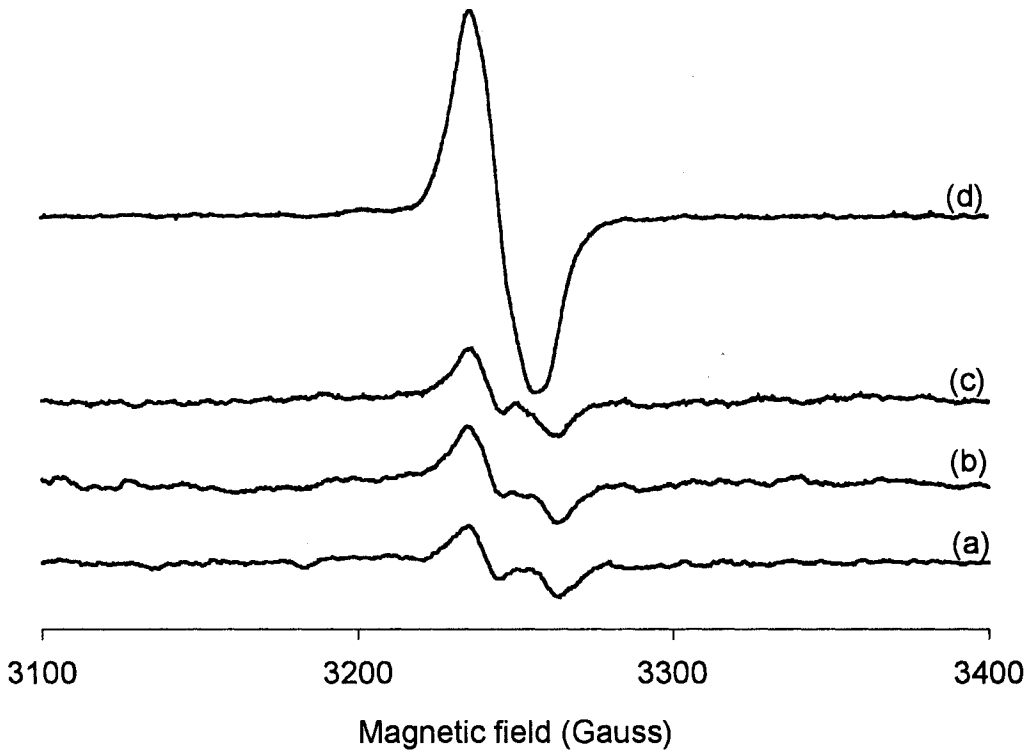

Figure 3.2 Evolution of tyrosyl radical EPR spectra in KatG[Y113F] during the reaction of resting enzyme with peroxyacetic acid. KatG[Y113F] (50 μM final) was reacted at 25 ° C with PAA (150 μM final). Reaction mixtures were freeze-quenched after (a) 10 ms; (b) 50 ms; (c) 250 ms; (d) 5 s. Experimental conditions: temperature, 77 K; microwave frequency, 9.120 GHz; modulation amplitude, 4 G; microwave power, 5 mW.

Reproduced with permission of the copyright owner. Further reproduction prohibited without permission.

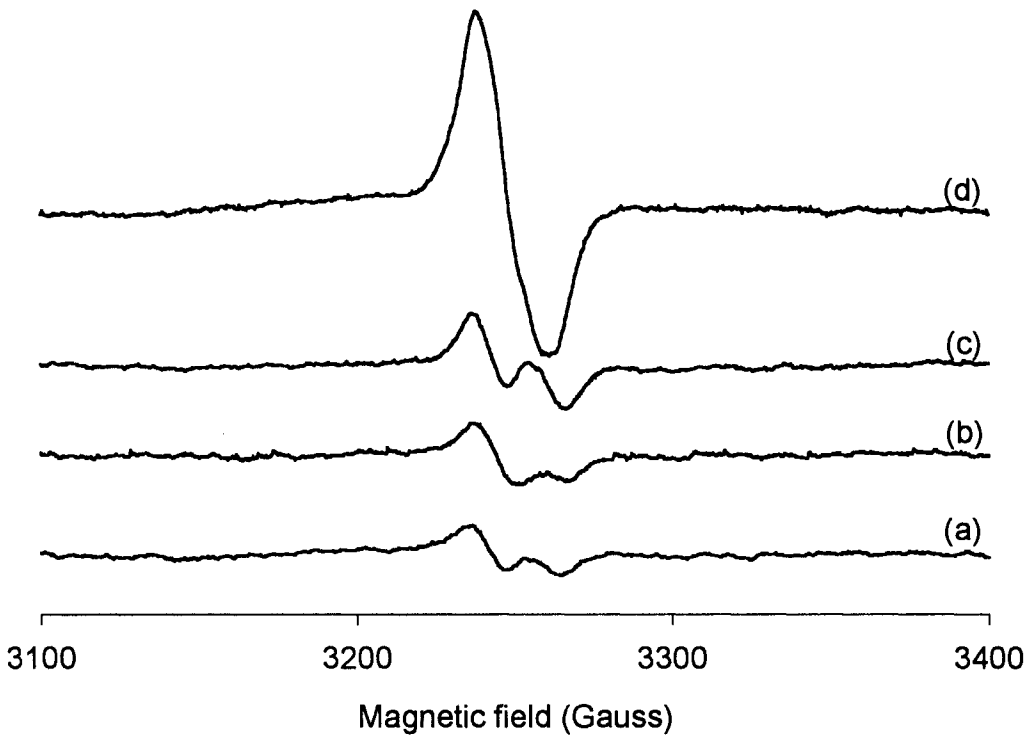

Figure 3.3 Evolution of tyrosyl radical EPR spectra in KatG[Y304F] during the reaction of resting enzyme with peroxyacetic acid. KatG[Y304F] (50 μM final) was reacted at 25 ° C with PAA (150 μM final). Reaction mixtures were freeze-quenched after (a) 50 ms; (b) 250 ms; (c) 500 ms; (d) 5 s. Experimental conditions: temperature, 77 K; microwave frequency, 9.120 GHz; modulation amplitude, 4 G; microwave power, 5 mW.

Reproduced with permission of the copyright owner. Further reproduction prohibited without permission.

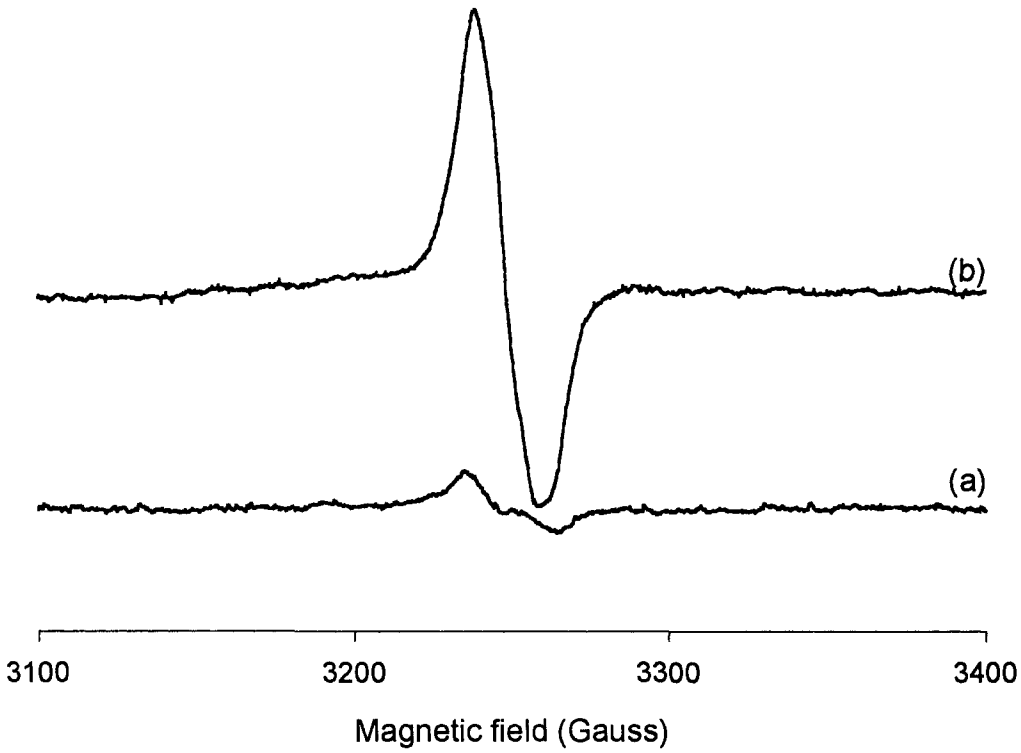

Figure 3.4 Evolution of tyrosyl radical EPR spectra in KatG[Y426F] during the reaction of resting enzyme with peroxyacetic acid. KatG[Y426F] (50 μM final) was reacted at 25 ° C with PAA (150 μM final). Reaction mixtures were freeze-quenched after (a) 250 ms; (b) 5 s. Experimental conditions: temperature, 77 K; microwave frequency, 9.120 GHz; modulation amplitude, 4 G; microwave power, 5 mW.

Reproduced with permission of the copyright owner. Further reproduction prohibited without permission.

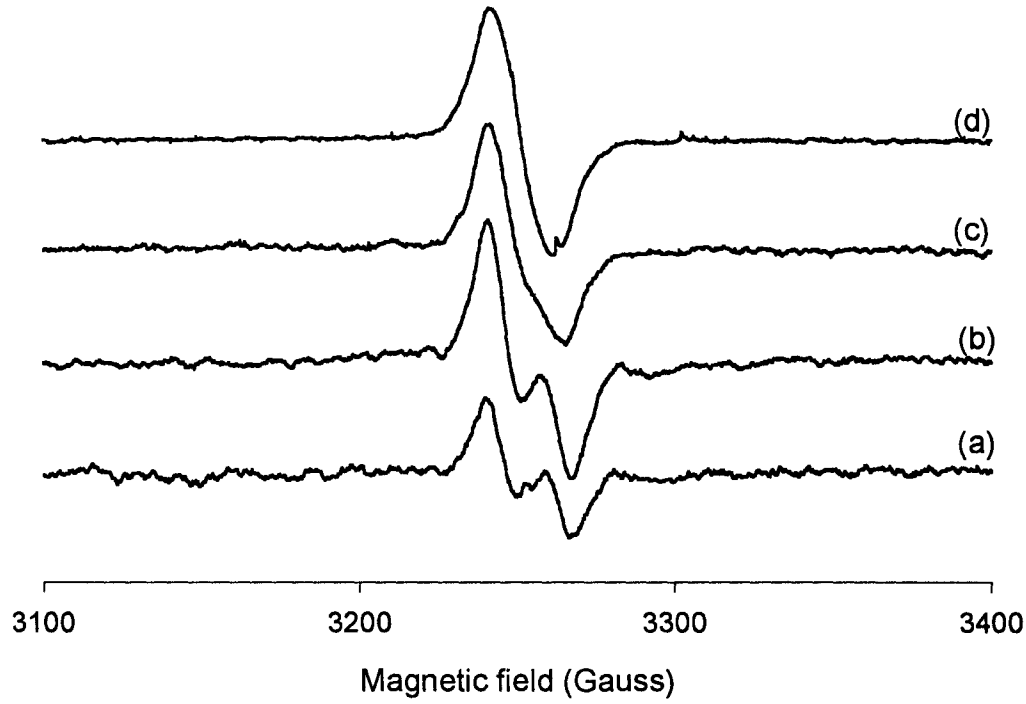

Figure 3.5 Evolution of tyrosyl radical EPR spectra in KatG[Y155S] during the reaction of resting enzyme with peroxyacetic acid. KatG[Y155S] (50 μM final) was reacted at 25 ° C with PAA (150 μM final). Reaction mixtures were freeze-quenched after (a) 50 ms; (b) 250 ms; (c) 2 s; (d) 10 s. Experimental conditions: temperature, 77 K; microwave frequency, 9.120 GHz; modulation amplitude, 4 G; microwave power, 5 mW.

Reproduced with permission of the copyright owner. Further reproduction prohibited without permission.

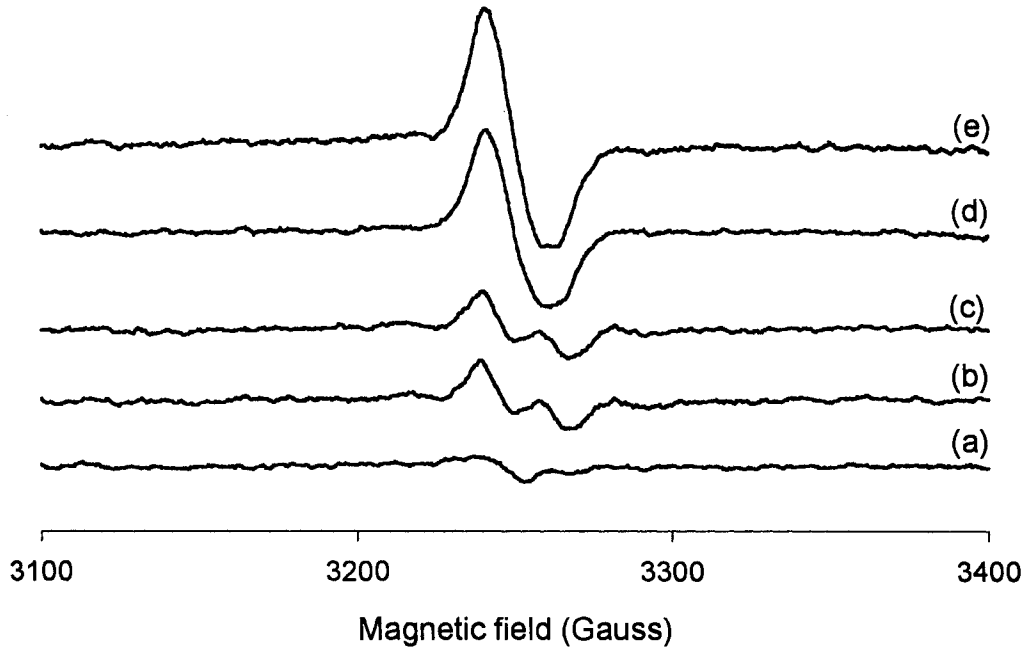

Figure 3.6 Evolution of tyrosyl radical EPR spectra in KatG[S315T] during the reaction of resting enzyme with peroxyacetic acid. KatG[S315T] (50 μM final) was reacted at 25 ° C with PAA (150 μM final). Reaction mixtures were freeze-quenched after (a) 50 ms; (b) 250 ms; (c) 500 ms; (d) 5 s; (e) 10 s. Experimental conditions: temperature, 77 K; microwave frequency, 9.120 GHz; modulation amplitude, 4 G; microwave power, 5 mW.

Reproduced with permission of the copyright owner. Further reproduction prohibited without permission.

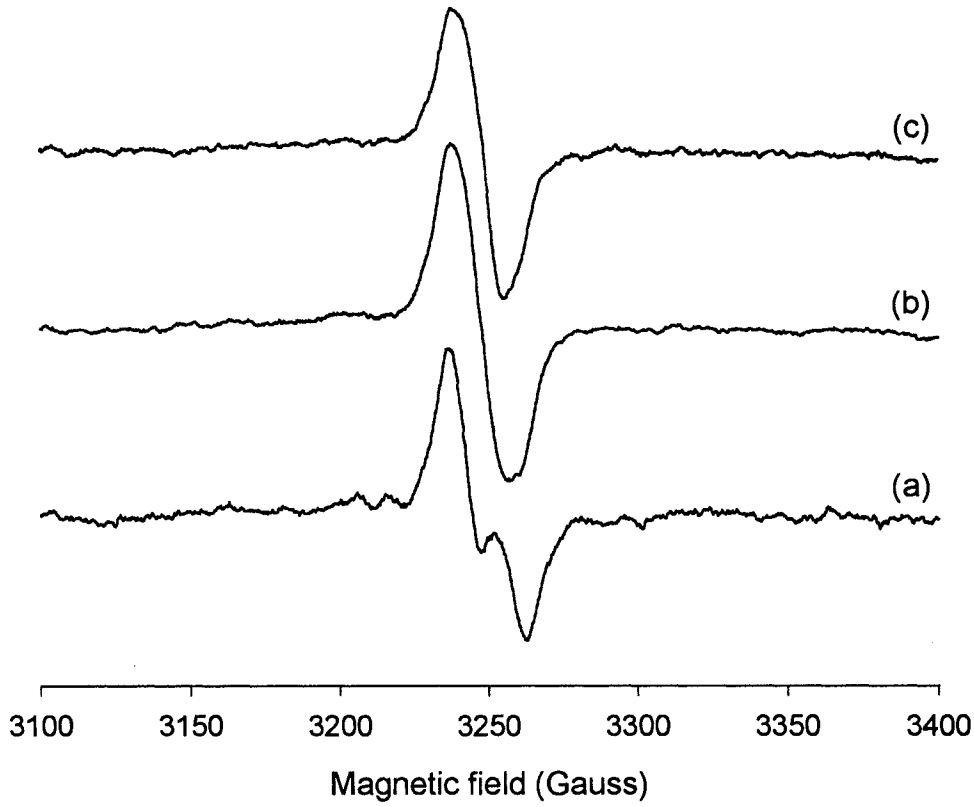

Figure 3.7 Evolution of tyrosyl radical EPR spectra in KatG[Y229F] during the reaction of resting enzyme with peroxyacetic acid. KatG[Y229F] (50 μM final) was reacted at 25 ° C with PAA (150 μM final). Reaction mixtures were freeze-quenched after (a) 10 ms; (b) 100 ms; (c) 5 s. Experimental conditions: temperature, 77 K; microwave frequency, 9.120 GHz; modulation amplitude, 4 G; microwave power, 5 mW.

Reproduced with permission of the copyright owner. Further reproduction prohibited without permission.

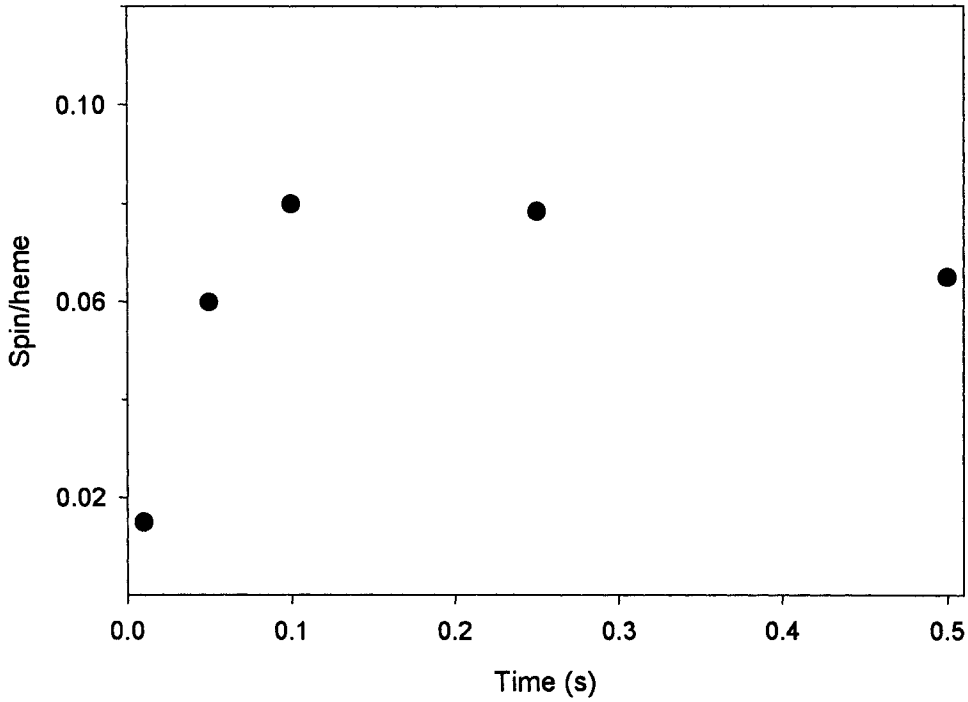

Figure 3.8 Yield of tyrosyl radical as a function of time in KatG[Y229F]. Concentration of tyrosyl radical was evaluated by double integration of EPR signal intensity (Appedix A). Rapid freeze-quench EPR samples were prepared from KatG[Y229F] (50 μM) reacted with PAA (150 μM) and frozen at the time points given by the data.

Reproduced with permission of the copyright owner. Further reproduction prohibited without permission.

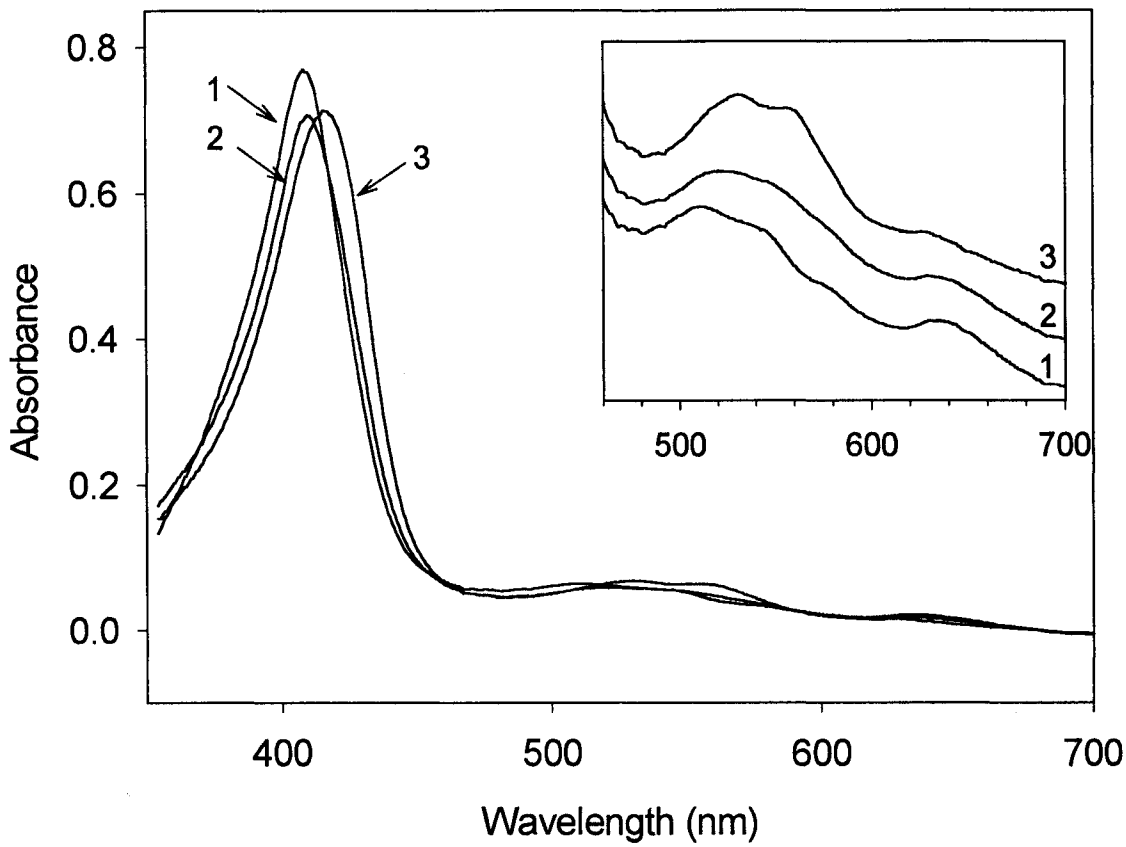

Figure 3.9 Optical stopped-flow absorption spectra of KatG[Y229F] during the reaction with peroxyacetic acid. 1, Resting (ferric) enzyme; 2, Cmpd I (t = 0.016 s); 3, Cmpd II (t = 7.5 s). Inset: visible region of spectra 1, 2 and 3. Final concentrations: KatG[Y229F] 10 μM, PAA 30 μM.

Reproduced with permission of the copyright owner. Further reproduction prohibited without permission.

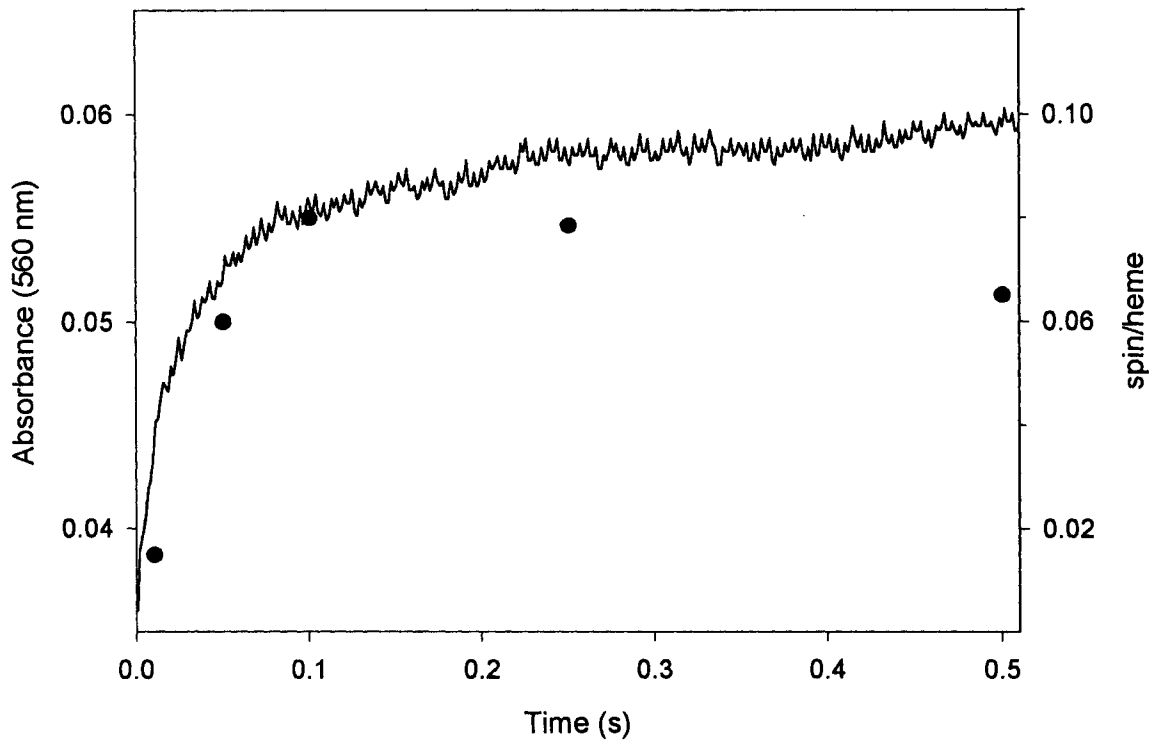

Figure 3.10 Yield of tyrosyl radical and formation of Cmpd II as a function of time in KatG[Y229F]. Rapid freeze-quench EPR samples were prepared from KatG[Y229F] (50 μM) reacted with PAA (150 μM) and frozen at the time points given by the data (as in Figure 3.8). Stopped-flow optical data (solid line) was recorded at 560 nm in a similar reaction mixture.

Reproduced with permission of the copyright owner. Further reproduction prohibited without permission.

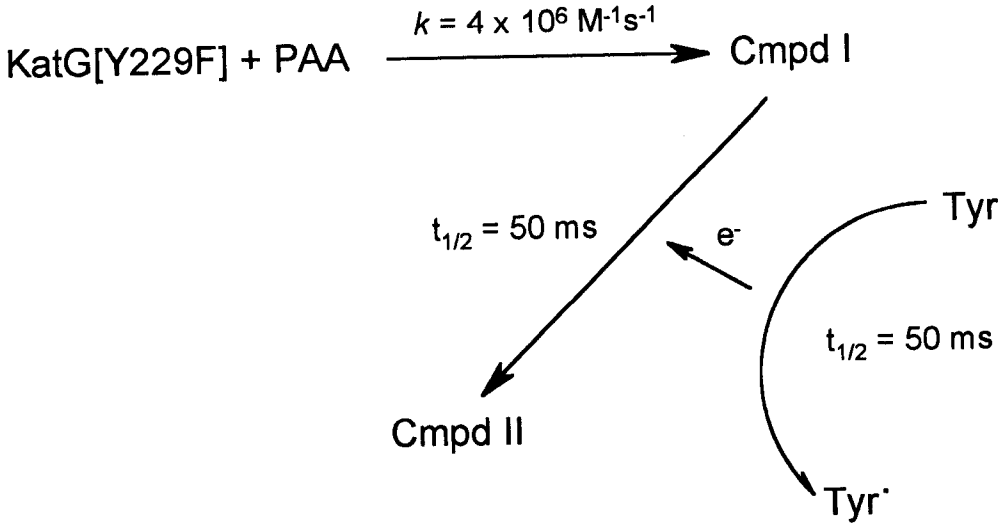

Figure 3.11 Kinetic scheme for tyrosyl radical and Cmpd II formation in KatG[Y229F].

Reproduced with permission of the copyright owner. Further reproduction prohibited without permission.

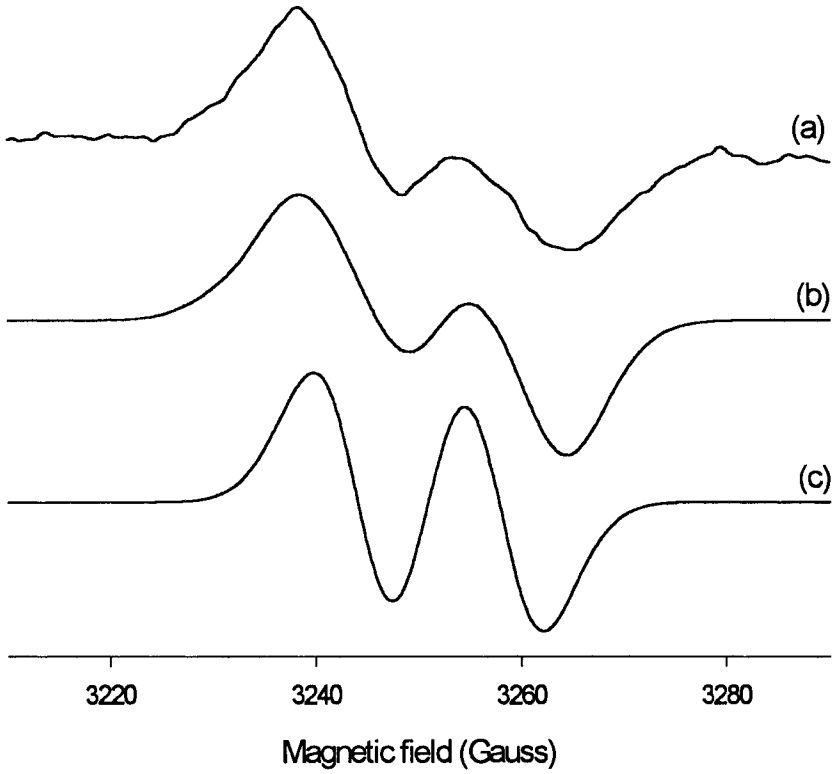

Figure 3.12 Simulation of an EPR spectrum of a tyrosyl radical lacking 3', 5' phenolic hydrogens. (a) Wt KatG (50 μM final) was reacted at 25 ° C with H_2O_2-free PAA (150 μM final). The reaction mixture was freeze-quenched after 250 ms. Experimental conditions were as in Figure 3.1. (b) Simulation of spectrum (a). (c) Simulation of a tyrosyl radical with identical parameter as in (b) except for the absence of the 3', 5' phenolic hydrogens.

Reproduced with permission of the copyright owner. Further reproduction prohibited without permission.

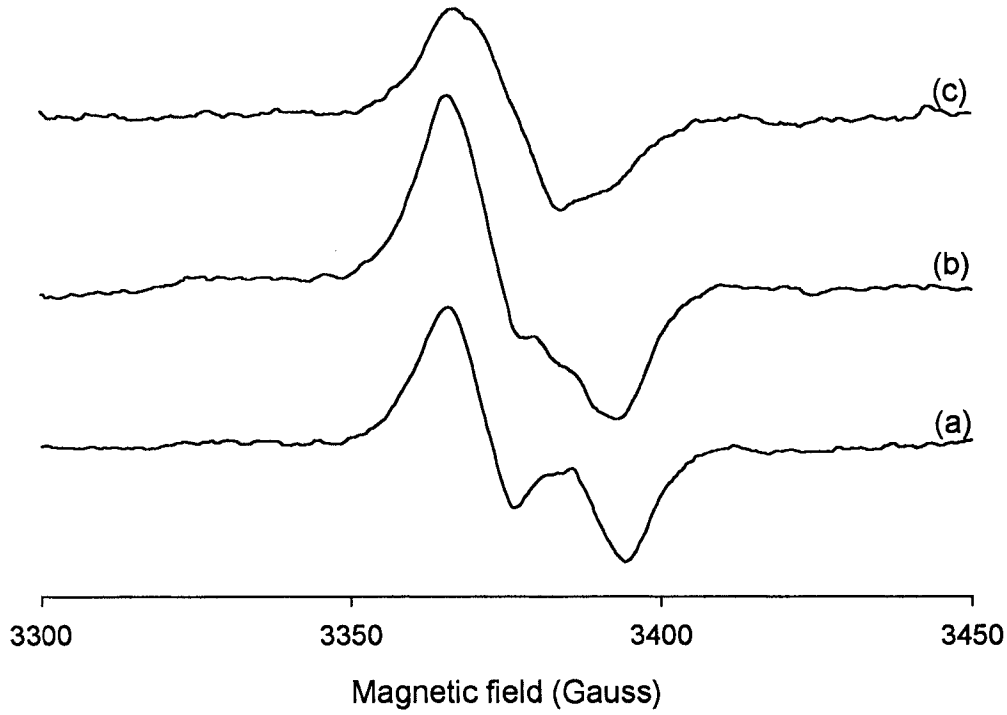

Figure 3.13 Evolution of tyrosyl radical EPR spectra in KatG[Y353F] during the reaction of resting enzyme with peroxyacetic acid. Rapid freeze-quench EPR samples were frozen 250 ms (a), 5 s (b) or 10 s (c) after mixing resting enzyme (50 μM final) with PAA (150 μM final) in 20mM potassium phosphate buffer at 25 ° C. EPR conditions: microwave frequency, 9.48 GHz; modulation amplitude, 1.0 G; microwave power, 1.08 mW; temperature 77 K.

Reproduced with permission of the copyright owner. Further reproduction prohibited without permission.

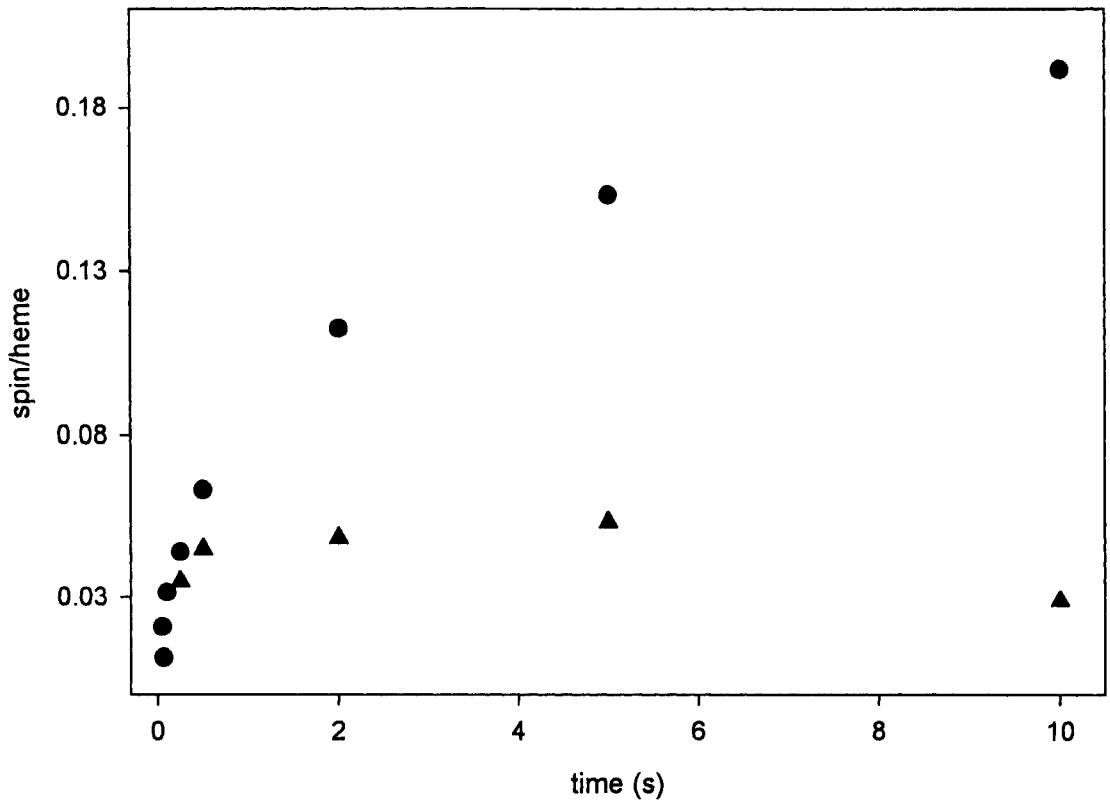

Figure 3.14 Yield of tyrosyl radical in KatG[Y353F]. Time course of tyrosyl radical production (spins/heme) in WT KatG (●) (from Figure 2.8) and KatG[Y353F] mutant (▲). RFQ-EPR samples were prepared as described in Figure 3.13 and were frozen after incubation for the indicated time intervals. EPR recording conditions were the same as in Figure 3.13.

Reproduced with permission of the copyright owner. Further reproduction prohibited without permission.

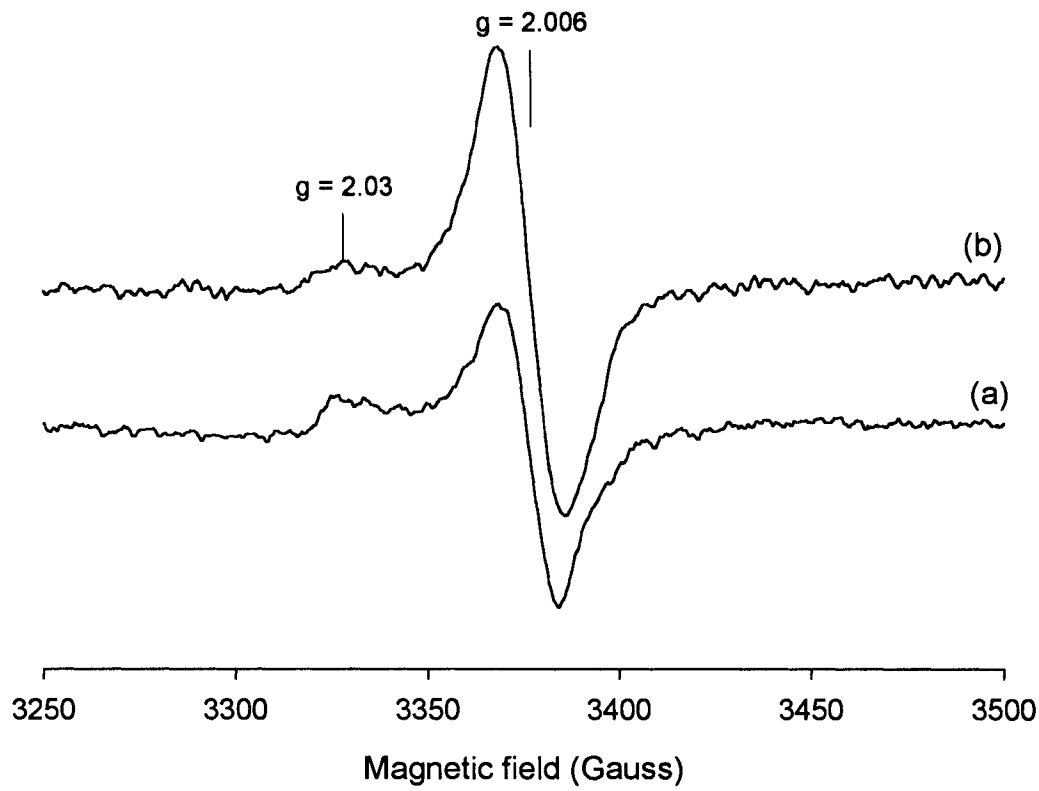

Figure 3.15 Rapid freeze-quench EPR spectra of WT-KatG in a repeat reaction with peroxyacetic acid. Rapid freeze-quench EPR samples were prepared from a previously reacted WT KatG sample mixed with 10-fold excess peroxyacetic acid and stored for one hour at 4 °C. The enzyme was then exchanged into phosphate buffer. Samples were frozen 250 ms (a), or 5 s (b) after mixing the pre-reacted enzyme (50 μM final) with PAA (150 μM final) in 20mM potassium phosphate buffer at 25 ° C. EPR conditions were as in Figure 3.13.

Reproduced with permission of the copyright owner. Further reproduction prohibited without permission.

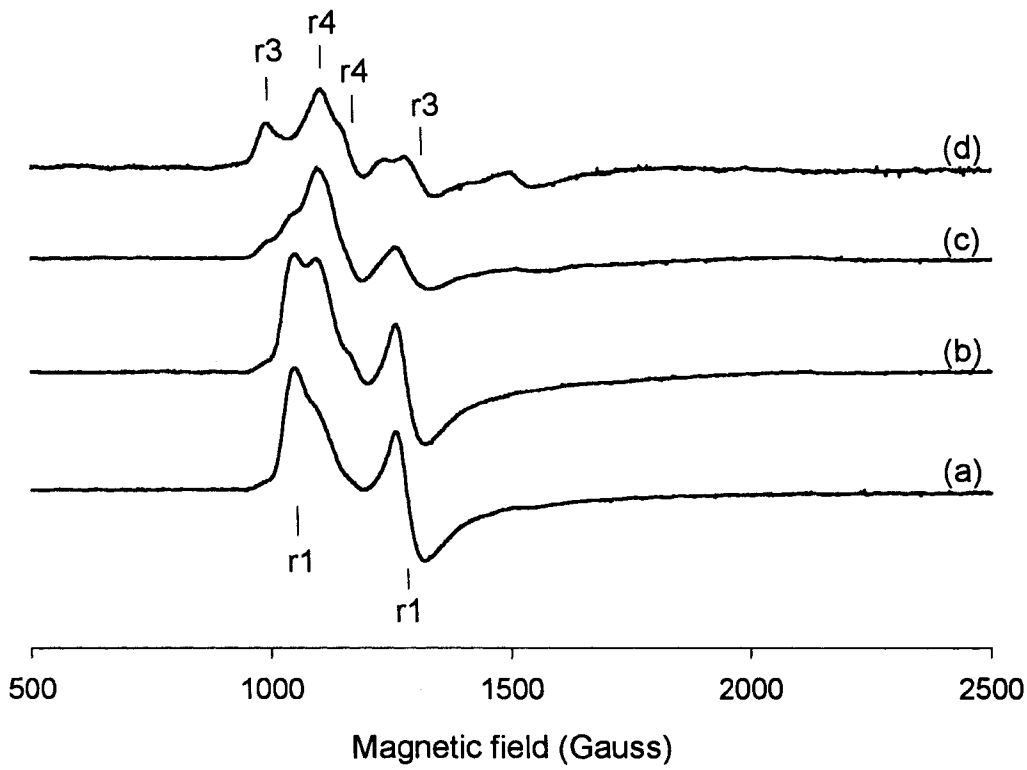

Figure 4.1 EPR spectra of KatG showing changes during purification and storage. (a) fresh partially-purified KatG, (b) pure KatG, and KatG after 3 (c) and 10 (d) weeks' storage. Experimental conditions were as follows: temperature, 5.5 K; microwave power, 5 mW; frequency 9.2446 GHz.

Reproduced with permission of the copyright owner. Further reproduction prohibited without permission.

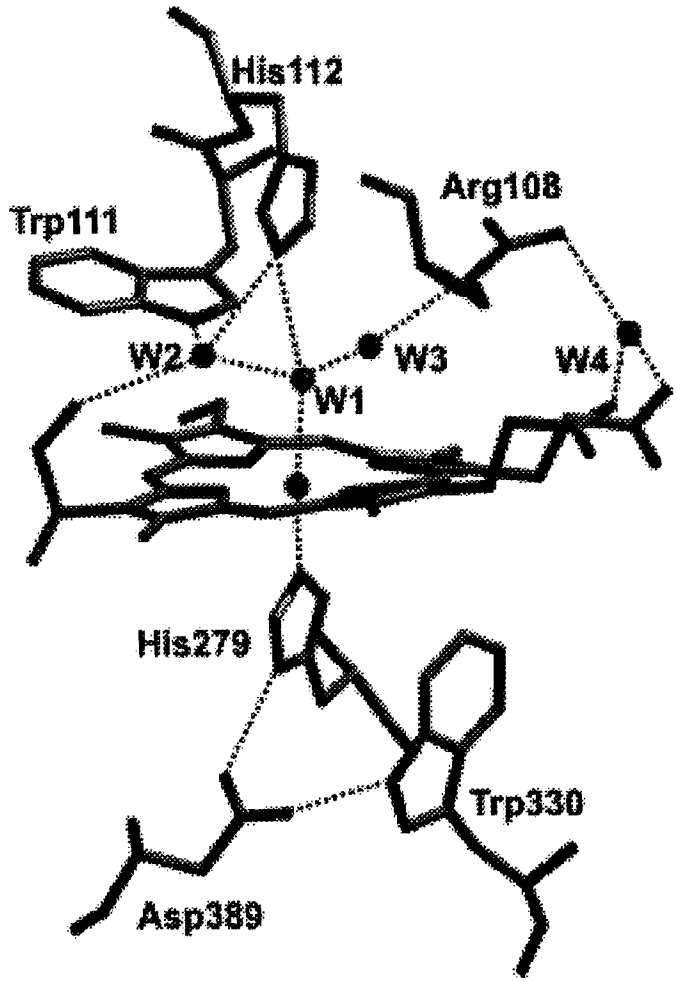

Figure 4.2 Active site of *B. pseudomallei* KatG showing a stereo view of the residues in the vicinity of the heme. On the distal side, four water molecules labeled W_1-W_4 are also shown. [Taken from (20)].

Reproduced with permission of the copyright owner. Further reproduction prohibited without permission.

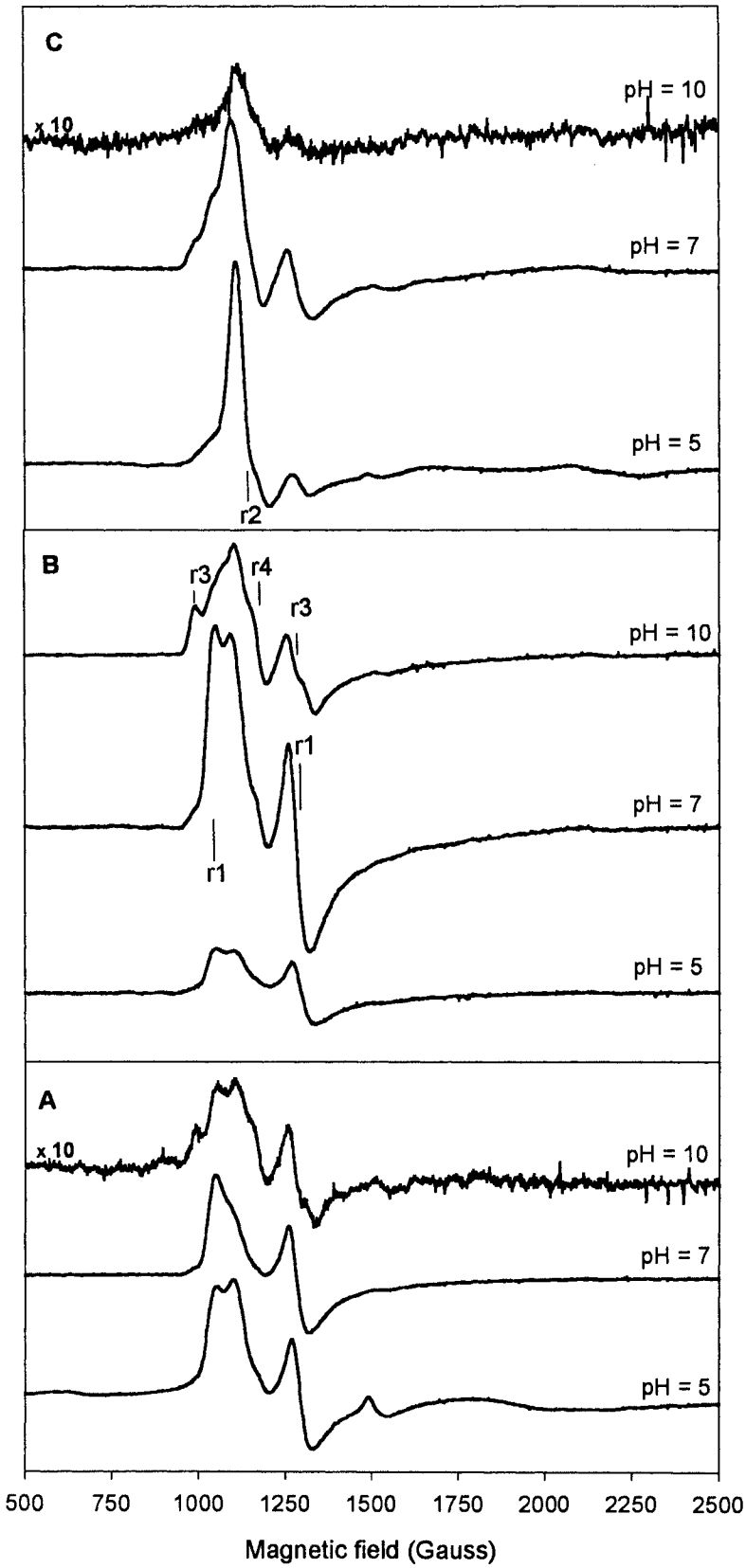

Reproduced with permission of the copyright owner. Further reproduction prohibited without permission.

Figure 4.3 pH dependence of EPR spectra of KatG. (panel A) fresh partially-purified KatG, (panel B) pure KatG, and (panel C) KatG after 3 weeks' storage. In citrate buffer, pH = 5; phosphate buffer, pH = 7; and carbonate buffer, pH = 10. Experimental conditions were the same as in Figure 4.1.

Reproduced with permission of the copyright owner. Further reproduction prohibited without permission.

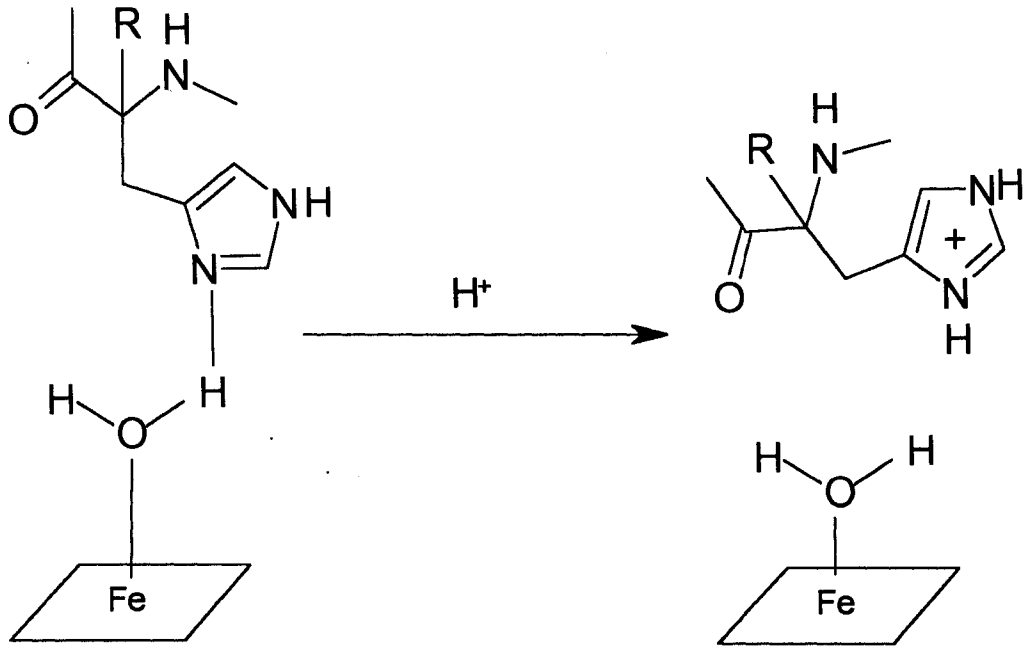

Figure 4.4 Proposed pH-dependent distal histidyl imidazole reorientation in ferric KatG.

Reproduced with permission of the copyright owner. Further reproduction prohibited without permission.

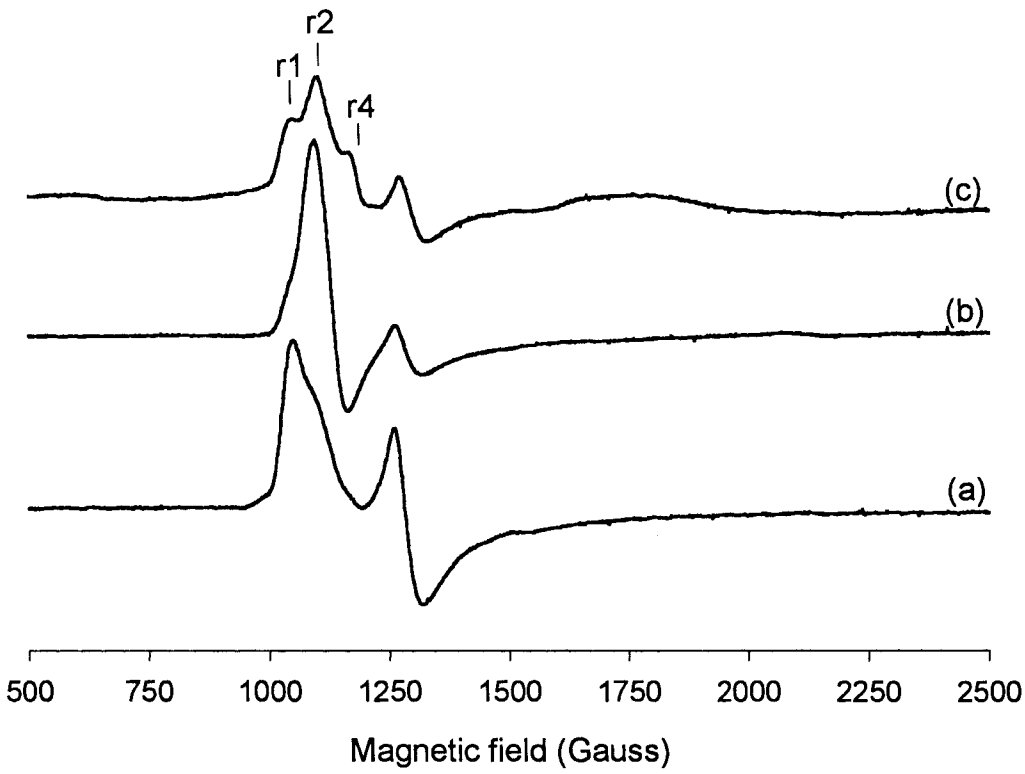

Figure 4.5 Fresh partially purified KatG in the presence of NaF or NaCl. (a) no additions, (b) in the presence of excess NaF and (c) in the presence of excess NaCl. Experimental conditions were the same as in Figure 4.1.

Reproduced with permission of the copyright owner. Further reproduction prohibited without permission.

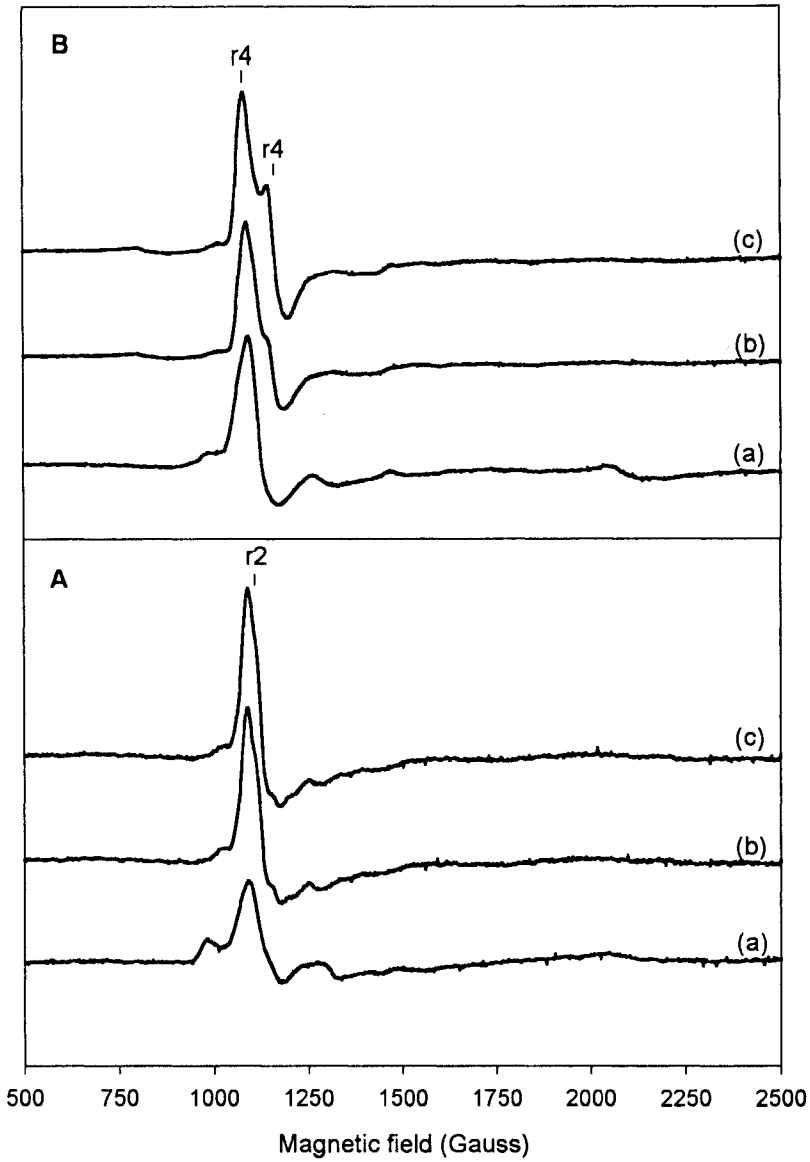

Figure 4.6 Effect of NaCl on KatG EPR spectra. The enzyme used here had been stored for one week prior to freezing EPR samples. (Panel A) EPR spectra of pure KatG (a), 1 hour after the addition of 1M NaCl (b) and 24 hours after the addition of 1M NaCl (c) all in potassium phosphate buffer (pH = 7). (Panel B) EPR spectra of pure KatG (a), 1 hour after the addition of 1M NaCl (b) and 24 hours after the addition of 1M NaCl (c) all in citrate buffer (pH = 5). Experimental conditions were the same as in Figure 4.1

Reproduced with permission of the copyright owner. Further reproduction prohibited without permission.

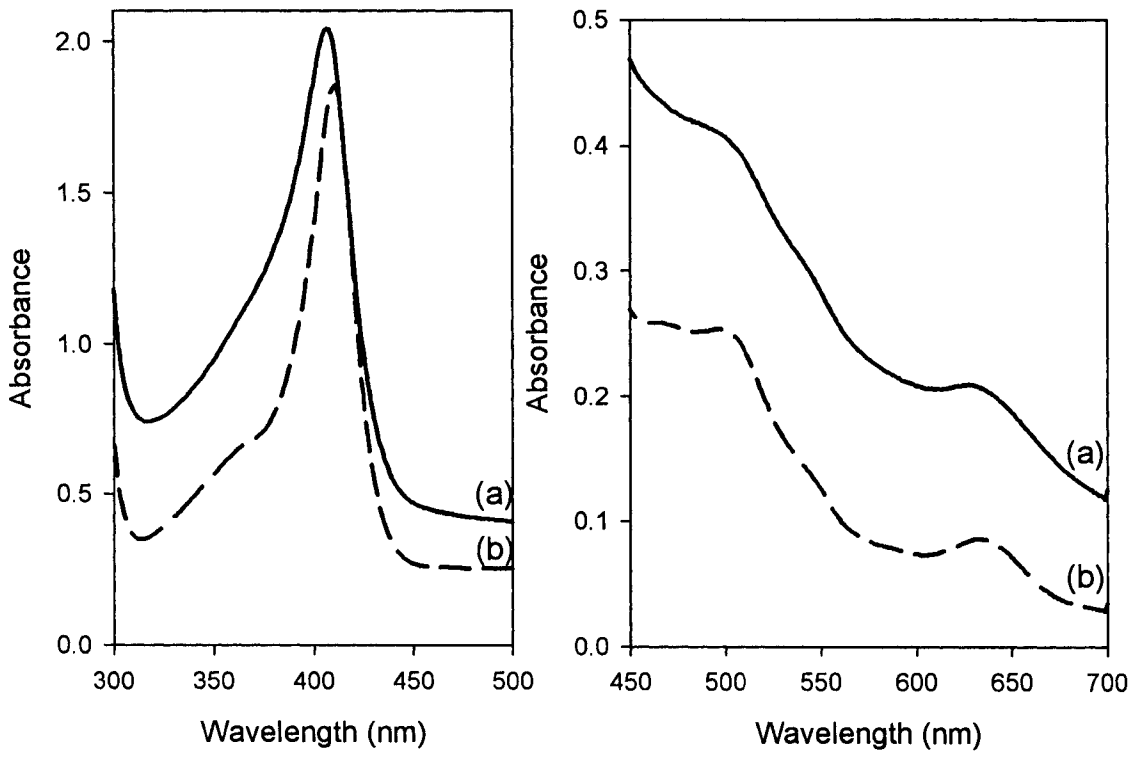

Figure 4.7 Effect of chloride on the optical spectrum of fully purified KatG at pH 5. The enzyme used here had been stored for three weeks. (a) no addition; (b) 24 hours after the addition of 1 M NaCl. Left panel: Soret region. Right panel: visible region. The spectra are offset for presentation purposes.

Reproduced with permission of the copyright owner. Further reproduction prohibited without permission.

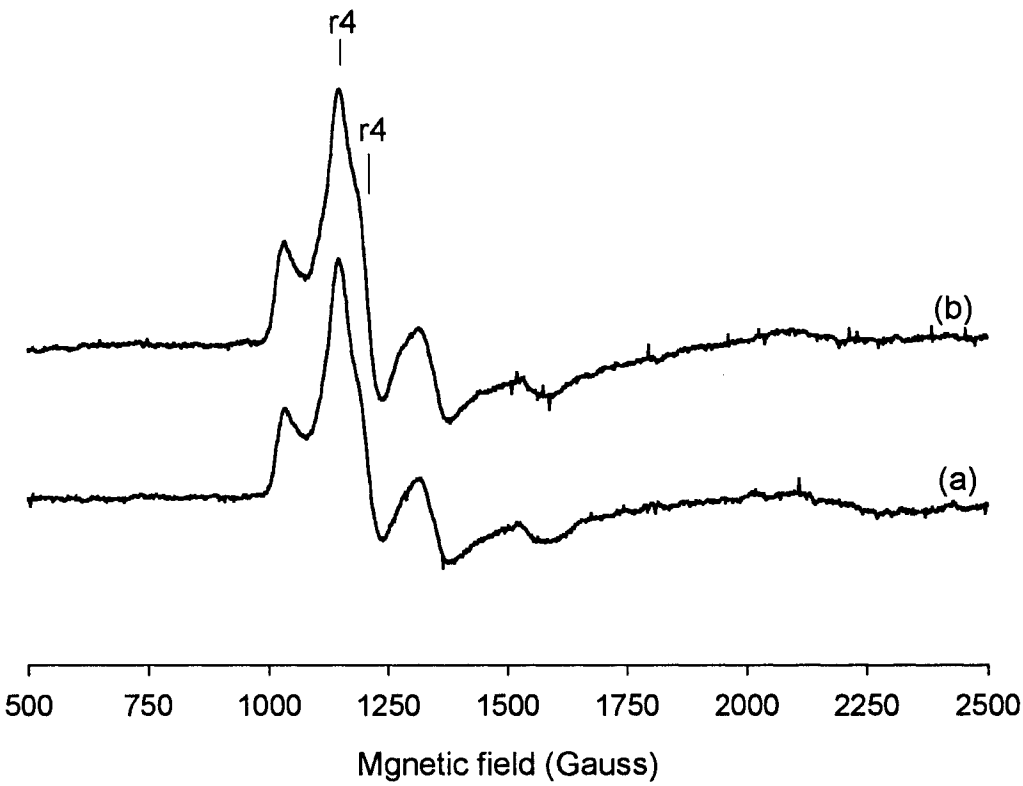

Figure 4.8 Effect of INH on EPR spectra of KatG. (a) no addition; (b) plus INH (6-fold excess over heme). The enzyme used here had been stored for 3 weeks prior to freezing for EPR samples. Experimental conditions were the same as in Figure 4.1.

Reproduced with permission of the copyright owner. Further reproduction prohibited without permission.

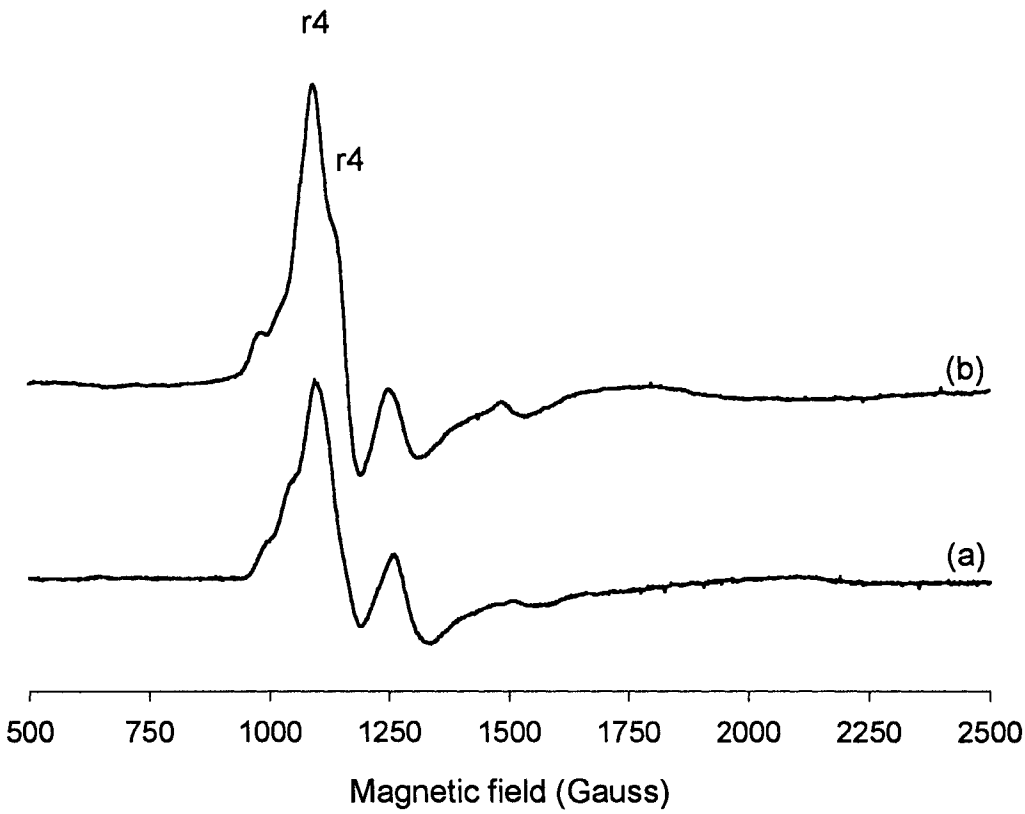

Figure 4.9 Effect of benzohydroxamic acid on EPR spectra of KatG. (a) no addition and (b) plus excess BHA. The enzyme used here had been stored for 1 week prior to freezing for EPR samples. Experimental conditions were the same as in Figure 4.1.

Reproduced with permission of the copyright owner. Further reproduction prohibited without permission.

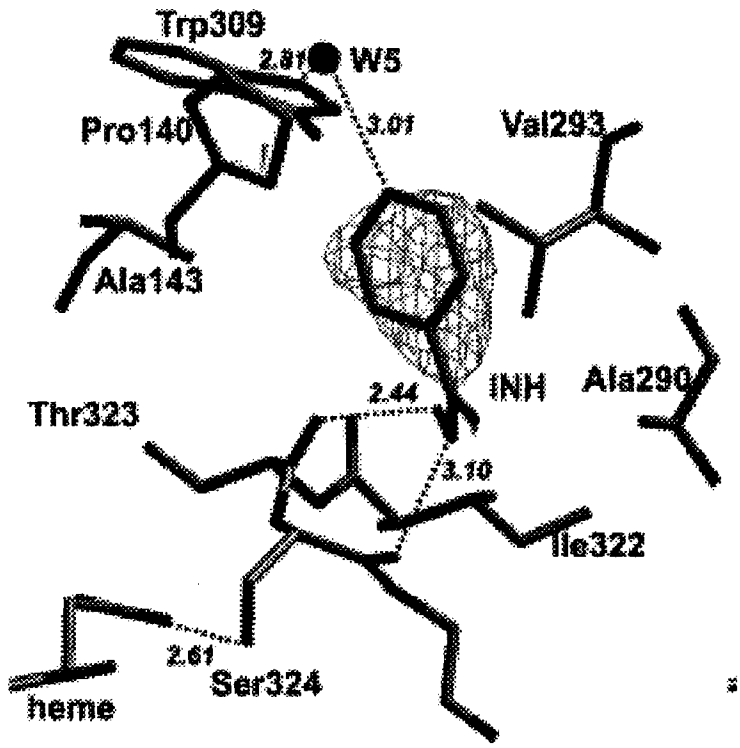

Figure 4.10 Proposed INH binding site in *B. pseudomallei* KatG. The electron density is shown with a model of isoniazid (INH) superimposed (20).

Reproduced with permission of the copyright owner. Further reproduction prohibited without permission.

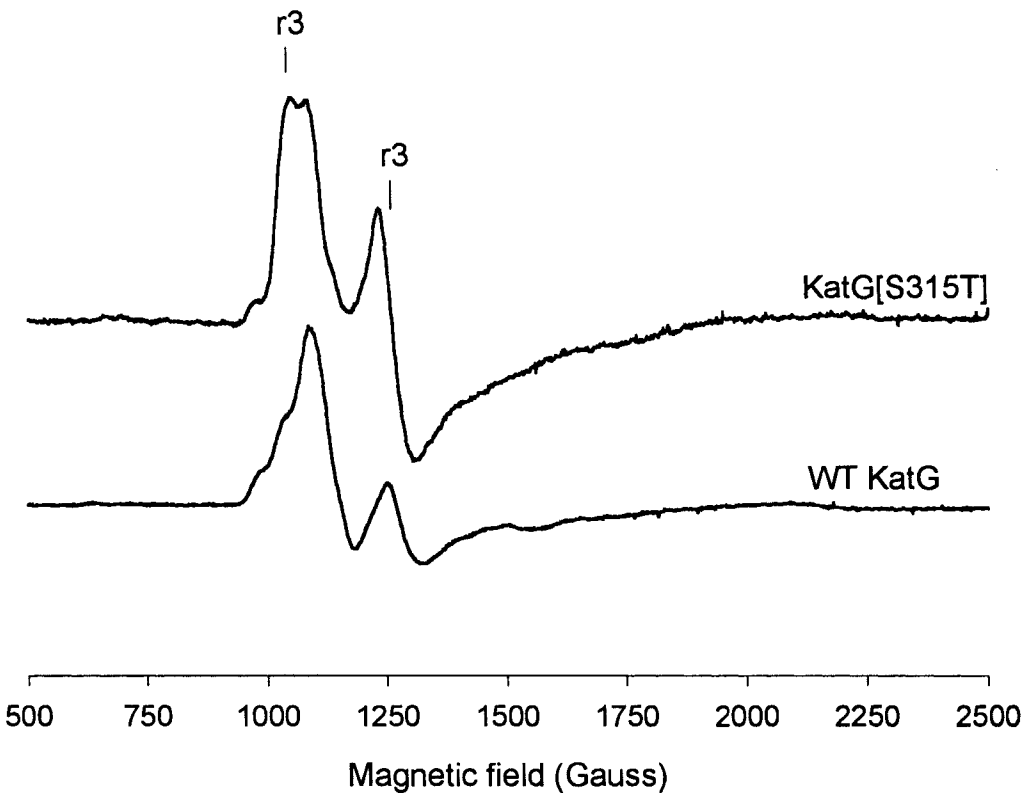

Figure 4.11 Low temperature EPR spectra of WT KatG and KatG[S315T] mutant.

The enzymes used here had been stored for 3 weeks prior to freezing for EPR.

Experimental conditions were the same as in Figure 4.1.

Reproduced with permission of the copyright owner. Further reproduction prohibited without permission.

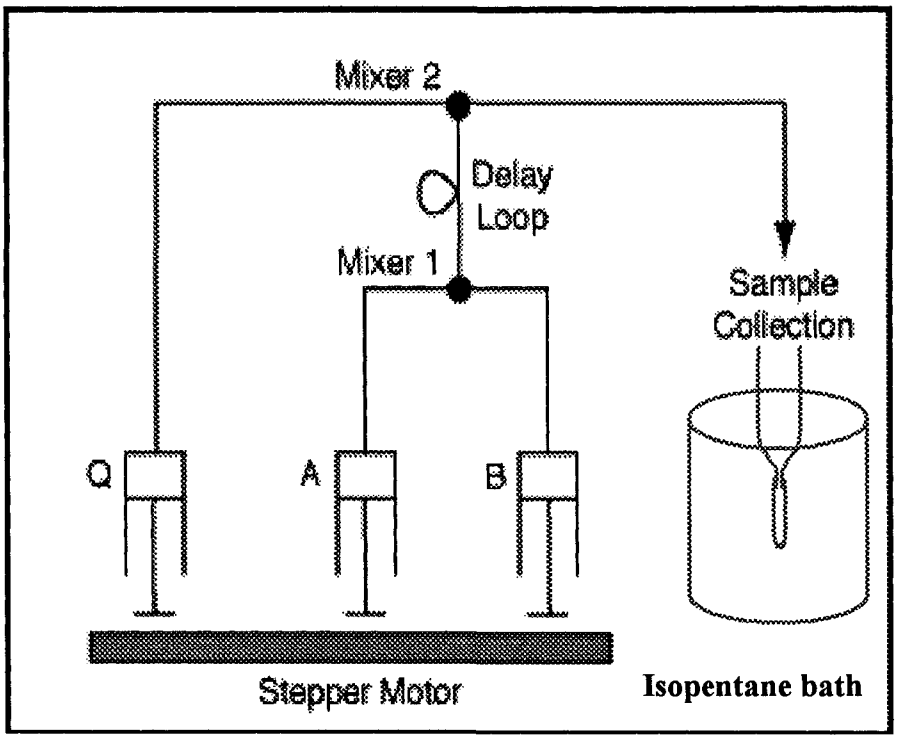

Figure A.1 Rapid freeze-quench EPR apparatus

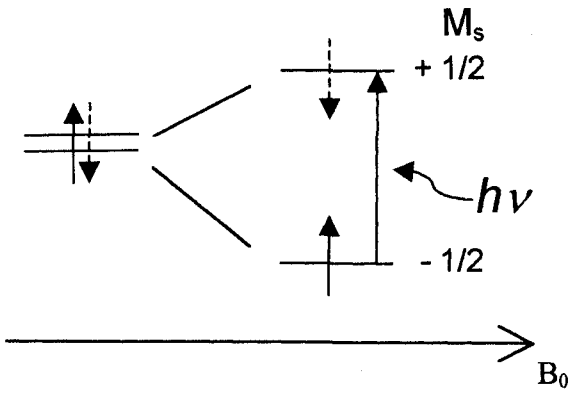

Figure B.1 Zeeman splitting for an S = ½ system. The $\Delta Ms = \pm 1$ transition is shown.

Reproduced with permission of the copyright owner. Further reproduction prohibited without permission.

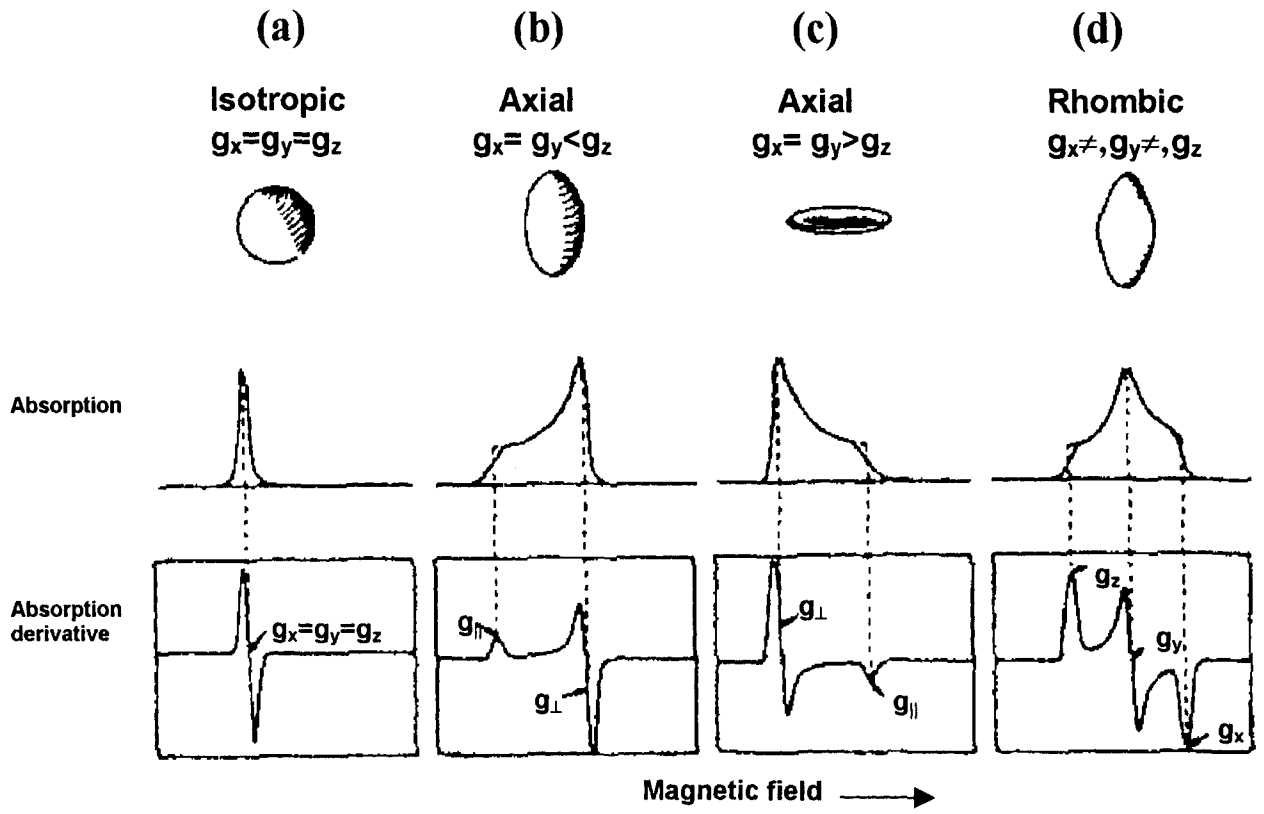

Figure B.2 Schematic representation of g-tensors and the corresponding EPR spectra. The figures illustrate isotropic (a), axial (prolate and oblate) (b, c) and rhombic (d) magnetic moments. The absorption curves and the corresponding EPR derivative curves are also shown (102).

Reproduced with permission of the copyright owner. Further reproduction prohibited without permission.

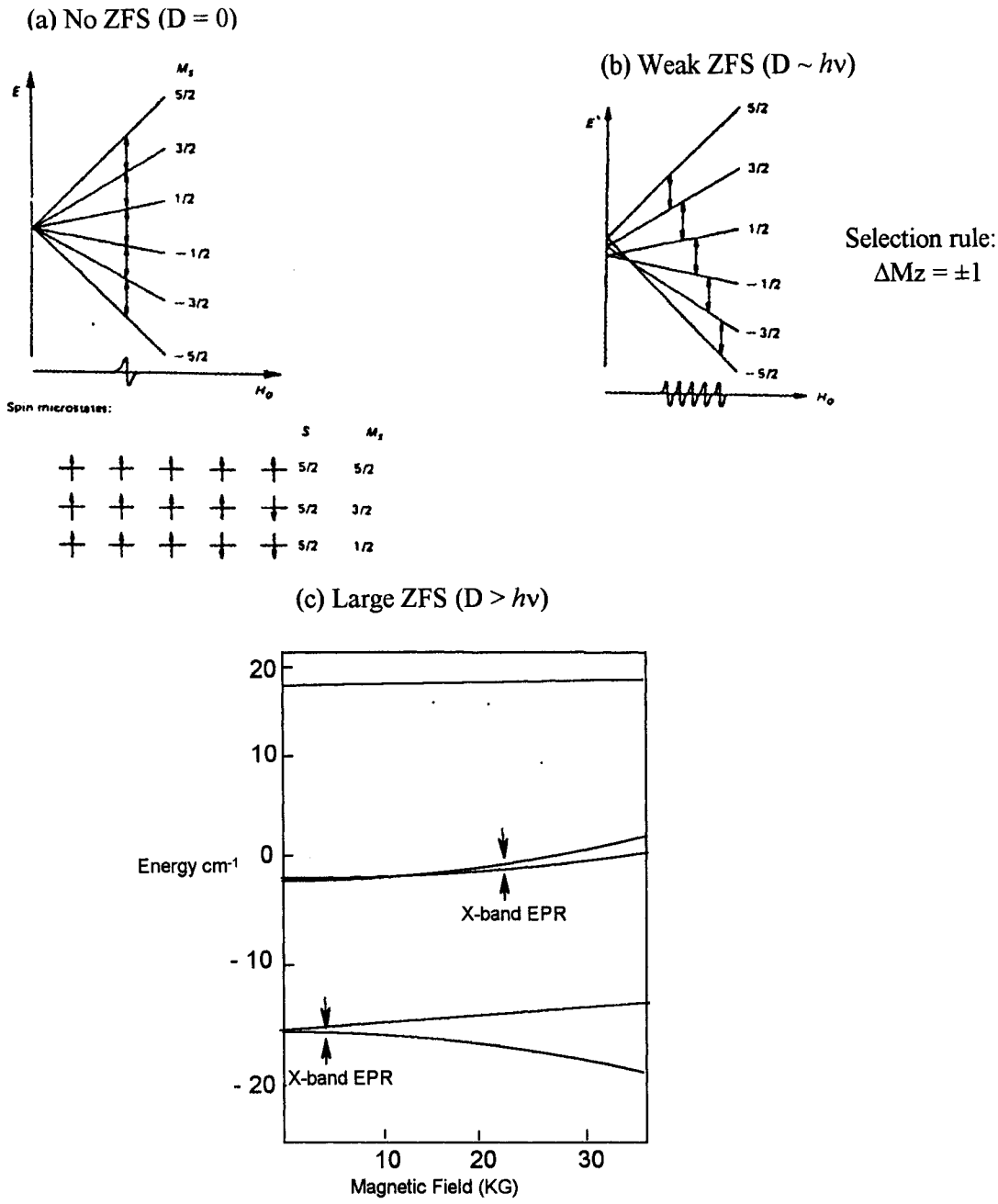

Figure B.3 Energy levels and EPR of S = 5/2 with varying degrees of zero-field splitting (ZFS). In the absence of ZFS (D = 0) a single isotropic EPR line is observed (a). With a small splitting, five lines are centered at g = 2 (b) (102). In (c) the zero-field splitting is large, and a highly anisotropic signal is observed from the lowest (M_s = ½) component shown here for axial high spin ferric heme at X-band in the condition where the magnetic field is parallel to the heme equatorial plane (116).

Reproduced with permission of the copyright owner. Further reproduction prohibited without permission.

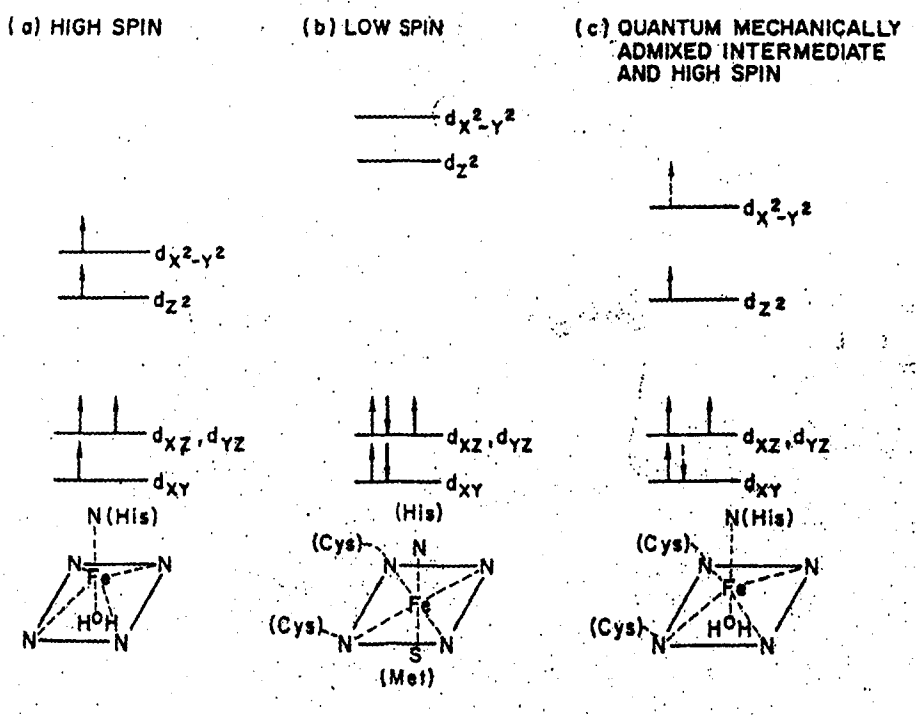

Figure B.4 Ordering of d orbitals and the corresponding heme structures proposed for ferricytochrome c'. (a) a typical ferric high spin state; (b) a typical ferric low spin state; and (c) as proposed by M. M. Maltempo for the spin admixed state (QS) (89).

Reproduced with permission of the copyright owner. Further reproduction prohibited without permission.

Table 2.1 EPR parameters used for simulation of tyrosyl radical EPR spectra[a].

Parameters	Doublet signal			Singlet signal		
$g_{(x, y, z)}$	20087	20044	20023	2.0074	2.0044	2.0023
$A_{(xx, yy, zz)}$ MHz (β-methylene proton)	47.5	47.5	50.0	34.0	34.0	37.0
$A_{(xx, yy, zz)}$ MHz (3, 5-ring protons)	23.7	7.4	19.5	26.0	7.8	20.9

[a]Spectra and simulations are shown in Figure 2.4. The g-tensor values as well as the week proton hyperfine couplings were based on published values for the tyrosyl radical in PGHS (51).

Table 4.1 g values for ferric heme iron species found in *M. tuberculosis* KatG.

signal	EPR g values	spin state
r_1	$g_1 = 6.3$; $g_2 = 5.14$; $g_3 \sim 2$	5-c HS
r_2	$g_\perp = 5.8$; $g_\parallel \sim 2$	6-c HS
r_3	$g_1 = 6.6$; $g_2 = 5.0$; $g_3 \sim 2$	5-c HS
r_4	$g_1 = 6.04$; $g_2 = 5.6$; $g_3 \sim 2$	6-c QS

Reproduced with permission of the copyright owner. Further reproduction prohibited without permission.

Bibliography

1. "Tuberculosis". WHO Information Sheet 104; http://www.who.int/inf-fs/en/fact104.html; accessed December, 2003.

2. Rouhi, A.M. Tuberculosis: A Tough Adversary. *C&EN* 77, 52-72 (1999).

3. Young, D.B. Blueprint for the White Plague. *Nature* 393, 515-516 (1998).

4. Johnsson, K. & Schultz, P.G. Mechanistic studies of the oxidation of isoniazid by the catalase-peroxidase from *Mycobacterium tuberculosis*. *J. Am. Chem. Soc.* 116, 7425-7426 (1994).

5. Johnsson, K., King, D.S. & Schultz, P.G. Studies on the mechanism of action of isoniazid and ethionamide in the chemotherapy of tuberculosis. *J. Am. Chem. Soc.* 117, 5009-5010 (1995).

6. Zhang, Y., Heym, B., Allen, B., Young, D. & Cole, S. The catalase-peroxidase gene and isoniazid resistance of *Mycobacterium tuberculosis*. *Nature* 358, 591-593 (1992).

7. Dunford, H.B. *Heme Peroxidases*, (Wiley-VCH, New York, 1999).

8. Pym, A.S. et al. Regulation of catalase-peroxidase (KatG) expression, isoniazid sensitivity and virulence by furA of Mycobacterium tuberculosis. *Mol. Microbiol.* 40, 879-889 (2001).

9. Collins, D.M. In search of tuberculosis virulence genes. *Trends Microbiol.* 4, 426-430 (1996).

10. Welinder, K.G. Bacterial catalase-peroxidases are gene duplicated members of the plant peroxidase superfamily. *Biochim Biophys Acta* 1080, 215-20 (1991).

11. Chouchane, S., Lippai, I. & Magliozzo, R.S. Catalase-peroxidase (*Mycobacterium tuberculosis* KatG) catalysis and isoniazid activation. *Biochemistry* 39, 9975-9983 (2000).

12. Ornstein, G.G., Robitzek, E.H. & Selikoff, I.J. Clinical studies: treatment of tuberculosis with isonicotinic acid hydrazine and its derivatives. *Trans. Annu. Meet. Natl. Tuberc. Assoc.* 48, 433-438 (1952).

13. Zhang, Y., Garbe, T. & Young, D. Transformation with katG restores isoniazid-sensitivity in *Mycobacterium tuberculosis* isolates resistant to a range of drug concentrations. *Mol. Microbiol.* 8, 521-524 (1993).

Reproduced with permission of the copyright owner. Further reproduction prohibited without permission.

14. Banerjee, A. et al. inhA, a gene encoding a target for isoniazid and ethionamide in *Mycobacterium tuberculosis*. *Science* 263, 227-230 (1994).

15. Basso, L.A., Zheng, R. & Blanchard, S. Kinetics of Inactivation of WT and C243S Mutant of *Mycobacterium tuberculosis* Enoyl Reductase by Activated Isoniazid. *J. Am. Chem. Soc.* 118, 11301-11302 (1996).

16. Quemard, A. et al. Enzymatic characterization of the target for isoniazid in *Mycobacterium tuberculosis*. *Biochemistry* 34, 8235-41 (1995).

17. Quemard, A. et al. Binding of Catalase-Peroxidase-Activated Isoniazid to Wild-Type and Mutant *Mycobacterium tuberculosis* Enoyl-ACP Reductases. *J. Am. Chem. Soc.* 118, 1561-1562 (1996).

18. Todar, K. Textbook of Bacteriology http://textbookofbacteriology.net/tuberculosis.html, accessed January 10, 2004.

19. Yamada, Y., Fujiwara, T., Sato, T., Igarashi, N. & Tanaka, N. The 2.0 Å crystal structure of catalase-peroxidase from *Haloarcula marismortui*. *Nature Structural Biology* 9, 691-695 (2002).

20. Carpena, X. et al. Catalase-peroxidase KatG of *Burkholderia pseudomallei* at 1.7 Å resolution. *J. Mol. Biol.* 327, 475-489 (2003).

21. Funk, C.D., Funk, L.B., Kennedy, M.E., Pong, A.S. & Fitzgerald, G.A. Human platelet/erythroleukemia cell prostaglandin G/H synthase: cDNA cloning, expression, and gene chromosomal assignment. *FASEB J.* 5, 2304-2312 (1991).

22. Kosaka, T. et al. Characterization of the human gene (PTGS2) encoding prostaglandin- endoperoxide synthase 2. *Eur. J. Biochem.* 221, 889-897 (1994).

23. Zamocky, M., Regelsberger, G., Jakopitsch, C. & Obinger, C. The molecular peculiarities of catalase-peroxidases. *FEBS Lett.* 492, 177-182 (2001).

24. Ricard, J. & Nari, J. The formation and reactivity of peroxidase compound 3. *Biochim. Biophys. Acta*, 132, 321-329 (1967).

25. Wengenack, N.L., Hoard, H.M. & Rusnak, F. Isoniazid Oxidation by *Mycobacterium tuberculosis* KatG: A Role for Superoxide Which Correlates with Isoniazid Susceptibility. *J. Am. Chem. Soc.* 121, 9748-9749 (1999).

26. Wengenack, N.L. & Rusnak, F. Evidence for Isoniazid-Dependent Free Radical Generation Catalyzed by *Mycobacterium tuberculosis* KatG and the Isoniazid-Resistant Mutant KatG(S315T). *Biochemistry* 40, 8990-8996 (2001).

Reproduced with permission of the copyright owner. Further reproduction prohibited without permission.

27. Magliozzo, R.S., and Marcinkeviciene, J.A. Evidence for isoniazid oxidationi by oxyferrous mycobacterial catalase-peroxidase. *J. Am. Chem. Soc.* 118, 11303-11304 (1996).

28. Chouchane, S., Girotto, S., Yu, S. & Magliozzo, R.S. Identification and characterization of tyrosyl radical formation in *Micobacterium tuberculosis* catalase-peroxidase (KatG). *J. Biol. Chem.* 277, 42633-38 (2002).

29. Sinha, B.K. Enzymatic activation of hydrazine derivatives. A spin-trapping study. *J. Biol. Chem.* 258, 796-801 (1983).

30. Shoeb, H.A., Bowman, B.U.J., Ottolenghi, A.C. & Merola, A.J. Peroxidase-mediated oxidation of isoniazid. *Antimicrob. Agents Chemother.* 27, 399-403 (1985).

31. Wengenack, N.L., Todorovic, S., Yu, L. & Rusnak, F. Evidence for differential binding of isoniazid by *Mycobacterium tuberculosis* KatG and the isoniazid-resistant mutant KatG(S315T). *Biochemistry* 37, 15825-15834 (1998).

32. Chouchane, S. et al. Analysis of heme structural heterogeneity in *Mycobacterium tuberculosis* catalase-peroxidase (KatG). *J. Biol. Chem.* 278, 8154-62 (2003).

33. Yu, S., Girotto, S., Lee, C. & Magliozzo, R.S. Reduced affinity for isoniazid in the S315T mutant of *Mycobacterium tuberculosis* KatG is a key factor in antibiotic resistance. *J. Bio. Chem.* 278, 14769-14775 (2003).

34. Sjoberg, B.M., Reichard, P., Graslund, A. & Ehrenberg, A. Nature of the free radical in ribonucleotide reductase from *Escherichia coli*. *J. Biol. Chem.* 252, 536-541 (1977).

35. Unkrig, V., Neugebauer, F.A. & Knappe, J. The free radical of pyruvate formate-lyase. Characterization by EPR spectroscopy and involvement in catalysis as studied with the substrate- analogue hypophosphite. *Eur. J. Biochem.* 184, 723-728 (1989).

36. Licht, S., Gerfen, G.J. & Stubbe, J. Thiyl radicals in ribonucleotide reductases. *Science* 271, 477-481 (1996).

37. Nordlund, P., Sjoberg, B.-M. & Eklund, H. Three-dimensional structure of the free radical protein of ribonucleotide reductase. *Nature* 345, 593-598 (1990).

38. Finzel, B.C., Poulos, T.L. & Kraut, J. Crystal structure of yeast cytochrome *c* peroxidase at 1.7 Å level. *J. Biol. Chem.* 259, 13027-13036 (1984).

39. Stubbe, J. & van der Donk, W.A. Protein Radical in Enzyme Catalysis. *Chem. Rev.*, 705-762 (1998).

Reproduced with permission of the copyright owner. Further reproduction prohibited without permission.

40. Ehrenberg, A. & Reichard, P.J. Electron Spin Resonance of the Iron-containing protein B2 from Ribonucleotide reducatase. *J. Biol. Chem.* 247, 3485-3488 (1972).

41. Tsai, A.L., Palmer, G. & Kulmacz, R.J. Prostaglandin H synthase. Kinetics of tyrosyl radical formation and of cyclooxygenase catalysis. *J. Biol. Chem.* 267, 17753-17759 (1992).

42. Tsai, A., Kulmacz, R.J. & Palmer, G. Spectroscopic evidence for reaction of prostaglandin H synthase-1 tyrosyl radical with arachidonic acid. *J. Biol. Chem.* 270, 10503-10508 (1995).

43. Tang, X.-S., Randall, D.W., Force, D.A., Diner, B.A. & Britt, R.D. Manganese-Tyrosine Interaction in the Photosystem II Oxygen-Evolving Complex. *J. Am. Chem. Soc.* 118, 7638-7639 (1996).

44. Summers, F.E. & Erman, J.E. Reduction of cytochrome c peroxidase Compounds I and II by ferrocytochrome c. A stopped-flow kinetic investigation. *J. Biol. Chem.* 263, 14267-14275 (1988).

45. Ivancich, A., Jouve, H.M., Sartor, B. & Gaillard, J. EPR investigation of Compound I in *Proteus mirabilis* and Bovine Liver Catalases: Formation of Porphyrin and Tyrosyl Radical Intermediates. *Biochemistry* 36, 9356-9364 (1997).

46. Ivancich, A., Mazza, G. & Desbois, A. Comparative Electron Paramagnetic Resonance Study of Radical Intermediates in Turnip Peroxidase Isozymes. *Biochemistry* 40, 6860-6866 (2001).

47. Warncke, K. & Perry, M.S. Redox state dependence of rotamer distributions in tyrosine and neutral tyrosyl radical. *Biochim. Biophys. Acta* 1545, 1-5 (2001).

48. Babcock, G.T. et al. Tyrosyl radicals in enzyme catalysis: some properties and a focus on photosynthetic water oxidation. *Acta Chem Scand* 51, 533-40 (1997).

49. Neese, F. Ph. D. thesis. University of Konstanz (1995).

50. Neese, F. in *Quantum Chemistry Program Exchange* Vol. Bull. 15 (5) (University of Indiana: Bloomington, IN, 1995).

51. Shi, W. et al. Electron paramagnetic resonance and electron nuclear double resonance spectroscopic identification and characterization of the tyrosyl radicals in prostaglandin H synthase 1. *Biochemistry* 39, 4112-4121 (2000).

Reproduced with permission of the copyright owner. Further reproduction prohibited without permission.

52. Rigby, S.E.J., Nungent, J.H.A. & O'Malley, P.J. The dark stable tyrosine radical of photosystem 2 studied in three species using ENDOR and EPR spectroscopies. *Biochemistry* 33, 1734-1742 (1994).

53. O'Malley, P.J., MacFarlane, A.J., Rigby, S.E.J. & Nugent, J.H.A. The geometry and spin density distribution of the tyrosyl radical: a molecular orbital study. *Biochim. Biophys. Acta* 1232, 175-179 (1995).

54. Bender, C.J. et al. An ENDOR study of the tyrosyl free radical in ribonucleotide reductase from Escherichia coli. *J. Am. Chem. Soc.* 111, 8076-8083 (1989).

55. Lendzian, F. et al. Electronic Structure of Neutral Tryptophan Radicals in Ribonucleotide Reductase Studied by EPR and ENDOR Spectroscopy. *J. Am. Chem. Soc.* 118, 8111-8120 (1996).

56. Sjoberg, B.M., Reichard, P., Graslund, A. & Ehrenberg, A. The tyrosine free radical in ribonucleotide reductase from *Escherichia coli*. *J. Biol. Chem.* 253, 6863-6865 (1978).

57. Weil, J.A., Bolton, J.R. & Wertz, J.E. *Electron Paramagnetic Resonance. Elementary Theory and Practical Applications*, (John Wiley & Sons, INC., New York, 1994).

58. Langella, E., Improta, R. & Barone, V. Conformational and Spectroscopic Analysis of the Tyrosyl Radical Dipeptide Analogue in the Gas Phase and in Aqueous Solution by a Density Functional/Continuum Solvent Model. *J. Am. Chem. Soc.* 124, 11531-11540 (2002).

59. Gerfen, G.J. et al. High-Frequency (139.5 GHz) EPR Spectroscopy of the Tyrosyl Radical in *Escherchia coli* Ribonucleotide Reductase. *J. Am. Chem. Soc.* 115, 6420-6421 (1993).

60. Dorlet, P. et al. High-field EPR study of tyrosyl radicals in prostaglandin H(2) synthase-1. *Biochemistry* 41, 6107-6114 (2002).

61. Ivancich, A., Jakopitsch, C., M., A., Un, S. & Obinger, C. Protein-based Radicals in the Catalase-Peroxidase of Synechocystis PCC6803: A Multifrequency EPR Investigation of wild-type and variants on the environment of the heme active site. *J. Am. Chem. Soc.* 125, 14093-14102 (2003).

62. Bleifuss et al. Tryptophan and Tyrosine Radicals in Ribonucleotide Reductase: A comparative High-Field Study at 94 GHz. *Biochemistry*, 15362-15368 (2001).

63. Ivancich, A., Dorlet, P., Goodin, D.B. & Un, S. Multifrequency high-field EPR study of the tryptophanyl and tyrosyl radical intermediates in wild-type and the

Reproduced with permission of the copyright owner. Further reproduction prohibited without permission.

W191G mutant of cytochrome c peroxidase. *J. Am. Chem. Soc.* 123, 5050-5058 (2001).

64. Laidler, K.J. *Chemical Kinetics*, (Harper Collins Publisher, New York, 1987).

65. McCammon, J.A., Wolynes, P.G. & Karplus, M. Picosecond Dynamics of Tyrosine Side Chains in Proteins. *Biochemistry* 18, 927-942 (1979).

66. Nall, B.T. & Zuniga, E.H. Rates and Energetics of Tyrosine Ring Flips in Yeast Iso-2-cytochrome c. *Biochemistry* 29, 7576-7584 (1990).

67. Benecky, M.J., Frew, J.E., Scowen, N., Jones, P. & Hoffman, B.M. EPR and ENDOR detection of compound I from *Micrococcus lysodeikticus* catalase. *Biochemistry* 32, 11929-33 (1993).

68. Schulz, C.E. et al. Horseradish peroxidase compound I: evidence for spin coupling between the heme iron and a 'free' radical. *FEBS Lett.* 103, 102-105 (1979).

69. Shimokawa, T., Kulmacz, R.J., DeWitt, D.L. & Smith, W.L. Tyrosine 385 of prostaglandin endoperoxide synthase is required for cyclooxygenase catalysis. *J. Biol. Chem.* 265, 20073-6 (1990).

70. Jakopitsch, C., Kolarich, D., Petutschnig, G., Furtmuller, P.G. & Obinger, C. Distal side tryptophan, tyrosine and methionine in catalase-peroxidases are covalently linked in solution. *FEBS Lett.* 552, 135-140 (2003).

71. Tsai, A., Hsi, L.C., Kulmacz, R.J., Palmer, G. & Smith, W.L. Characterization of the tyrosyl radicals in ovine prostaglandin H synthase-1 by isotope replacement and site-directed mutagenesis. *J. Biol. Chem.* 269, 5085-5091 (1994).

72. Jakopitsch, C. et al. Total conversion of bifunctional catalase-peroxidase (KatG) to monofunctional peroxidase by exchange of a conserved distal side tyrosine. *J. Biol. Chem.* 278, 20185-20191 (2003).

73. Nakajima, R. & Yamazaki, I. The mechanism of oxyperoxidase formation from ferryl peroxidase and hydrogen peroxide. *J. Biol. Chem.* 262, 2576-2581 (1987).

74. Donald, L.J. et al. Characterization of the Catalase-Peroxidase KatG from *Burkholderia pseudomallei* by Mass Spectrometry. *J. Biol.Chem.* 278, 35687-35692 (2003).

75. Yu, S., Girotto, S., Zhao, X. & Magliozzo, R.S. Rapid formation of Compound II and a tyrosyl radical in the Y229F mutant of *M. tuberculosis* KatG disrupts catalase but not peroxidase function. *J. Biol. Chem.* 278, 44121-44127 (2003).

Reproduced with permission of the copyright owner. Further reproduction prohibited without permission.

76. Zhao, X., Girotto, S., Yu, S. & Magliozzo, R.S. Evidence for radical formation at Tyr353 in *M. tuberculosis* catalase-peroxidase (KatG). *J. Biol. Chem.* in press (2003).

77. Lardinois, O.M., Medzihradszky, K.F. & Ortiz de Montellano, P.R. Spin trapping and protein cross-linking of the lactoperoxidase protein radical. *J Biol Chem* 274, 35441-8 (1999).

78. Peisach, J., Mims, W.B. & Davis, J.L. Water coordination by heme iron in metmyoglobin. *J. Biol. Chem.* 259, 2704-2706 (1984).

79. Khindaria, A. & Aust, S.D. EPR Detection and Characterizatrion of Lignin Peroxidase Porphyrin π-Cation Radical. *Biochemistry* 35, 13107-13111 (1996).

80. Blumberg, W.E. & Peisach, J. A unified theory for low spin forms of all ferric heme proteins as studied by EPR. *Probes of structure and function of macromolecules and membranes* 2, 215-229 (1971).

81. Loew, G. & Dupuis, M. Characterization of a Resting State Model of Peroxidases by *ab initio* Methods: Optimazed Geometries, Electronic Structures, and Relative Energies of the Sextet, Quartet, and Doublet Spin States. *J. Am. Chem. Soc.* 119, 9848-9851 (1997).

82. Itakura, H., Oda, Y. & Fukuyama, K. Biding mode of benzhydroxamic acid to *Arthromyces ramosus* peroxidase shown by X-ray crystallographic analysis of the complex at 1.6 Å resolution. *FEBS. Lett.* 412, 107-110 (1997).

83. Prasad, S., Mazumdar, S. & Mitra, S. Binding of camphor to *Pseudomonas putida* cytochrome $P450_{cam}$: steady state and picosecond time-resolved fluorescence studies. *FEBS Lett.* 477, 157-160 (2000).

84. Lukat-Rodgers, G.S., Wengenack, N.L., Rusnak, F. & Rodgers, K.R. Spectroscopic comparison of the heme active sites in WT KatG and its S315T mutant. *Biochemistry* 39, 9984-9993 (2000).

85. Ikeda-Saito, M. et al. Coordination structure of the ferric heme iron in engineered distal histidine myoglobin mutants. *J. Biol. Chem.* 267, 22843-22852 (1992).

86. Indiani, C., Feis, A., Howes, B.D., Marzocchi, M.P. & Smulevich, G. Benzohydroxamic Acid-Peroxidase Complexes: Spectroscopic Characterization of a Novel Heme Spin Species. *J. Am. Chem. Soc.* 122, 7368-7376 (2000).

87. Kapetanaki, S. et al. Conformational differences in Mycobacterium tuberculosis catalase-peroxidase KatG and its S315T mutant revealed by resonance Raman spectroscopy. *Biochemistry* 42, 3835-45 (2003).

Reproduced with permission of the copyright owner. Further reproduction prohibited without permission.

88. Howes, B.D. et al. The quantum mixed-spin heme state of barley peroxidase: A paradigm for class III peroxidases. *Biophys. J.* 77, 478-492 (1999).

89. Maltempo, M.M. Magnetic state of an unusual bacterial heme protein. *J. Chem. Phys.* 61, 2540-2547 (1974).

90. Howes, B.D., Schiodt, C.B., Welinder, K.G., Marzocchi,M.P., Ma, J-G., Zhang, J., Shelnutt, J.A., Smulevich, G. The quantum mixed-spin heme state of barley peroxidase: a paradigm for class III peroxidases. *Biophys. J.* 77, 478-492 (1999).

91. Yonetani, T. & Anni, H. Yeast cytochrome c peroxidase. Coordination and spin states of heme prosthetic group. *J. Biol. Chem.* 262, 9547-9554 (1987).

92. Dunford, H.B. & Alberty, R.A. The kinetics of fluoride binding by ferric horse radish peroxidase. *Biochemistry* 6, 447-51 (1967).

93. Ellis, W.D. & Dunford, H.B. The kinetics of cyanide and fluoride binding by ferric horseradish peroxidase. *Biochemistry* 7, 2054-2062 (1968).

94. Neri, F., Kok, D., Miller, M.A. & Smulevich, G. Fluoride binding in hemoproteins: the importance of the distal cavity structure. *Biochemistry* 36, 8947-8953 (1997).

95. Smulevich, G., Miller, M.A., Kraut, J. & Spiro, T.G. Conformational change and histidine control of heme chemistry in cytochrome c peroxidase: resonance Raman evidence from Leu-52 and Gly- 181 mutants of cytochrome c peroxidase. *Biochemistry* 30, 9546-58 (1991).

96. Magliozzo, R.S. & Peisach, J. Evaluation of nitrogen nuclear hyperfine and quadrupole coupling parameters for the proximal imidazole in myoglobin-azide, -cyanide, and -mercaptoethanol complexes by electron spin echo envelope modulation spectroscopy. *Biochemistry* 32, 8446-8456 (1993).

97. Sarma, S., DiGate, R.J., Goodin, D.B., Miller, C.J. & Guiles, R.D. Effect of Axial Ligand Plane Reorientation on the Electronic and Electrochemical Properties Observed in the A67V Mutant of Rat Cytochrome b5. *Biochemistry* 36, 5658-5668 (1997).

98. Marcinkeviciene, J.A., Magliozzo, R.S. & Blanchard, J.S. Purification and characterization of the Mycobacterium smegmatis catalase-peroxidase involved in isoniazid activation. *J. Biol. Chem.* 270, 22290-22295 (1995).

99. Beers, R.F. & Sizers, I.W. A spectrophotometric method for measuring the breakdown of hydrogen peroxide by catalase. *J. Biol. Chem.* 195, 133-140 (1952).

Reproduced with permission of the copyright owner. Further reproduction prohibited without permission.

100. Yu, S., Chouchane, S. & Magliozzo, R.S. Characterization of the W321F mutant of Mycobacterium tuberculosis catalase-peroxidase KatG. *Protein Sci.* 11, 58-64 (2002).

101. Sanger, F., Nicklen, S. & Coulson, A.R. DNA sequencing with chain-terminating inhibitors. *Proc Natl Acad Sci U S A* 74, 5463-5467 (1977).

102. Palmer, G. The electron paramagnetic resonance of metalloproteins. *Biochem. Soc. Trans.*, 548-560 (1985).

103. Smith, K.M. *Porphyrins and metalloporphyrins*, (Elsevier, 1976).

104. Rutter, R. et al. Chloroperoxidase compound I: Electron paramagnetic resonance and Mossbauer studies. *Biochemistry* 23, 6809-16 (1984).

105. Reed, C.A. et al. The Missing Heme Spin State and a Model for Cytochrome c'. The Mixed S = 3/2, 5/2 Intermediate Spin Ferric Porphyrin: Perchlorato(meso-tetraphenylporphinato)iron(III). *J. Am. Chem. Soc.* 101, 2948-2958 (1979).

106. Simonato, J.-P. et al. An Itegrated Approach to the Mid-Spin State (S= 3/2) in Six-Coordinate Iron (III) Chiroporphyrins. *Inorg. Chem.* 39, 3978-3987 (2000).

107. Cheng, R.-J., Chen, P.-Y., Gau, P.-R., Chen, C.-C. & Peng, S.-M. Control of Spin State by Ring Conformation of Iron(III) Porphyrins. A Novel Model for the Quantum-Mixed Intermediate Spin State of Ferric Cytochrome *c'* from Photosynthetic Bacteria. *J. Am. Chem. Soc* 119, 2563-2569 (1997).

108. Saito, M. & Kashiwagi, H. Ab initio MO study on relationships between the electronic state and out-of-plane displacement of the iron atom in four-coordinate Fe-porphine. *J. Chem. Phys.* 82, 848-855 (1985).

109. Fujii, S. et al. Electron paramagnetic resonance studies of ferric cytochrome c' from photosynthetic bacteria. *Biochim. Biophys. Acta* 1251, 161-169 (1995).

110. Indiani, C., Feis., A., Howes, B.D., Marzocchi, M.P., Smulevich,G. Effect of low temperature on soybean peroxidase: spectroscopic characterization of the quantum-mechanically admixed spin state. *J. Inorg. Biochem.* 79, 269-274 (2000).

111. Tsan, P. et al. Magnetic susceptibility tensor and heme contact shifts determinations in the Rhodobacter capsulatus ferricytochrome c': NMR and magnetic susceptibility studies. *J. Am. Chem. Soc.* 123, 2231-2242 (2001).

112. La Mar, G.N., Jackson, J.T., Dugad, L.B., Cusanovich, M.A. & Bartsch, R.G. Proton NMR study of the comparative electronic/magnetic properties and

Reproduced with permission of the copyright owner. Further reproduction prohibited without permission.

dynamics of the acid in equilibrium with alkaline transition in a series of ferricytochromes c'. *J. Biol. Chem.*, 265, 16173-16180 (1990).

113. Rakshit, G. & Spiro, T.G. Resonance Raman Spectra of Horseradish Peroxidase: Evidence for Anomalous Heme Structure. *Biochemistry* 13, 5317-5323 (1974).

114. Indiani, C., Feis, A., Howes, B.D., Marzocchi, M.P. & Smulevich, G. Effect of low temperature on soybean peroxidase: spectroscopic characterization of the quantum-mechanically admixed spin state. *J. Inorg. Biochem.* 79, 269-274 (2000).

115. Cole, S.T. *et al.* Deciphering the biology of Mycobacterium tuberculosis from the complete genome sequence. *Nature* **393**, 537-44 (1998).

116. Peisach, J., Blumberg, W.E., Ogawa, S., Rachmilewitz, E.A. & Oltzik, R. The Effect of Protein Conformation on the Heme Simmetry in High Spin Ferric Heme Proteins as Studied by Electron Paramagnetic Resonance. J. Biol. Chem. 246, 3342-3355 (1971).

Reproduced with permission of the copyright owner. Further reproduction prohibited without permission.